Supporting Information for

Synthetic Placement of Active Sites in MFI Zeolites for Selective Toluene Methylation to *para*-Xylene

Sopuruchukwu Ezenwa[1], Hansel Montalvo-Castro[2], Alexander J. Hoffman[2], Huston Locht[2], Jordan Attebery[2], Deng-Yang Jan[3], Michael Schmithorst[4], Bradley Chmelka[4], David Hibbitts[2]*, Rajamani Gounder[1]*

[1]*Davidson School of Chemical Engineering, Purdue University, West Lafayette, IN, 47907, USA*

[2]*Department of Chemical Engineering, University of Florida, Gainesville, FL, 32608, USA*

[3]*Honeywell UOP, Des Plaines, IL, 60017, USA*

[4]*Department of Chemical Engineering, University of California, Santa Barbara, Santa Barbara, CA, 93106, USA*

*Corresponding authors. E-mail: rgounder@purdue.edu, hibbitts@ufl.edu

Table of Contents

Materials and Methods

Section S1. Synthesis of MFI zeolites

The Al-substituted MFI (ZSM-5) zeolite samples used in this study were synthesized using different combinations of organic and inorganic structure directing agents (SDA) according to previously reported protocols (references provided below) or obtained from a commercial source (Zeolyst CBV8014, Lot #249347). Lab-synthesized samples are denoted as MFI-*X*-*Y*, where *X* indicates the major organic SDA used in the synthesis and *Y* denotes unique samples synthesized with the same organic SDA but with other synthesis parameters varied or maintained (i.e., replicates). The commercial sample is surmised to be synthesized using the conventional TPA organic SDA and is therefore denoted as MFI-TPA-C. Synthesis and characterization of ten of the 12 MFI samples in this study have been reported in three previous publications from our group[1–3], and two new samples were prepared herein (MFI-EDA-3 and MFI-EDA-4). Two of these (MFI-EDA-3 and MFI-EDA-4) are replicate syntheses performed to confirm reproducibility of samples reported in previous studies. In some cases, synthetic modifications such as introduction of boric acid (H_3BO_3) in synthesis gel were used to vary the crystallite size as previously reported[1,4]. All synthesis reagents were used without further purification. Detailed synthetic procedures are described below.

S1.1. MFI synthesis using TPA^+ and Na^+

Two of the MFI samples in this study (MFI-TPA-1, MFI-TPA-3) were respectively synthesized using tetrapropylammonium (TPA^+) without or with Na^+ using protocols reported by Nimlos et al.[2]. These samples were respectively named MFI-TPA(50,0) and MFI-TPA(55,5) in the original publication[2] and the sample nomenclature was MFI-OSDA(*X*,*Y*) where *X* is the Si/Al ratio of the zeolite solid and *Y* is the Na^+/OSDA ratio used in the synthesis gel. The MFI samples were obtained from synthesis gels with molar ratio of 1 SiO_2/0.01 Al_2O_3/0.10 or 0.611 TPAOH/0 or 0.26 Na_2O/ 44 H_2O/0.611 OH and hydrothermally crystallized in a 45 mL Teflon-lined stainless-steel autoclaves (Parr Instruments) in a forced convection oven at 433 K for 5 days. Detailed synthetic procedures can be found in the original publication[2].

S1.2. MFI synthesis using TPA^+ only in presence of boron heteroatoms

Two of the MFI samples in this study (MFI-TPA-2, MFI-TPA-4) were respectively synthesized using tetrapropylammonium (TPA^+) with high and low boron contents using protocols reported by Hur et al.[1]. These samples were respectively named B-Al-MFI-TPA(2.5,50) and B-Al-MFI-TPA(500,50) in the original publication and the sample nomenclature was B-Al-MFI-TPA(*a*,*b*) where *a* is the Si/B ratio and *b* is the Si/Al ratio used in the synthesis gel. The MFI samples were obtained from synthesis gels with molar ratio of 1 SiO_2/0.01 Al_2O_3/0.32 TPAOH/0.002 or 0.4 H_3BO_3/ 30.45 H_2O and hydrothermally crystallized in a 45 mL Teflon-lined stainless-steel autoclaves (Parr Instruments) in a forced convection oven at 443 K and rotated at 50 rpm for 7 days. Detailed synthetic procedures can be found in the original publication[1].

S1.3. MFI synthesis using EDA and TPA^+ in the presence and absence of B heteroatoms

Two of the MFI samples in this study (MFI-EDA-1, MFI-EDA-2) were respectively synthesized using tetrapropylammonium (TPA^+) and ethylenediamine (EDA) with high and no boron contents using protocols reported by Hur et al.[1] and adapted from methods first reported by Kester et al.[4]. These samples were named B-Al-MFI-EDA(2.5,50) and B-Al-MFI-EDA(B-free,50)

in the original publication[1] where the sample nomenclature was B-Al-MFI-EDA(*a*,*b*) where *a* is the Si/B ratio and *b* is the Si/Al ratio used in the synthesis gel. The MFI samples were obtained from synthesis gels with molar ratio of 1 SiO_2/0.01 Al_2O_3/0.02 TPAOH/0.29 EDA/0 or 0.4 H_3BO_3/ 10.2 H_2O and hydrothermally crystallized in a 45 mL Teflon-lined stainless-steel autoclaves (Parr Instruments) in a forced convection oven at 448 K and rotated at 50 rpm for 5 days. Detailed synthetic procedures can be found in the original publication[1].

Two previously unreported replicate MFI samples (MFI-EDA-3 and MFI-EDA-4) were synthesized in the presence and absence of B to confirm reproducibility of samples reported in previous study[1]. The synthesis gel molar ratio (1 SiO_2/0.01 Al_2O_3/0.02 TPAOH/0.29 EDA/0 or 0.4 H_3BO_3/ 10.2 or 15.6 H_2O) and synthetic protocols were similar to those of the previous studies[1,4] with the exception that the synthesis gel amount was scaled up (3×) from a 45 mL to a 120 mL Teflon-lined stainless-steel autoclave. In an example synthesis, 3.7 g of EDA (99.5 wt%, Sigma Aldrich) was added to a perfluoroalkoxy alkane (PFA) container (120 mL, Savillex Corp.). Then, 9.2 g of deionized H_2O (18.2 MΩ) was added to the EDA-containing jar. Then 5.2 g of boric acid (H_3BO_3, 99.5 wt%, Sigma-Aldrich) was added to the EDA mixture and the solution was stirred for 0.25 h under ambient conditions to homogenize contents. For MFI-EDA synthesis in absence of B, the H_3BO_3 addition was skipped. Next, 0.33 g of aluminum hydroxide ($Al(OH)_3$, 99 wt%, SPI Pharma), 2.2 g of tetra-n-propylammonium hydroxide (TPAOH, 40 wt%, Alfa Aesar) and 9.2 g of deionized water were mixed together in another PFA container and stirred for 0.25 h under ambient conditions to homogenize contents. The two solutions were then combined into one PFA container and 31.6 g of colloidal silica (Ludox AS40, 40 wt%, Sigma-Aldrich) was added to the mixture and stirred for 2 h under ambient conditions. The final synthesis gel mixture (~55–60 g) was hydrothermally crystallized in a 120 mL Teflon-lined stainless-steel autoclave in a forced convection oven at 448 K and rotated at 50 rpm for 5 days.

S1.4. MFI synthesis using DABCO and MA

Two MFI samples in this study (MFI-DABCO-1, MFI-DABCO-2) were synthesized using a mixture of 1,4-diazabicyclo[2.2.2]octane (DABCO) and methylamine (MA) using protocols reported by Nimlos et al.[2]. These samples were respectively named MFI-DABCO(44,0.04)-2 and MFI-DABCO(44,0.04)-1 in the original publication[2] where the sample nomenclature was MFI-OSDA(*X*,*Y*) where *X* is the Si/Al ratio of the solid and *Y* is the Na^+/OSDA ratio used in the synthesis gel. The MFI sample was obtained from synthesis gel with molar ratio of 1 SiO_2/0.0125 Al_2O_3/0.36 DABCO/0.36 MA/0.014 Na_2O/13.2 H_2O and crystallized in Teflon lined stainless-steel autoclaves (Parr Instruments) in a forced convection oven (Yamato DKN-402C) at 413 K for 16 days. Detailed synthetic procedures can be found in the original publication[2].

S1.5. MFI synthesis using C666 diquaternary ammonium surfactant

An MFI sample (MFI-TPA-C666) was synthesized using a gemini-type quaternary ammonium SDA with formula of C_6H_{13}–$N^+(CH_3)_2C_6H_{12}$–$N^+(CH_3)_2$–C_6H_{13} (designated as C666) using protocols reported by Bickel et al.[3], adapted from methods reported by Kim et al.[5]. The sample was named MFI-1.3-0.03 in the original publication[3] where the sample nomenclature was MFI-*X*-*Y* with *X* as the mol H^+ per unit cell and *Y* as the average length of the shortest crystallite dimension in μm. de The MFI-TPA-C666 sample was obtained from synthesis gel with molar ratio of 1 SiO_2/0.01 Al_2O_3/0.1 C666/0.09 Na_2O/40 H_2O and crystallized in Teflon lined stainless-steel autoclaves (Parr Instruments) in a forced convection oven at 413 K and rotated at 30 rpm for 16 days. Detailed synthetic procedures can be found in Bickel et al.[3].

Section S2. Characterization of MFI zeolites

In all cases, following zeolite crystallization, solids were washed with deionized water (18.2 MΩ) and acetone (Sigma-Aldrich, 99.9 wt%) in alternating steps (70 cm^3 per g solids per wash) for at least four times and until the pH of the supernatant remained constant between washes. Solids were then recovered via centrifugation (5000 rpm), dried in stagnant air for at 24 h, then heat treated in flowing dry air (1.67 $cm^3\ s^{-1}\ g_{cat}^{-1}$) while increasing the temperature to 853 K (0.0167 $K\ s^{-1}$) and holding for 10 h before cooling to ambient temperature. The dried (as synthesized) and heat-treated solids were further characterized using various techniques. Detailed characterization procedures for MFI samples used in this study can be found in Nimlos et al.[2] and Hur et al.[1]. These procedures are outlined in brief below. Summaries of characterization data are presented in Figures S29–S45 and Tables S6 to S10.

S2.1. X-ray diffraction (XRD)

Crystallographic structures were verified by acquiring powder X-ray diffraction (XRD) patterns on a Rigaku SmartLab X-ray diffractometer with a Cu Kα radiation source operated at 1.76 kW (40 kV, 44 mA) and comparing with reference patterns [6]. The diffraction patterns were measured from 4–40° at a step size of 0.01° and scan rate of 0.0167° s^{-1}. XRD patterns are shown in Figure S32

S2.2. N_2 adsorption isotherms

Micropore volumes were determined from N_2 adsorption isotherms at 77 K on either a Micromeritics ASAP 2020 surface area and porosity analyzer or a Micromeritics 3-Flex physisorption analyzer. Samples were degassed by heating to 393 K (0.167 $K\ s^{-1}$) under vacuum (5 μmHg) for 2h then heated to 623 K (0.167 $K\ s^{-1}$) under vacuum (<5 mmHg) for 9h prior to adsorption measurement. To obtain micropore volumes, adsorbed gas volumes ($cm^3\ g_{cat}^{-1}$ at STP) were converted to liquid volumes using a density conversion factor for liquid N_2 at 77 K. Micropore volumes estimated using volumetric uptakes of N_2 in the 0.05–0.35 P/P_0 region that were linearly extrapolated to zero pressure were consistent (±10%) with micropore volumes estimated from the minimum of the semilogarithmic derivative plot of the isotherm $\partial(V_{ads})/\partial(\ln(P/P_0))$ vs $\ln(P/P_0)$, where the first maximum represents the micropore filling transition and the subsequent minimum represents the end of micropore filling[7]. N_2 adsorption isotherms are shown in Figure S33 and micropore volumes are summarized in Table 1 in main text.

S2.3. Elemental analysis

Elemental analysis was performed either using inductively coupled plasma-optical emission spectroscopy (ICP-OES) (Si, Al, B, Na, Co) on a Thermo Scientific iCAP 7000 Plus Series ICP-OES or an atomic absorbance spectroscopy (AAS) (Al, Na only) on a PerkinElmer Model AAnalyst 300 spectrometer following sample dissolution in hydrofluoric acid (48 wt%) and further dilution with deionized water (18.2 MΩ). *[Caution: when working with HF acid, use appropriate personal protective equipment, ventilation, and other safety precautions.]* Calibrations with known standards were used to determine the elemental contents of each sample. Results from elemental analysis are summarized in Table 1 in main text and Table S6.

S2.4. Aqueous phase NH_4^+ ion-exchange and NH_3 temperature programmed desorption (TPD)

Following high temperature (853 K) treatment of as-synthesized MFI samples to combust occluded organic SDA, the resulting solids were converted into ammonium form (NH_4-form) by aqueous phase ion-exchange with ammonium nitrate at ambient conditions.[1,2] Ammonia temperature programmed desorption (NH_3-TPD) of NH_4-form samples was performed using a Micromeritics AutoChem II 2920 Chemisorption analyzer and either an Agilent 5793N mass-selective detection (MSD) system or an MKS Instruments Cirrus 3 quadrupole mass spectrometer to quantify NH_3 evolved when the NH_4-form sample was heated to 873 K in flowing He. Previously reported methods[1,4] to discriminate protons located at Al heteroatoms (H^+_{Al}) from those at B heteroatoms (H^+_B) were used to quantify H^+_{Al} in MFI-OSDA zeolites synthesized in presence of B heteroatoms. These validated methods involved holding the sample isothermally at 433 K under flowing He for 4 h to remove NH_3 bound to B heteroatoms before heating the sample to 873 K in flowing He to quantify NH_3 bound to Al heteroatoms. Quantified H^+_{Al} contents are normalized by Al content and presented as H^+/Al in Table 1 in main text.

S2.5. Scanning electron microscopy (SEM)

Scanning electron microscopy (SEM) on an FEI Quanta 3D FEG Dual-beam SEM instrument at accelerating voltages of 2–7 kV and a spot size range of 1–6 μm was used to obtain images and estimate average crystallite sizes. An FEI Teneo microscope operating at 2 kV was used to obtain SEM images for MFI-TPA-C666. Average crystallite sizes represent linear averages of the shortest crystallite dimension measured from SEM crystallite size distributions (>40 crystallites analyzed). Samples were coated in platinum prior to imaging to reduce charging effects. SEM images and crystallite size distribution are shown in Figures S34–S45 and average crystallite sizes and standard deviations are summarized in Table 1 in main text.

S2.6. Thermogravimetric Analysis (TGA) and Carbon Hydrogen Nitrogen (CHN) Analysis

Thermogravimetric analysis (TGA) was performed using a TA Instruments SDT Q600 thermogravimetric analyzer and differential scanning calorimeter (TGA-DSC) and involved heating as-synthesized MFI zeolites in flowing dry air to 523 K (0.167 K s^{-1}) for 0.5 h to remove physisorbed water before further heating to 1023 K (0.167 K s^{-1}). For single organic SDA system (i.e., TPA^+), the molar amount of occluded organic SDA (per MFI unit cell or per g solid) was determined from the molecular weight of the SDA (186.36 g mol^{-1} for TPA^+) and MFI unit cell (5769.09 g $(unit\ cell)^{-1}$) and dry weight loss (523–1073 K) assuming the SDA remains intact during hydrothermal crystallization. For mixed organic SDA systems, the molar ratios of occluded organic SDAs (EDA/TPA^+, MA/DABCO) were obtained from C and N elemental contents of as-synthesized MFI zeolites measured by CHN analysis (Perkin Elmer 2400 Series II CHNS/O Analyzer, Galbraith Laboratories) while assuming that all organic SDAs remain intact during hydrothermal crystallization according to Equations S1–S2:

$$\frac{EDA}{TPA} = \frac{12 - \frac{C}{N}}{2\left(\frac{C}{N} - 1\right)} \quad \text{(S1)}$$

$$\frac{MA}{DABCO} = \frac{2(\frac{C}{N} - 3)}{1 - \frac{C}{N}} \quad \text{(S2)}$$

Molar amounts of occluded organic SDAs (per MFI unit cell or per g zeolite) were obtained from a mass balance based on the total organic weight loss from TGA analysis and organic SDA molar ratios from CHN analysis. C/N ratio and OSDA per unit cell are reported in Table S9.

S2.7. Solid-State nuclear magnetic resonance (SS NMR) spectroscopy analyses

Solid-state one-dimensional (1D) direct-excitation ^{27}Al NMR spectra were acquired on fully hydrated zeolite samples using a Bruker Avance NMR spectrometer at a field of 18.8 T using 2.5 mm zirconia rotors and acquired under magic-angle-spinning (MAS) conditions of 30 kHz at room temperature. Prior to the ^{27}Al MAS NMR measurements, samples were stored in a sealed container containing a saturated solution of potassium chloride for at least 24 h (~85% relative humidity) to ensure consistent hydration. An 83.3 kHz 15° pulse was used to excite the central transition of the ^{27}Al nuclei. A 0.2 s recycle delay was used between pulses, which was found to be sufficient for the ^{27}Al nuclei to fully relax between scans. 16384 scans were acquired for each spectrum. The ^{27}Al MAS NMR spectra were referenced to an aqueous solution of 0.5 M $Al(NO_3)_3$ at 0 ppm. Solid-state 1D ^{27}Al MAS NMR spectra are shown in Figures S29 and S30.

Solid-state 2D *J*-mediated ^{27}Al–^{29}Si *J*-HMQC NMR spectra were acquired at 9.4 T and 100 K on a 400 MHz Bruker Ascend NMR spectrometer equipped with a triple-resonance NMR probehead using 3.2 mm zirconia rotors spinning at a MAS frequency of 8 kHz.[8] Samples were hydrated as described above prior to measurement. For each 2D spectrum, the indirect dimension was acquired with 32 increments of 2048 scans with a t_1 increment of 250 μs and a recycle delay of 1 s between scans. 25 kHz radiofrequency pulses were applied to ^{29}Si nuclei, and 16.7 kHz radiofrequency pulses were applied to ^{27}Al nuclei. A 1-ms double-frequency-sweep shaped pulse was applied to ^{27}Al nuclei before the initial 90° pulse of the *J*-HMQC sequence. This pulse was swept between 100 kHz and 1 MHz relative to the carrier frequency. ^{29}Si chemical shifts were indirectly referenced to tetramethylsilane at 0 ppm using tetrakis(trimethylsilyl)silane as a secondary standard at –9.84 ppm. ^{27}Al NMR chemical shifts were referenced to an aqueous solution of 0.5 M $Al(NO_3)_3$ at 0 ppm. All references were measured at room temperature. Solid-state 2D ^{27}Al–^{29}Si *J*-mediated MAS NMR spectra are shown in Figure S31.

Section S3. Toluene methylation kinetic studies

Reactor configuration and product analysis using gas chromatography (GC)

Toluene methylation experiments were performed in a tubular packed-bed reactor (quartz, 7 mm ID). In a typical kinetic study, zeolite samples (0.010–0.060 g; NH_4^+-form) were pelleted, crushed, and sieved to retain aggregates between 180 and 250 μm in diameter. The sieved samples were diluted with acid-purified quartz sand (SiO_2, 180–250 μm; Sigma-Aldrich) to maintain a constant mass (1.0 g) of packed bed supported between two plugs of quartz wool (0.030–0.050 g). The bed temperature was measured using a K-type thermocouple in contact with the outside of the quartz tube at the level of the bed and maintained at desired temperature using a three-zone furnace (Applied Test Systems) and Watlow temperature controllers (EZ-ZONE). Isothermal operation across the length of the catalyst bed (4–6 cm) was confirmed by moving the thermocouple across the length of the bed and confirming negligible temperature variation (<1 K) across the bed length. For higher conversion studies, a higher mass (1.8 g) of MFI sample was used without silica diluent.

Prior to measurements of rate data, the packed bed was pre-treated to 773 K (0.083 K s^{-1}) in 5 % O_2/He flow (UHP, Indiana Oxygen, 1.67 cm^3 s^{-1}) for 4 h, and then cooled (0.083 K s^{-1}) to reaction temperature (403 K) and flushed with He (UHP, Indiana Oxygen, 1.67 cm^3 s^{-1}) for 1 h before reactants were introduced. In some cases, used catalysts were regenerated to 803 K (0.033 K s^{-1}) in 5% O_2/He flow (UHP, Indiana Oxygen, 1.67 cm^3 s^{-1}). Liquid toluene (Sigma Aldrich, HPLC grade, >99.99%) was introduced via a syringe pump (KD Scientific Legato 100) and vaporized in a heated (473 K) low dead volume mixing tee (Valco Instruments) into a carrier stream of He (UHP, Indiana Oxygen) and dimethyl ether (DME, Matheson, CP, >99.5%). For toluene methylation studies with methanol, the liquid methanol (Sigma Aldrich, 99.99%) was premixed with liquid toluene in desired molar ratios (methanol/toluene = 0–4) and vaporized into a stream of He upstream of the reactor. Similarly, for toluene methylation studies with 2,6-di-*tert*-butylpyridine (DTBP, Sigma-Aldrich, >97%) or pyridine (Avantor, 99%), the liquid DTBP or pyridine were pre-mixed with toluene in desired molar ratios and vaporized in a stream of He upstream of the reactor. For all studies, total gas volumetric flow rates were between 0.83 and 1.67 cm^3 s^{-1}. Heated lines upstream of reactor were maintained >400 K, while heated lines from reactor outlet to GC were maintained >430 K to prevent condensation. Reactions were performed at desired toluene (0.2–9 kPa) and oxygenate partial pressures (5–66 kPa DME or 1–8 kPa methanol), while initial conversions were typically kept below 2%. Each reaction was performed at a fixed condition (e.g., 4 kPa toluene, 66 kPa DME, balance He) for the entire experiment (typically 6–18 h time-on-stream).

Methane (0–5 cm^3/min; 25% CH_4/Ar; Indiana Oxygen) was co-fed with the reactants and used as an internal standard to determine the molar flow rate of species in reactor effluent (F_i) as shown in Equations S3a-b, where A_i is the integrated GC peak area and α_i is the GC response factor for component *i*. Measured *Fi* were within 5% when calculated using a CH_4 internal standard (Eq. S3a) or when calculated using total molar flow rate of all species (F_{total}) in reactor inlet (Eq. S3b). Reactant and product concentrations were measured (25-30 min sampling intervals) by online gas chromatography (GC, Agilent 7890B) using DB-Wax column (30 m x 320 μm x 0.5 μm) and flame ionization detector. GC peak areas were quantified using response factors either measured (methane, DME, hexane, methanol, benzene, toluene, *p*-xylene, *m*-xylene, *o*-xylene) by feeding known concentrations of standards or extrapolated (trimethylbenzene, tetramethylbenzene) from linear correlations of known response factors of aromatic hydrocarbons

(benzene, toluene, *p*-xylene, *m*-xylene, *o*-xylene). All GC response factors agreed within 95% of response factors estimated using the effective carbon number approach[9]. For a given GC oven program, GC peaks were identified by comparing the retention times of known standards species (methane, DME, hexane, methanol, benzene, toluene, *p*-xylene, *m*-xylene, *o*-xylene, 1,2,4-trimethylbenzene, 1,3,5-trimethylbenzene, 1,2,4,5-tetramethylbenzene, pentamethylbenzene, hexamethylbenzene) or comparing peak elution order with published chromatograms from Agilent GC column guide to identify components without standards (e.g., 1,2,3-trimethylbenzene).

Prior to reaction, the feed stream composition was stabilized and verified from bypass injections to the GC. Under most of our study conditions at low conversions (<2%), xylenes were the major gas-phase hydrocarbon products (>97 mol%) in the reactor effluent while 1,2,4-trimethylbenzene were detected (<3 mol%) during some reactions. Product formation rates (r_j) are calculated from their reactor effluent molar flow rates (F_j) normalized by initial proton counts ($H^+_{initial}$; obtained using NH_3 TPD) as shown in Equations S4 and S5. Total xylene formation rates (r_{totalX}) were obtained from the sum of the formation rates of each xylene (F_{kX}) and further methylated products (mostly 1,2,4-trimethylbenzene). Xylenes selectivity (S_{kX}) is calculated (Eq. S6) from the individual xylene product formation rates normalized by total xylenes formation rates. Toluene conversions ($X_{Toluene}$) are calculated on a product mole basis (Eq. S7).

$$F_i = F_{CH_4} \frac{A_i}{A_{CH_4}} \frac{\alpha_{CH4}}{\alpha_i} \tag{S3a}$$

$$F_i = \frac{A_i}{\alpha_i} F_{total} \tag{S3b}$$

$$r_j = \frac{F_{product,\,j}}{H^+_{initial}} \tag{S4}$$

$$r_{totalX} = \sum_{k=1}^{3} F_{kX} + F_{1,2,4TMB} \tag{S5}$$

$$S_{kX} = \frac{r_{kX}}{\sum_{k=1}^{3} r_{kX}} \tag{S6}$$

$$X_{Toluene} = \frac{\sum_{k=1}^{3} F_{xyl,k} + F_{1,2,4TMB}}{F_{toluene,out} + \sum_{k=1}^{3} F_{xyl,k} + F_{1,2,4TMB}} \cdot 100 \tag{S7}$$

Section S4. Density functional theory (DFT) studies of MFI zeolites

Computational Methods

Periodic DFT calculations were performed using the Vienna ab initio simulation package (VASP)[10–13] in a fully periodic MFI unit cell and implemented in the Computational Catalysis Interface[14]. Plane-wave basis sets were constructed with the projector augmented wave potentials[15,16] with an energy cutoff of 400 eV except where noted. The exchange and correlation energies were estimated with the Perdew–Burke–Ernzerhof (PBE) form of the generalized gradient approximation (GGA).[17–19] The DFT-D3 method with Becke and Johnson (D3BJ) damping corrected for dispersive interactions.[20–22] Gas-phase calculations were performed in a 15 Å × 15 Å × 15 Å vacuum unit cell. Calculations involving charge species were performed with a uniform compensating background charge with dipole and quadrupole corrections. Structures with unpaired electrons were run spin-polarized.

The MFI-zeolite structure was obtained from the experimental results of van Koningsveld[23] to minimize restructuring artifacts that may influence energy estimates[24]. The T- and O-site indices referenced in this work follow the International Zeolite Association (IZA) convention[6]. The shape and lattice parameters for MFI (a = 20.090 Å, b = 19.738 Å, and c = 13.142 Å) were fixed across all calculations. Structures were optimized in a two-step procedure[14], which is more efficient than traditional single-step optimizations. In the first step, structures were electronically converged so that energies varied $<10^{-4}$ eV between iterations, and the maximum force on each atom was <0.05 eV $Å^{-1}$. In the second step, electronic structures were further optimized so that energies varied by $<10^{-6}$ eV between iterations to improve force estimates, and the maximum force on each atom was <0.05 eV $Å^{-1}$. Forces for the first and second steps were computed using a fast Fourier transform (FFT) grid with cutoffs of 1.5-times and 2.0-times of the plane-wave cutoff, respectively. The Brillouin zone was sampled at the Γ-point.[25] Transition state structures for toluene methylation toward *o*-X, *m*-X, and *p*-X were systematically studied across all 12 unique T-sites of MFI. Each T-site in MFI is tetrahedrally coordinated to four O-atoms; therefore, all the potential (48) T-O pairs were also considered. Three O sites (O4, O20, and O24) had environments too small to accommodate a toluene methylation transition state complex and were thus omitted from further investigation.

Calculations of DABCO-MA and DABCO-H_2O included one DABCO molecule in each of the four intersections of MFI and four co-SDA molecules (either MA or H_2O) nearby. One of these complexes was protonated and one Al was placed in the surrounding framework to balance the cationic charge. Several initial structures were created manually of the protonated DABCO-MA and DABCO-H_2O complexes for each of the 12 Al locations. After these initial optimizations, the Al was systematically moved to all 95 remaining positions in the unit cell for each of the provided structures. The lowest energy structure for each unique Al position from these optimizations were used in analysis, and were optimized again with the VASPsol implicit solvation model[26] with the relative permittivity of water at 298 K[27], ε = 80. Calculations performed with implicit solvation were performed in a single step with the same settings as the second step of optimizations described above but using a planewave energy cutoff of 600 eV.

Tools to systematically sample the zeolite pore structure in the Computational Catalysis Interface[14] were implemented to initiate transition states searches, by adding the toluene methylation transition state complex across all 42 accessible T-O pairs in MFI. O-atoms in MFI are often bridged between two potential and distinct T-sites; therefore, structural tools were also

developed to systematically vary Al-atom location for a given transition state complex. Furthermore, all states were also systematically reoriented based on their relevant interactions with the zeolite framework as explained in detail in our prior work[28], and then optimized in the aforementioned two-step procedure. These systematic orientations increase the likelihood of identifying the global minima and the lowest-energy saddle-point (transition states) connecting those minima. We demonstrated that these systematic reorientations could lower DFT-estimated energies by ~10–50 kJ mol^{-1}.[28] These differences are significant, as they may either include irrelevant pathways or exclude relevant ones; hence, systematic reorientations (enhanced DFT sampling) improve the accuracy of DFT calculations while being ~100-times more computationally efficient than AIMD simulations or alternative global minimization strategies while also being applicable to transition state searches. Overall, these structural tools allow for automated and efficient initiation of transition state searches, resulting in approximately 20,000 converged transition state structures for toluene methylation to form the three xylene isomers. Transition state complexes were then refined using the Dimer method[29], until the maximum force on all atoms was <0.05 eV A^{-1}. These dimer calculations were also performed using a two-step method analogous to that described for optimization.

Vibrational frequencies for reactant, product, and transition states were calculated using a fixed displacement method in which all adsorbate atoms, the framework Al atom, and the four O atoms attached to the Al atom were displaced. Vibrational frequencies are used to confirm transition state structures and to estimate the zero-point vibrational energy and temperature-corrected free energies (G) and enthalpies (H) for all states. Vibrational modes <60 cm^{-1} were replaced with 60 cm^{-1} (except for imaginary modes along the reaction coordinate in transition states), similar to previous work[28,30–32]. These low-frequency modes—typically associated with frustrated or hindered motions—are inaccurate and significantly contribute to vibrational entropy estimates.

Enthalpies (*H*) and Gibbs free energies (*G*) can be calculated from DFT-derived energies using statistical mechanics. Specifically, each is a sum of the electronic energy (E_0), the zero-point vibrational energy (ZPVE), and the respective vibrational, translational, and rotational motions of the species:

$$H = E_o + ZPVE + H_{vib} + H_{rot} + H_{trans} \tag{S8}$$

$$G = E_0 + ZPVE + G_{vib} + G_{rot} + G_{trans} \tag{S9}$$

at 403 K. Adsorbed species are not considered to have translational or rotational contributions; all such motions are modeled as frustrated vibrations on the zeolite pores. Vibrational, rotational, and translational enthalpies and free energies are estimated from other statistical mechanics formalisms:

$$ZPVE = \sum_i \left(\frac{1}{2} h\nu_i\right) \tag{S10}$$

$$H_{vib} = \sum_i \left(\frac{h\nu_i \exp\left(-\frac{h\nu_i}{kT}\right)}{1-\exp\left(-\frac{h\nu_i}{kT}\right)}\right) \tag{S11}$$

$$G_{vib} = \sum_i \left(-kT \ln\left(\frac{1}{1-\exp\left(-\frac{h\nu_i}{kT}\right)}\right)\right) \tag{S12}$$

$$H_{trans} = \frac{5}{2}kT \tag{S13}$$

$$H_{rot,linear} = kT \tag{S14}$$

$$H_{rot,nonlinear} = \frac{3}{2}kT \tag{S15}$$

$$G_{trans} = -kT \ln\left(\left(\frac{2\pi mkT}{h^2}\right)^{\frac{3}{2}} V\right) \tag{S16}$$

$$G_{rot} = -kT \ln\left(\frac{\pi^{\frac{1}{2}}}{\sigma}\left(\frac{T^3}{\theta_x\theta_y\theta_z}\right)^{\frac{1}{2}}\right) \tag{S17}$$

$$\theta_i = \frac{h^2}{8\pi^2 I_i k} \tag{S18}$$

where I_i is the moment of intertia about the i axis (either x, y, or z) and σ is the symmetry number of the species.

Section S5. Supplementary text and figures

S5.1. Reaction network during toluene conversion to xylenes

Toluene methylation to xylene products occurs on Brønsted acid catalysts as part of a complex reaction network that encompasses both parallel reactions of the toluene-methanol/DME reactants and sequential reactions of the primary xylene products (C_8). Under typical conditions studied in prior literature reports (573–773 K, toluene conversions > 5%), the concurrence of the primary toluene methylation with side reactions (xylene isomerization, further C_{8+} aromatic methylation, toluene disproportionation and transalkylation with C_{9+} methylbenzenes, polymethylbenzene dealkylation) results in a broad product distribution ranging from light (C_2-C_4) aliphatic hydrocarbons to heavy (C_{10+}) aromatic hydrocarbons[33,34]. A simplified reaction network is shown in Scheme S1. The reaction network often involves catalyst deactivation pathways associated with the formation of bulky polyalkylated aromatic species (e.g., hexamethylbenzene) or polycyclic aromatic hydrocarbons (e.g. pyrene) that either remain entrained within intracrystalline domains or are deposited on external crystallite surfaces[35]. Process parameters such as temperature, pressure, aromatic/oxygenate ratio, or space velocity have been reported to influence the prevalence of different side reactions. However, at the low reaction temperatures (<473 K) and low conversions (<2%) used in our study, the primary toluene methylation pathways typically dominate over other side reactions[33,36].

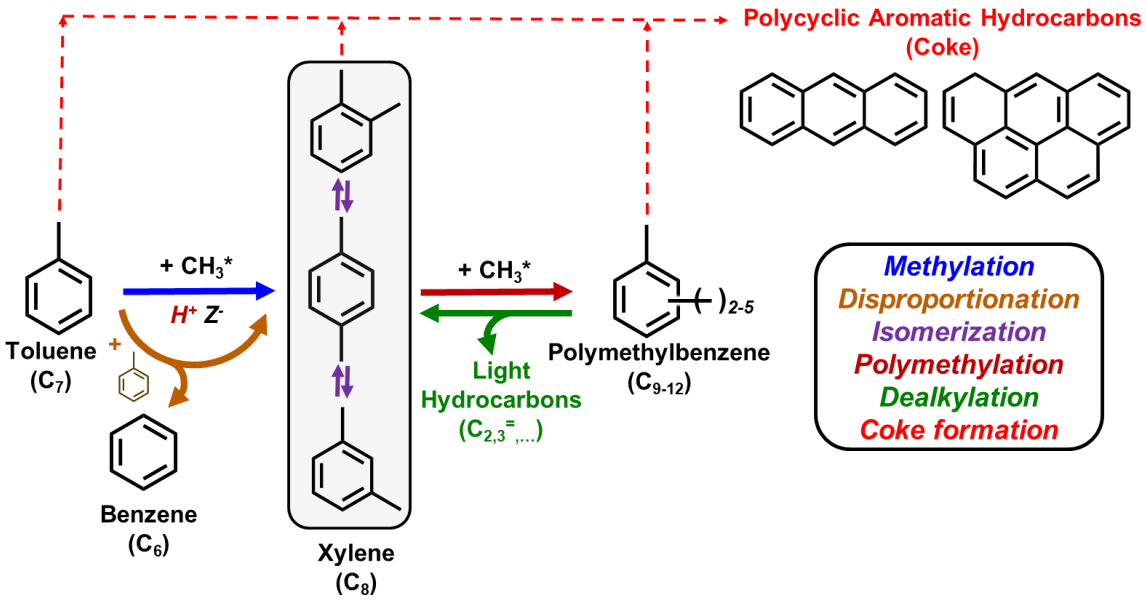

Scheme S1. Simplified toluene methylation reaction network showing various side reactions that can contribute to aromatics product selectivity.

S5.2. Carbon balance assessment, time-on-stream deactivation, and regeneration studies

A carbon balance was estimated using Equation S19 to confirm that the majority of products are detected in the gas phase and to assess the extent of carbon deposition on the catalyst during reaction. By comparing the total carbon molar flow rate (ΣF_n) in the reactor effluent during reaction to the total carbon molar flow rate when bypassing the reactor, the carbon balance closed within 90–110%; however, the low conversions (<1%) used in most of this study as well as minor syringe fluctuations (<10%) preclude a more rigorous estimation of the carbon balance. From the available data, we conclude that there is negligible carbon accumulation in the catalyst bed during kinetic studies and that observed gas-phase products are the majority of the reaction products.

$$Carbon\ balance = \frac{\Sigma_1^n n * F_{n,effluent}}{7 * F_{Toluene,bypass} + 2 * F_{DME,bypass} + 1 * F_{CH_4}} \quad \text{(S19)}$$

During toluene methylation at high DME-to-toluene ratios (>6:1), the high DME pressures (25–66 kPa) also promote further methylation of xylenes to C_{9+} polymethylbenzenes (<3% of gas phase aromatic products) that slowly accumulate within micropores and cause catalyst deactivation with time-on-stream (Scheme S1; Figs. S1–S6). The deactivation profile for the xylenes formation rate was fit with an empirical exponential decay model [37] (Eq. S20) to estimate initial rates:

$$r_X(t) = r_0 e^{-k_d t} + r_{ss} \quad \text{(S20)}$$

where r_{ss} is the pseudo-steady-state rate (value at which subsequent rates decreased by <5% every 0.5 h, usually occurs within first 6–8 h for MFI), $(r_o + r_{ss})$ is the initial rate, and k_d is the deactivation constant (h^{-1}). The non-linear regression was done by solving the non-linear least squares problem in OriginPro 2021 using the Levenberg-Marquardt (LM) algorithm or in JMP Pro 15 using the Gauss-Newton (GN) algorithm. The values of parameters estimated by both LM and GN algorithms in both software varied by less than 5%. The instantaneous xylene isomer selectivity is represented by Equation S21 which is similar to Equation S6:

$$S_{iX}(t) = \frac{r_{iX}(t)}{r_{pX}(t) + r_{mX}(t) + r_{oX}(t)} \quad \text{(S21)}$$

Two methods were used to estimate initial formation rates of all xylene isomer products ($r_{totalX,ini}$) and the initial selectivity to each xylene isomer ($S_{iX,ini}$). In the first method, $r_{totalX,ini}$ was obtained by fitting and extrapolating the measured total xylenes formation rate for the first 6–8 h to zero time-on-stream ($r_{totalX}(t = 0)$) using Equation S20 while the reported $S_{iX,ini}$ reflect measured instantaneous xylenes selectivity (Eq. S21) from the first data point (usually within the initial 0.2–0.5 h; i.e., $S_{iX}(t < 0.5\ h)$). Then, initial individual xylene formation rates ($r_{iX,ini}$) were obtained by Equation S22:

$$r_{iX,ini} = r_{totalX,ini} * S_{iX,ini} \quad \text{(S22)}$$

In the second method, the initial formation rates of each xylene isomer ($r_{iX,ini}$) were first obtained by fitting and extrapolating each individual xylene formation rate to zero time-on-stream ($r_{iX}(t = 0)$) using Equation S20. Then, the $r_{totalX,ini}$ was taken as the summation of all $r_{iX,ini}$ terms (Eq. S23), while the $S_{iX,ini}$ reflects the xylene selectivity obtained from $r_{iX,ini}$ (i.e., $S_{iX}(t = 0)$).

$$r_{totalX,ini} = r_{pX,ini} + r_{mX,ini} + r_{oX,ini} \quad \text{(S23)}$$

For both methods, the $r_{totalX,ini}$, $r_{iX,ini}$, and $S_{iX,ini}$ are similar (within ±5%) for experiments performed for MFI-TPA-C and MFI-EDA-1 at varying reactor bed residence times

as summarized in Table S1 and shown in Figures S1–S2. Thus, we have chosen to use method 1 for the data analysis for MFI samples in this manuscript.

Table S1. Comparison of two different methods for estimating initial rates and selectivity

Sample	Reactor bed residence time / mol H^+ s (mol C_7H_8)$^{-1}$	$r_{totalX,ini}$ Method #1 $r_{totalX}(t=0)$ / 10^{-3} mol xylenes (mol H^+ s)$^{-1}$	$r_{totalX,ini}$ Method #2 $\Sigma_i^3 r_{iX}(t=0)$ / 10^{-3} mol xylenes (mol H^+ s)$^{-1}$	$S_{iX,ini}$ Method #1 $S_{iX}(t<0.5\ h)$ *p*-X/*m*-X/*o*-X (TOS)	$S_{iX,ini}$ Method #2 $\frac{r_{iX}(t=0)}{\Sigma_i^3 r_{iX}(t=0)}$ *p*-X/*m*-X/*o*-X
MFI-TPA-C	1.5	0.586	0.592	0.28/0.08/0.64 (0.37 h)	0.29/0.07/0.64
MFI-TPA-C	4.4	0.723	0.737	0.24/0.05/0.71 (0.20 h)	0.24/0.06/0.70
MFI-EDA-1	1.8[a]	0.0814 (0.24 h)	-	0.82/0.03/0.15 (0.24 h)	-
MFI-EDA-1	7.7	0.0806	0.0827	0.84/0.03/0.13 (0.31 h)	0.86/0.02/0.12
MFI-EDA-1	14.5	0.0837	0.0848	0.83/0.02/0.15 (0.19 h)	0.83/0.02/0.15

[a]Data was collected for only 2 h at the 1.8 mol H^+·s (mol toluene)$^{-1}$ residence time and thus were not fit to Equation S20; initial rates reflect values at 0.24 h time on stream. Uncertainties on initial rate measurements are ±15%. Uncertainties on initial xylene selectivity are ±0.02.

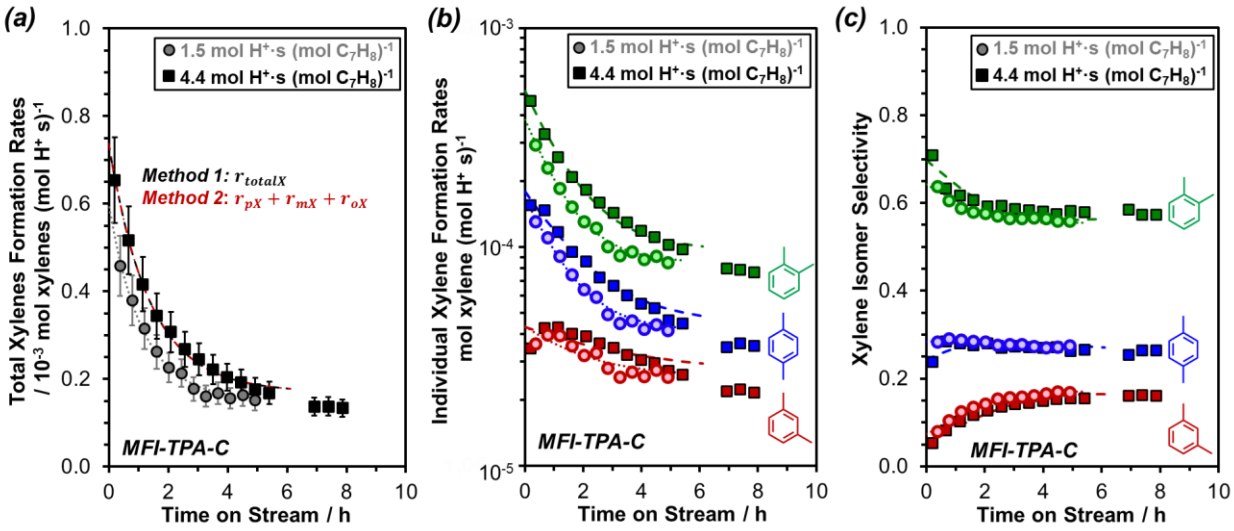

Fig. S1. (a) Measured and fitted (method 1 and 2) total xylenes formation rates, (b) measured and fitted (method 2) individual xylenes formation rates, and (c) measured and fitted (method 2) xylene isomer selectivity as a function of time on stream on MFI-TPA-C at 4.0–4.4 kPa toluene, 66 kPa DME, 403 K and varying reactor bed residence times (1.5 (···) or 4.4 (---) mol H^+·s (mol toluene)$^{-1}$). Dashed lines represent fits of measured data within the first 6 h time-on-stream to Equations S20-S21. Uncertainties on rate measurements are ±15%.

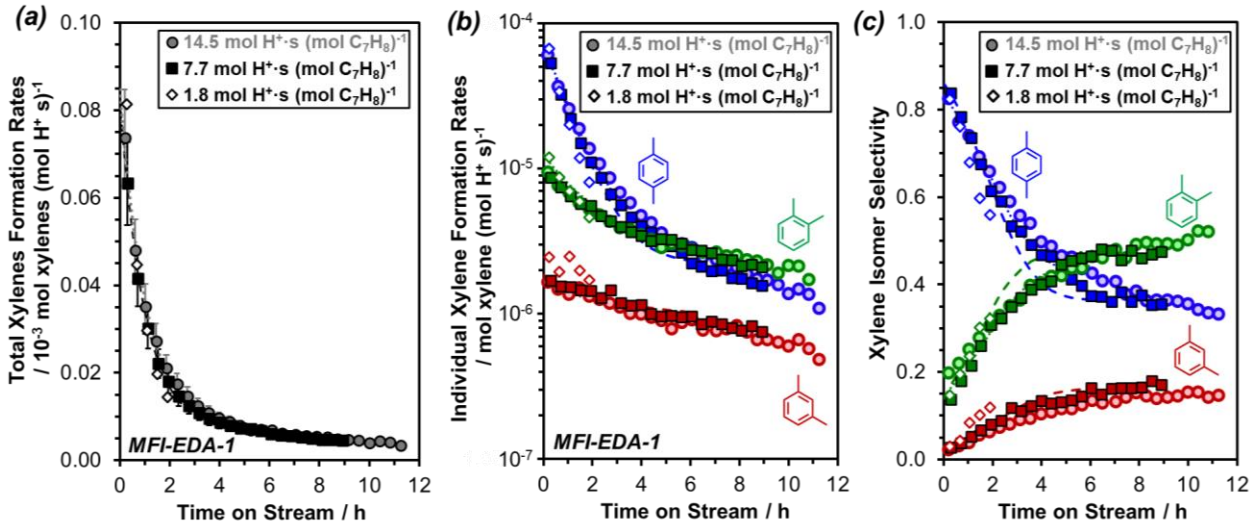

Fig. S2. (a) Measured and fitted (method 1 and 2) total xylenes formation rates, (b) measured and fitted (method 2) individual xylenes formation rates, and (c) measured and fitted (method 2) xylene isomer selectivity as a function of time on stream on MFI-EDA-1 at 4.0–4.4 kPa toluene, 66 kPa DME, 403 K and varying reactor bed residence times (1.8, 7.7 (···) and 14.5 (---) mol H^+·s (mol toluene)$^{-1}$). Dashed lines represent fits of measured data within the first 6 h time-on-stream to Equations S20–S21. Data was collected for only 2h at the 1.8 mol H^+·s (mol toluene)$^{-1}$ residence time and thus were not fit to Equation S20. Uncertainties on rate measurements are ±15%.

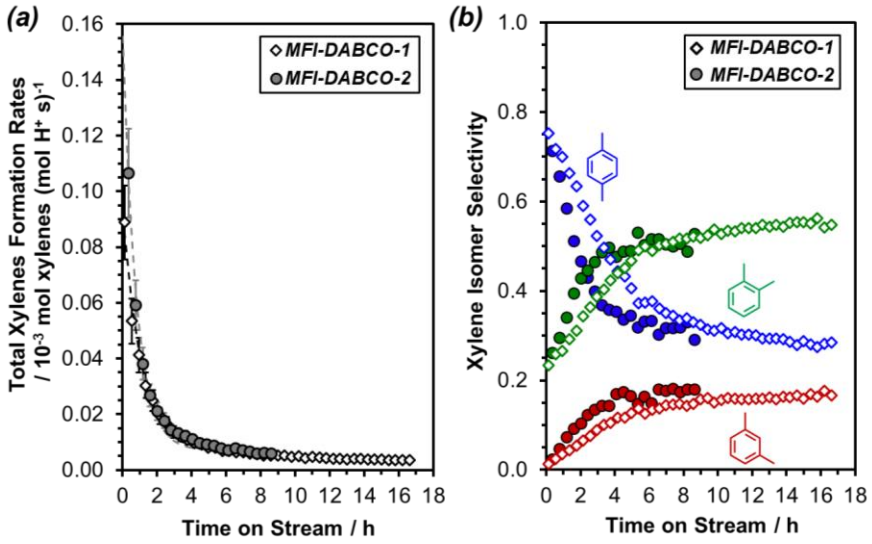

Fig. S3. (a) Measured and fitted (by method 2) total xylenes formation rates and (b) measured xylene isomer selectivity as a function of time onstream. Experiments were performed on MFI-DABCO-1,2 (3.7–4.0 kPa toluene, 66 kPa DME, 403 K, 5–30 mol H^+·s (mol toluene)$^{-1}$). Dashed lines represent fits of measured rate data within the first 6 h time-on-stream to Equation S20. Uncertainties on rate measurements are ±15%.

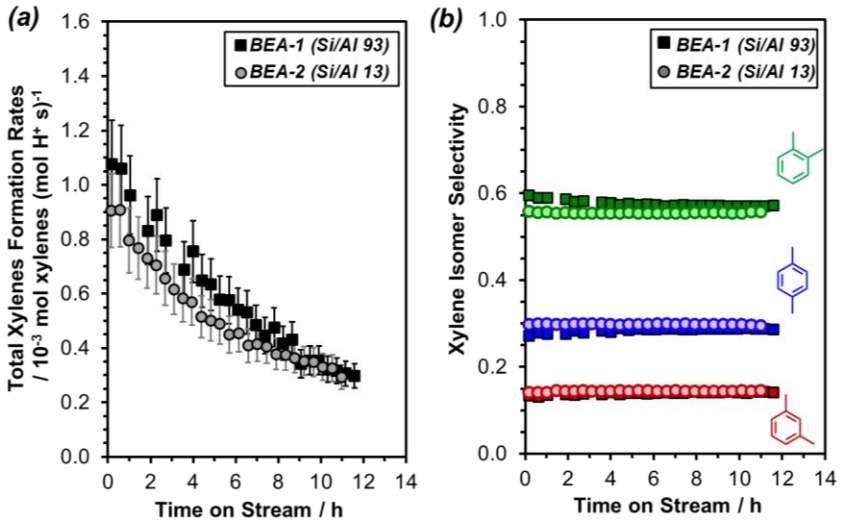

Fig. S4. (a) Total xylenes formation rates and (b) xylene isomer selectivity as a function of time on stream on the two BEA samples in this study (4.0–4.2 kPa toluene, 66 kPa DME, 403 K, 6.5–7.1 mol H^+·s (mol toluene)$^{-1}$). Uncertainties on rate measurements are ±15%.

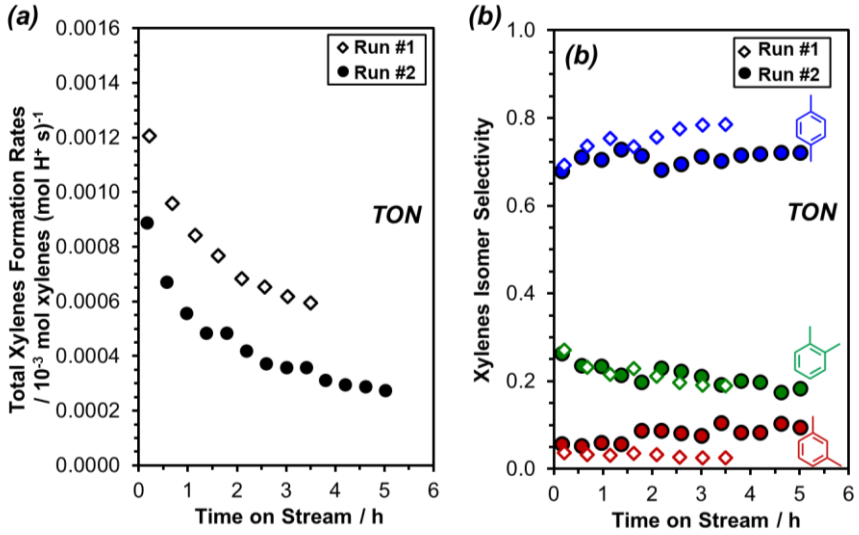

Fig. S5. (a) Total xylenes formation rates and (b) xylene isomer selectivity as a function of time-on-stream during toluene methylation on a TON zeolite sample (4.0–4.4 kPa toluene, 66 kPa DME, 403 K, 34.1–41.5 mol H^+·s (mol toluene)$^{-1}$). The TON zeolite sample was run with 2,6-di-*tert*-butylpyridine (DTBP) co-feeds (Run #1: 0.02 kPa DTBP; Run #2: 0.04 kPa DTBP) to remove contributions of external acid sites (further discussion in Section S5.9). For both cases, the xylene formation rates are normalized by the bulk proton content obtained using ammonium TPD.

Unlike the case of microporous aluminosilicates (MFI, BEA, TON), the xylene formation rates during toluene methylation on mesoporous MCM-41 initially increased to a maximum within the first 2 h time-on-stream and then only slightly decreased by ~10% over the following 12 h (Fig. S6). In addition, xylene isomer selectivity remained invariant with time-on-stream. Thus, reported rates on MCM-41 represent the maximum rate obtained after the initial induction period which reflect the initial slow replacement of protons with methyl groups from DME[38].

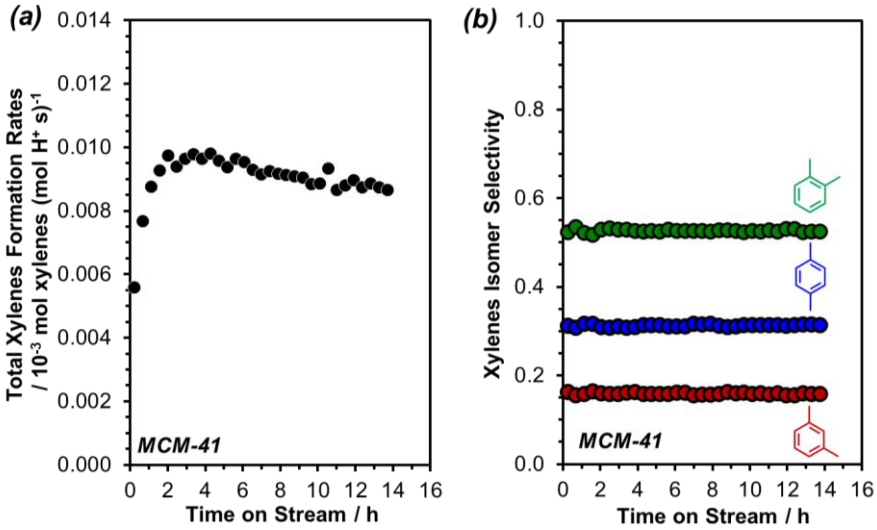

Fig. S6. (a) Xylenes formation rates and (b) isomer selectivity as a function of time on stream during toluene methylation on MCM-41 (4.0 kPa toluene, 66 kPa DME, 403 K, 32.5 mol H^+·s (mol toluene)$^{-1}$)

Fresh samples were used in almost all catalytic measurements, and where applicable, used samples were regenerated (5% O_2/He; 0.033 K s^{-1} to 803 K) a maximum of 2 times. Rates and selectivity negligibly changed (<10%) with catalyst regeneration (Fig. S7). The complete regeneration (>95%) of a representative MFI zeolite catalyst (MFI-EDA-3) in non-oxidative conditions (100% He; 0.033 K s^{-1} to 853 K) (Fig. S8) with the concurrent formation of less bulky aromatics (benzene, toluene, xylenes, 1,2,4-trimethylbenzene, 1,2,4,5-tetramethylbenzene) and light hydrocarbons (ethene, propene) during regeneration in 100% He evidences the formation of bulky polymethylated benzenes that gradually accumulate in the larger MFI intersections and are either unable to egress from the crystallite [39] or dealkylate at the lower temperatures (<433 K) of our study[33]. Thus, the rates and selectivity during toluene methylation with DME on MFI, BEA and TON (Figs. S1–S5) catalysts in this study were extrapolated to initial time-on-stream to reflect initial rates and selectivity in the absence of bulky intrapore species.

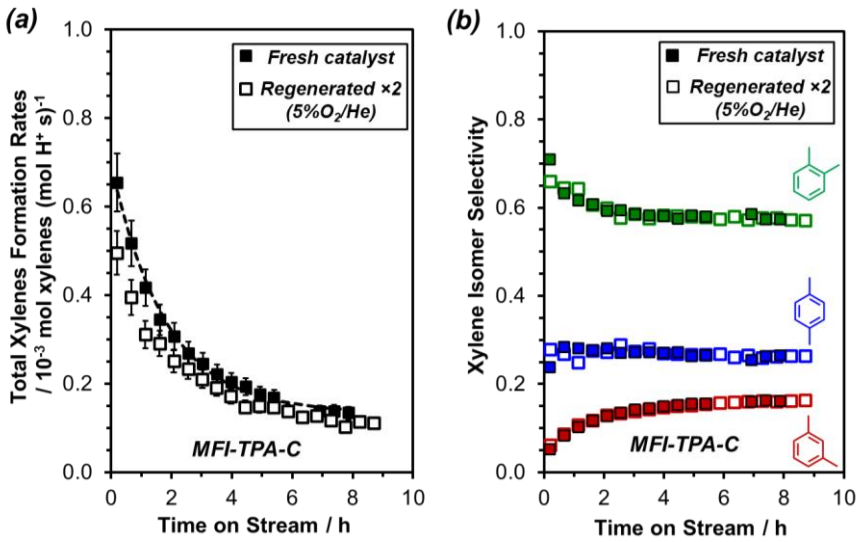

Fig. S7. (a) Xylenes formation rates and (b) xylenes isomer selectivity as a function of time on stream during toluene methylation (4.0-4.5 kPa toluene, 66 kPa DME, 403 K, 4.4 mol H^+·s (mol toluene)$^{-1}$)) on fresh and twice regenerated (5% O_2/He; 0.033 K s^{-1} to 803 K) MFI-TPA-C samples.

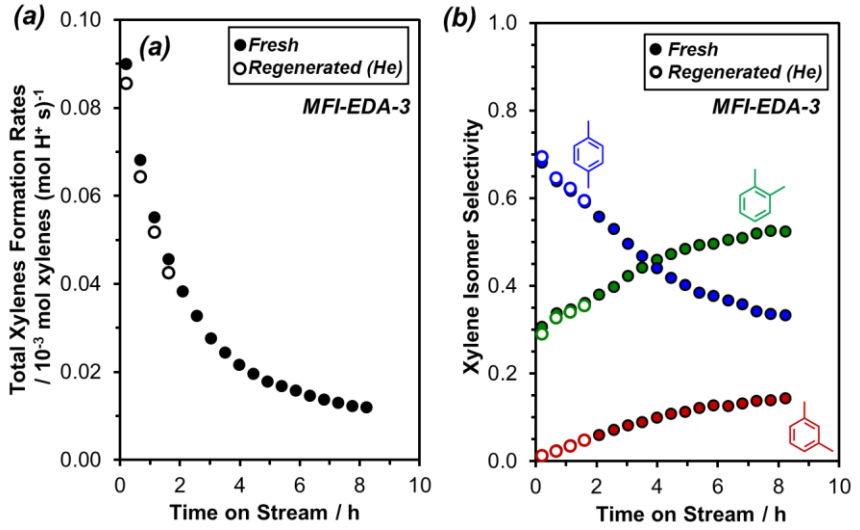

Fig. S8. (a) Xylenes formation rates and (b) xylenes isomer selectivity as a function of time on stream during toluene methylation (4.5 kPa toluene, 68 kPa DME, 403 K) on fresh and regenerated (100% He; 0.033 K s^{-1} to 853 K) MFI-EDA-3 samples. For easier comparison with the regenerated MFI-EDA-3 run, only the first 8 h time-on-stream data is shown for the fresh MFI-EDA-3 run. The full 22 h time on stream rate and selectivity data are not shown.

S5.3. Evaluation of extracrystalline transport and reactor bed residence time effects

To evaluate effects of extracrystalline transport effects, toluene methylation rates (per H^+, 403 K) were measured as a function of reactor bed residence time at fixed reactant partial pressures for three MFI samples (MFI-TPA-C, MFI-EDA-1, MFI-DABCO-1) representative for each group of MFI. Reactor bed residence times were varied by varying the catalyst mass at fixed reactant flow rates or varying the reactant flow rates at fixed catalyst mass. As shown in Figures S9a-c, the initial rates are independent of reactor residence times and the toluene conversions increased linearly with increasing reactor bed residence time, confirming reaction under differential conditions and absence of extracrystalline transport phenomena[40]. In addition, gas phase and background contributions to reactivity by quartz sand diluent, quartz wool and reactor internals were ruled out as no products were observed in blank reactor tests with quartz wool and SiO_2 sand at a temperature much higher (473 K) than that used in catalytic experiments (403–433 K).

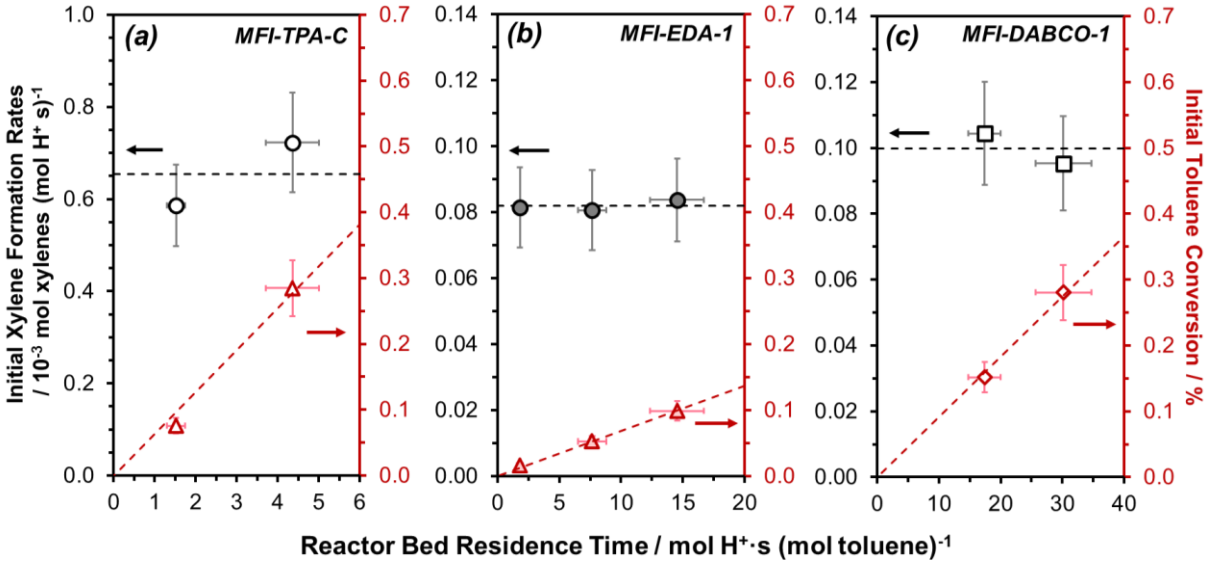

Fig. S9. Initial toluene methylation rates (black) and conversion (dark red) as a function of reactor bed residence time for (a) MFI-TPA-C (b) MFI-EDA-1 and (c) MFI-DABCO-1. Reaction conditions: 4.0-4.4 kPa Toluene, 66 kPa DME, 403 K. Dashed lines represent either the average rate of xylene formation or the line of best fit from the linear regression of the conversion data. Error bars on both vertical and horizontal axis are ±15%.

Xylene isomer selectivities were further evaluated at a wide range of reactor bed residence times and conversions spanning more than two orders of magnitude. As discussed in the main text (Section 2.1) and shown in Figures 3A-B, xylene isomer selectivity (403 K) negligibly depended on toluene conversions (<5%) within each MFI subset. At much higher conversions (up to 31%) and higher temperatures (403–473 K) on MFI-TPA-C, *o*-X remained the dominant aromatic product (~45 mol%) (Fig. S10). Thus, differences in xylene selectivity between MFI-TPA-X and MFI-EDA,DABCO cannot be explained by effects of reactor bed residence times and toluene conversions under the study conditions.

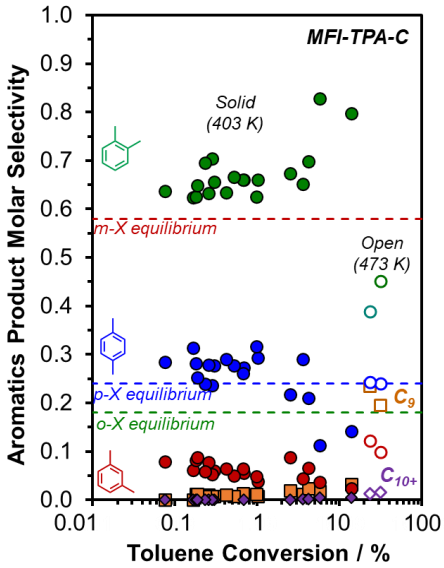

Fig. S10. Aromatics products molar selectivity as a function of toluene conversion (0.08–31.3%) during toluene methylation (403 K (solid) or 473 K (open), 0.2–8.8 kPa toluene, 4–66 kPa DME, 1.5–3900 mol H^+·s (mol toluene)$^{-1}$)) on MFI-TPA-C. Toluene conversions represent the conversions at initial times measured within the first 0.2–1.0 h.

S5.4. Assessment of intracrystalline transport effects

We assessed the influence of intracrystalline diffusional constraints on measured rates and selectivity using reaction-diffusion formalisms[41] that relate the measured rates and selectivity to reaction properties (e.g., intrinsic rate constants), molecular transport properties (e.g., effective diffusivities) and catalyst properties (e.g., active site density and crystallite size). Through the effectiveness factor (η), measured rates ($r_{Xyl,meas}$) are related to the intrinsic kinetic rates ($r_{Xyl,kin}$) when sites are exposed to the bulk fluid concentration of toluene present at the catalyst surface ($C_{Toluene,s}$):

$$r_{Xyl,meas} = \eta\,(\Phi_{Toluene})\, r_{Xyl,kin} \tag{S24}$$

$$r_{Xyl,kin} = k_{eff} C_{Toluene,s}^{n} \tag{S25}$$

Here, $k_{eff} C_{Toluene,s}^{n}$ is an assumed n[th] order toluene methylation rate expression. Increasing deviations for η below unity (for isothermal pellets and positive-order reactions) reflect more severe concentration gradients at the crystallite length-scales[42]. The effectiveness factor is a function of the Thiele modulus (Φ_j^2) which represents the reaction rate within micropores relative to the intracrystalline diffusion rates.

Furthermore, the Thiele modulus is parametrized by the effective diffusivity of toluene ($D_{e,Toluene}$; assumed to be concentration independent), the radius of the crystallite (R), the volumetric proton density ($[H^+]$), and the reaction rate constant (k_{eff}):

$$\Phi^2{}_{Toluene} = \frac{reaction\ rate}{diffusion\ rate} = \frac{k_{eff} C_{Toluene,s}^{n}\,[H^+]\,R^2}{C_{Toluene,s}\,D_{e,Toluene}} = k_{eff} C_{Toluene,s}^{n-1} \cdot \frac{[H^+]\,R^2}{D_{e,Toluene}} \tag{S26}$$

The combined parameter, $\frac{[H^+]\,R^2}{D_{e,Toluene}}$ represents the intracrystalline residence time of toluene which governs the number of sequential sorption and reactions that a diffusing species undergoes as it traverses a continuous crystalline domain during a single sojourn. For larger values of the Thiele modulus ($\Phi > 2$), the effectiveness factor for a quasi-spherical crystallite can be written as:

$$\eta(\Phi_{Toluene}) \approx \left(\frac{2}{n+1}\right)^{\frac{1}{2}} \frac{3}{\Phi_{Toluene}} = \left(\frac{2}{n+1} \cdot \frac{9\,D_{e,Toluene}}{k_{eff} C_{Toluene,s}^{n-1}}\right)^{\frac{1}{2}} \cdot \left(\frac{1}{[H^+]\,R^2}\right)^{\frac{1}{2}} \tag{S27}$$

Thus, the measured rates can be written in terms of the catalyst properties:

$$r_{Xyl,meas} = 3\left(\frac{2}{n+1} \cdot k_{eff}\, D_{e,Toluene}\right)^{\frac{1}{2}} \cdot C_{Toluene,s}^{\frac{n+1}{2}} \left(\frac{1}{[H^+]\,R^2}\right)^{\frac{1}{2}} \tag{S28}$$

For given zeolite topology (e.g., MFI), to a first approximation, $D_{e,Toluene}$ is independent of catalyst structural properties (e.g., site density and crystallite size); however, internal structural defects (e.g., twinning) or changes in morphology that emphasize higher densities of sinusoidal channels that are more tortuous than straight channels may cause $D_{e,Toluene}$ to vary among different samples[43,44]. Thus, in the limit of strong intracrystalline diffusion limitations, measured rates are expected to decrease with increasing $[H^+]R^2$. Yet, we observed that measured rates are independent of $[H^+]R^2$ within each MFI subset (Fig. S11 and S12a-b), thus indicating negligible influence of intracrystalline diffusional constraints on measured rates.

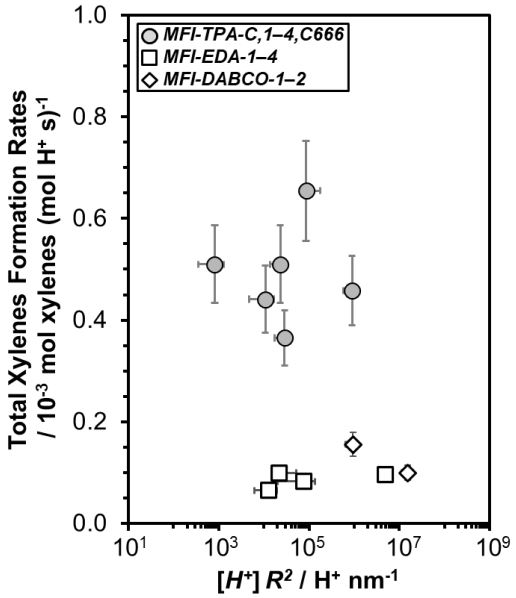

Fig. S11. Total xylenes formation rates as a function of $[H^+]R^2$. Reaction conditions: 3.7–4.7 kPa Toluene, 66–68 kPa DME, 403 K. Uncertainties in rate measurements are ±15%. Error bars on $[H^+]R^2$ reflect uncertainties propagated from the uncertainties in bulk proton density (±15%) and the standard deviations of the length of the shortest dimension of the crystallites estimated by SEM.

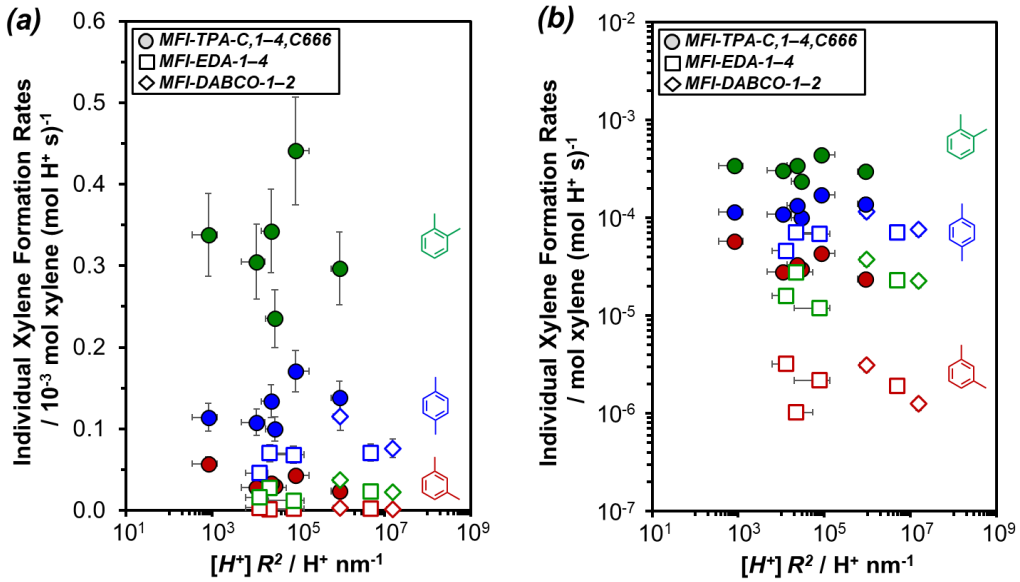

Fig. S12. Individual xylenes formation rates as a function of $[H^+]R^2$ in (a) linear-log scale and (b)log-log scale. Reaction conditions: 3.7–4.7 kPa Toluene, 66–68 kPa DME, 403 K. Uncertainties in rate measurements are ±15%. Error bars on $[H^+]\,R^2$ reflect uncertainties propagated from the uncertainties in bulk proton density (±15%) and the standard deviations of the length of the shortest dimension of the crystallites estimated by SEM.

On the other hand, negligible intracrystalline concentration gradients in toluene reactants do not necessarily preclude diffusional limitations of the bulkier reaction-derived products (e.g., xylenes)[45,46]. Among the three xylenes, *p*-X (kinetic diameter, d_{kin} = 0.585 nm and critical

diameter, d_{crit} = 0.67 nm) is smaller than *m*-X and *o*-X (both with d_{kin} = 0.68 nm and d_{crit} = 0.74 nm).[47–50] Significant differences in diffusivities of these xylene isomers within MFI, which could differ by up to three orders of magnitude ($D_{pX}/D_{mX,oX} \approx 10^2$–$10^3$)[39,51,52], may lead to isomer sieving behavior that is further enhanced by increased crystallite sizes or acid site densities. The contributions from diffusion-enhanced secondary reactions to measured selectivity depend on the intracrystalline residence times of each xylene ($\frac{[H^+]\,R^2}{D_{e,Xylene}}$) and their intrinsic net rates of formation and consumption ($r_{Xylene,kin,j}$) as captured in Equation S29 which relates the measured selectivities to the intrinsic selectivities and effectiveness factors ($\eta_j(\Phi_j)$).

$$S_{Xyl,meas,j} = \frac{r_{Xylene,\,meas,j}}{\sum_j r_{Xylene,\,meas,j}} = \frac{\eta_j(\Phi_j)\, r_{Xylene,kin,j}}{\sum_j \eta_j(\Phi_j)\, r_{Xylene,kin,j}} \qquad \text{(S29)}$$

If intracrystalline diffusion constraints are significant under these conditions, measured selectivity to the faster diffusing *p*-X isomer are expected to increase while those to *o*-X and *m*-X isomers decrease with increasing $[H^+]\,R^2$. However, we observed that measured selectivities are independent of $[H^+]\,R^2$ within each MFI subset (Fig. 3C, main text), thus indicating negligible influence of intracrystalline diffusional constraints on measured selectivity. Taken together, we conclude that differences in measured rate and selectivity among MFI subsets reflect intrinsic kinetic differences due to differences in transition state stabilities of individual xylenes.

Note: A sample calculation of $[H^+]R^2$ is outlined for MFI-TPA-C: The number of protons per unit cell (1.9 H^+ per unit cell) is obtained from the Al content per unit cell (2.2 Al per unit cell; Table 1, main text) and the H^+/Al ratio (0.85; Table 1). The volumetric proton density, $[H^+]$ (0.36 H^+ nm^{-3}) is calculated from the number of protons per unit cell and the volume of an MFI unit cell (5.211 nm^3 per unit cell; from IZA database[6]). Finally, $[H^+]R^2$ (9.0×10^4 H^+ nm^{-1}) is calculated from $[H^+]$ and the crystallite radius, R (500 nm) taken as the half-length of the shortest crystallite dimension (1000 nm; Table 1). The value of $[H^+]R^2$ can also be presented in molar units (1.5×10^{-19} mol H^+ nm^{-1}) using the Avogadro constant (6.022×10^{23} H^+ atoms per mol H^+).

S5.5. Benchmarking xylene selectivity with prior low temperature toluene methylation reports

The initial xylene selectivity on aluminosilicates at fixed conditions (403 K, 4 kPa toluene, 24-66 kPa DME) were compared to previously reported xylene selectivity during toluene methylation at low temperatures (288–523 K) and conversions (<6.0%) on MFI catalysts synthesized using TPA^+ [53], amorphous silica-alumina catalysts[54], and homogeneous Friedel-Crafts catalysts[55,56] (Table S2). Additional samples (MFI-TPA-C-1: CBV5524G, Si/Al = 31; MFI-TPA-C-2: CBV28014, Si/Al 134) and reaction conditions (403 K or 433 K, 4 kPa toluene, 4 kPa methanol) not included in the main text are also presented in Table S3. The *ortho*-selective xylene selectivity on all synthesized MFI-TPA-*Y* as well as commercial MFI samples (surmised to be synthesized using TPA^+) are similar to previously reported *ortho*-selective toluene methylation behavior[53–56] and consistent with established kinetically controlled electrophilic aromatic substitution patterns[57] that are not influenced by thermodynamically controlled xylene isomerization[58] or intracrystalline diffusion constraints [52].

In contrast, at higher reaction temperatures (>573 K) and higher conversions (>5%), product distributions during toluene methylations have been consistently observed[36,52,53] to result in either *meta*-selective distributions because of secondary xylene isomerization toward thermodynamic equilibrium amounts[58] or *para*-selective distributions because of constraints on intracrystalline xylenes diffusion that preferentially steer the isomerization of slower diffusing *o*-X and *m*-X toward faster diffusing *p*-X[52]. Thus, *para*-selective distributions observed at lower temperatures and conversions of this study reflect phenomena distinct from thermodynamic or diffusion control.

Table S2. Xylene selectivity from past literature reports during toluene methylation at low temperatures (<523 K) and low conversions (<6%).

Catalyst	Xylene Selectivity			Temperature; $X_{Toluene}$
	***p*-X**	***m*-X**	***o*-X**	
MFI (Young et al. 1982)	0.29	0.21	0.50	523 K; X = 1.8%
$SiO_2 \cdot Al_2O_3$ (Yashima et al. 1970)	0.25	0.19	0.56	498 K; X = 0.4%
$AlBr_3$ (Brown and Jungk 1955)	0.29	0.17	0.54	273 K
$AlCl_3$, $AlBr_3$ (Allen and Yats 1961)	0.26	0.14	0.60	288 K; X = 6.0%
$BF_3 \cdot P_2O_5$ (Allen and Yats 1961)	0.26	0.14	0.60	333 K; X = 2.0%
Thermodynamic Equilibrium (Chirico and Steele 1997)	0.24–0.25	0.56–0.61	0.15–0.19	300–500 K

Table S3. Summary of xylene selectivity in this study (4 kPa toluene, 403–433 K; $X_{Toluene}$<2%)

Catalyst	Initial Xylene Selectivity			Conditions (T, $X_{Toluene}$)
	***p*-X**	***m*-X**	***o*-X**	
MFI-TPA-C	0.28	0.08	0.64	403 K; X = 0.08%
MFI-TPA-C	0.26	0.07	0.67	403 K; X = 0.3%
MFI-TPA-C	0.22	0.07	0.71	403 K; X = 5.6%
MFI-TPA-C (4 kPa methanol)	0.29	0.17	0.54	403 K; X = 0.02%
MFI-TPA-C (4 kPa methanol)	0.27	0.19	0.54	433 K; X = 0.3%
MFI-TPA-C1 (4 kPa methanol)	0.34	0.14	0.51	403 K; X = 0.05
MFI-TPA-C1 (4 kPa methanol)	0.32	0.16	0.52	433 K; X = 0.5%
MFI-TPA-C2	0.29	0.04	0.67	433 K; X = 0.2%
MFI-TPA-1	0.27	0.08	0.64	403 K; X = 0.3%
MFI-TPA-2	0.26	0.07	0.67	403 K; X = 0.1%
MFI-TPA-3	0.30	0.05	0.65	403 K; X = 0.4%
MFI-TPA-4	0.24	0.06	0.69	403 K; X = 0.4%
MFI-TPA-C666	0.22	0.11	0.66	403 K; X = 0.5%
MFI-EDA-1	0.82	0.03	0.15	403 K; X = 0.02%
MFI-EDA-1	0.84	0.02	0.14	403 K; X = 0.05%
MFI-EDA-1	0.83	0.02	0.15	403 K; X = 0.1%
MFI-EDA-1 (4 kPa methanol)	0.84	0.06	0.10	403 K; X = 0.004%
MFI-EDA-1 (4 kPa methanol)	0.78	0.07	0.15	433 K; X = 0.05%
MFI-EDA-2	0.74	0.02	0.24	403 K; X = 0.07%
MFI-EDA-3	0.68	0.01	0.31	403 K; X = 0.5%
MFI-EDA-3 (0.02 kPa DTBP)	0.71	0.01	0.28	403 K; X = 0.5%
MFI-EDA-4	0.71	0.05	0.25	403 K; X = 1.4%
MFI-DABCO-1	0.75	0.02	0.24	403 K; X = 0.28%
MFI-DABCO-1 (0.02 kPa DTBP)	0.77	0.01	0.22	403 K; X = 0.15%
MFI-DABCO-2	0.74	0.02	0.24	403 K; X = 0.06%
BEA-1	0.28	0.13	0.59	403 K; X = 0.8%
BEA-2	0.30	0.14	0.56	403 K; X = 0.6%
TON	0.36	0.15	0.49	403 K; X = 0.004%
TON (0.02 kPa DTBP)	0.74	0.07	0.19	403 K; X = 0.003%
MCM-41 (mesostructured $SiO_2 \cdot Al_2O_3$)	0.30	0.15	0.55	403 K; X = 0.03%

S5.6. Rates and selectivity as a function of toluene and dimethyl ether pressures

The dependence of xylenes formation rates and isomer selectivity on reactant pressures were assessed on representative MFI samples in this study. On MFI samples (MFI-TPA-C, MFI-EDA-2), rates and selectivity were zero-order in DME pressure (25–66 kPa) at fixed toluene pressure (4 kPa) as shown in Figure S13., reflecting H^+ sites covered with DME-derived species.

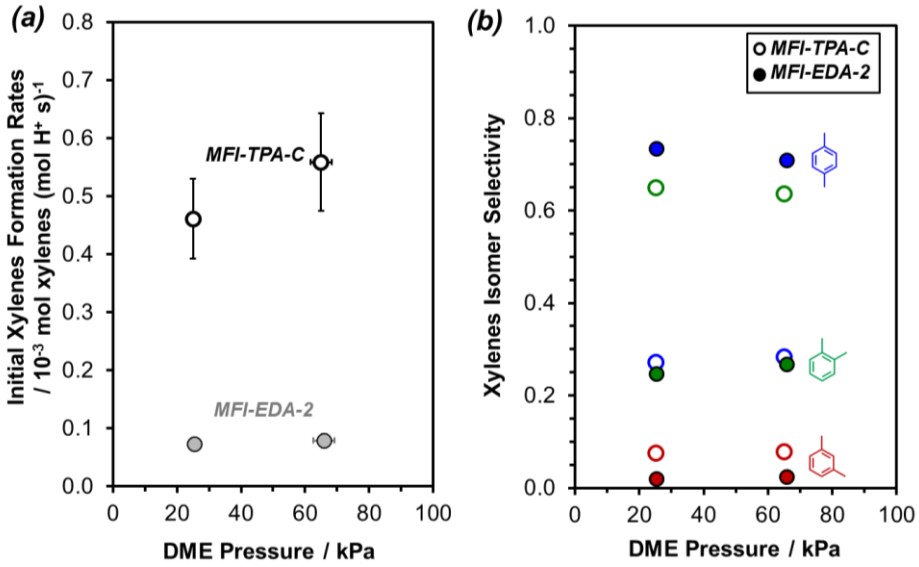

Fig. S13. (a) Xylenes formation rates and (b) Xylenes isomer selectivity as a function of DME pressure (25–66 kPa) during toluene methylation (403 K, 4.0–4.4 kPa) on MFI-TPA-C and MFI-EDA-2. Error bars on rates represent ±15% uncertainty in rate measurements.

As discussed in the main text and shown in Figure 2C and Figures S14a–15a,S17a–S19a, total xylenes formation rates on all aluminosilicates (MFI-TPA-C, MFI-EDA-1, MFI-DABCO-1, BEA-1, BEA-2, MCM-41, TON) transitioned from first- to zero-order dependence in toluene pressure (0.2–8.8 kPa), reflecting increasing coverages of co-adsorbed toluene on DME-derived intermediates that subsequently react *via* kinetically relevant C-C formation to xylenes (more discussion in Section S5.7). This trend was also observed with the individual xylenes formation rates as a function of toluene pressure on all aluminosilicates in this study as shown in Figures S14b–15b,S17b–S19b. Such trends are consistent with xylenes selectivity that are independent of toluene pressure (Figs. S14c–15c and S17c–S19c) and reflect parallel reaction steps to form each xylene isomer from the same pool of toluene-DME-derived intermediates. Based on these insights, the rest of the MFI samples were compared at fixed toluene pressures (~4 kPa) and DME pressures (~66 kPa) to assess how the various synthetic origins influence the observed xylene formation rates and isomer selectivity (Figs. S16a–b).

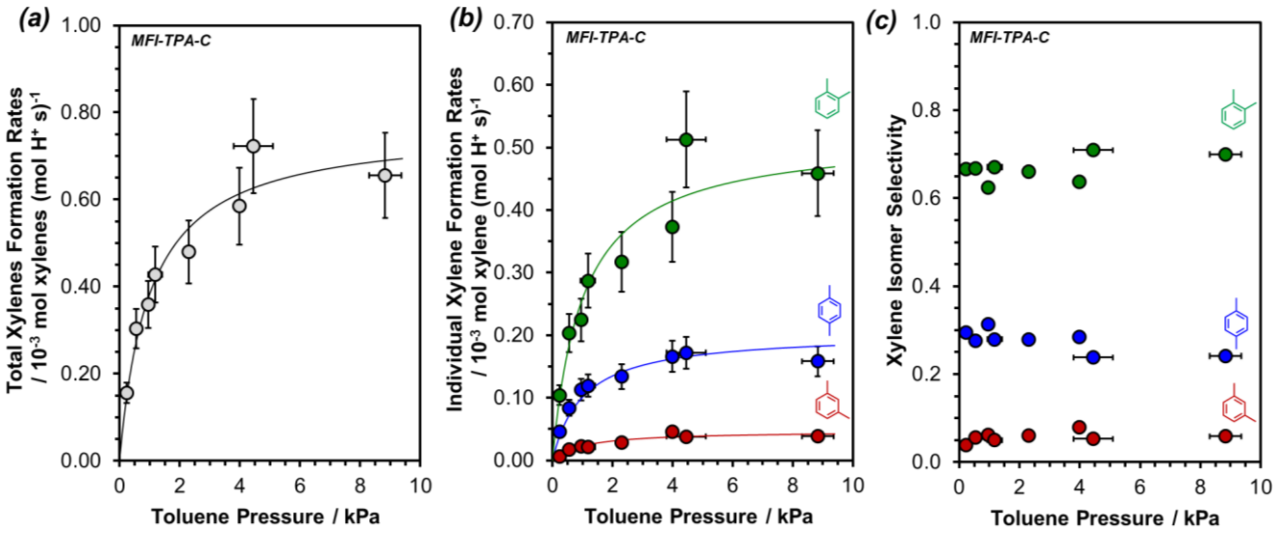

Fig. S14. (a) Total xylenes formation rates, (b) individual xylene formation rates, and (c) xylene isomer selectivity as a function of toluene pressures during toluene methylation (403 K, 0.2–8.6 kPa, 66-68 kPa DME) on MFI-TPA-C. Solid lines represent regressed best fits of measured data to Equation 2 in main text. Error bars on rates represent ±15% uncertainty in rate measurements while error bars on toluene pressures represent one standard deviation of average toluene pressures.

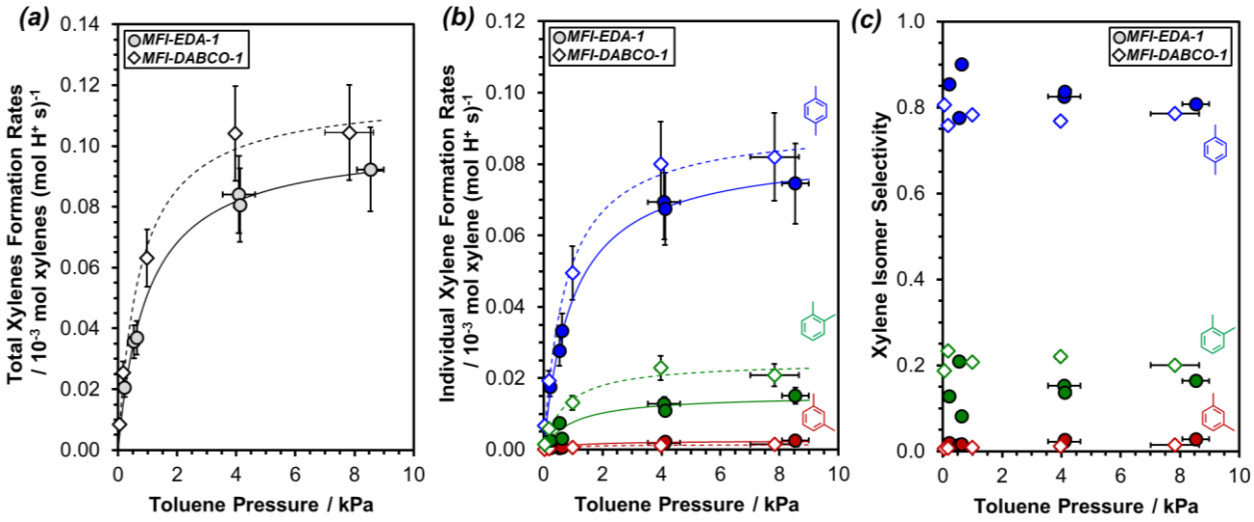

Fig. S15. (a) Total xylenes formation rates, (b) individual xylene formation rates, and (c) xylene isomer selectivity as a function of toluene pressures during toluene methylation (403 K, 0.05–8.6 kPa, 66-68 kPa DME) on MFI-EDA-1 (circles) and MFI-DABCO-1 (diamonds). Solid and dashed lines represent regressed best fits of measured data on MFI-EDA-1 and MFI-DABCO-1 respectively to Equation 2 in main text. Error bars on rates represent ±15% uncertainty in rate measurements while error bars on toluene pressures represent one standard deviation of average toluene pressures.

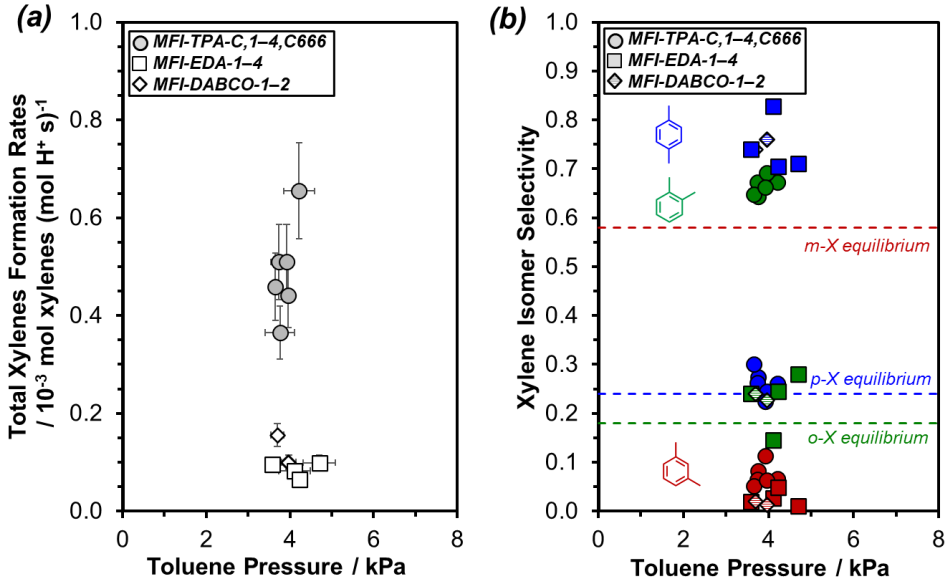

Fig. S16. (a) Xylenes formation rates and (b) xylene isomer selectivity at fixed toluene pressures (3.7–4.7 kPa) and DME pressures (66–68 kPa) during toluene methylation (403 K, 4.0–4.4 kPa) on all MFI samples in this study. Error bars on rates represent ±15% uncertainty in rate measurements while error bars on toluene pressures represent one standard deviation.

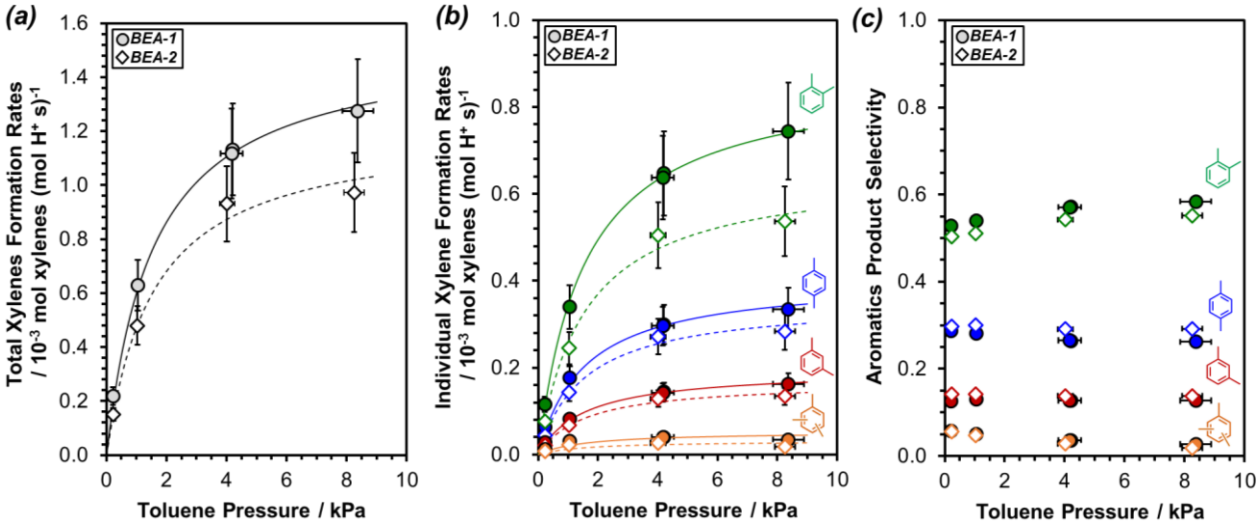

Fig. S17. (a) Total xylenes formation rates, (b) Individual xylene formation rates, and (c) aromatic product selectivity as a function of toluene pressure during toluene methylation (403 K, 0.2-8.4 kPa, 66-68 kPa DME) on BEA-1 (circles) and BEA-2 (diamonds). Solid and dashed lines represent regressed best fits of measured data on BEA-1 and BEA-2 respectively to Equation 2 in main text. Error bars on formation rates represent ±15% uncertainty in rate measurements while error bars on toluene pressures represent one standard deviation of average toluene pressures. Unlike during toluene methylation on MFI where the gas phase trimethylbenzene selectivities are usually negligible (<0.02) at low toluene conversions (<2%), the gas phase trimethylbenzene selectivities (0.02–0.06) are non-negligible during toluene methylation on BEA under the same low toluene conversions (<2%). Tetra-,penta- and hexa-methylbenzenes were also observed in trace amounts

(<0.005 of gas phase aromatic selectivity). Thus, trimethylbenzenes are the only polymethylated species included in the total xylene formation rates and selectivity.

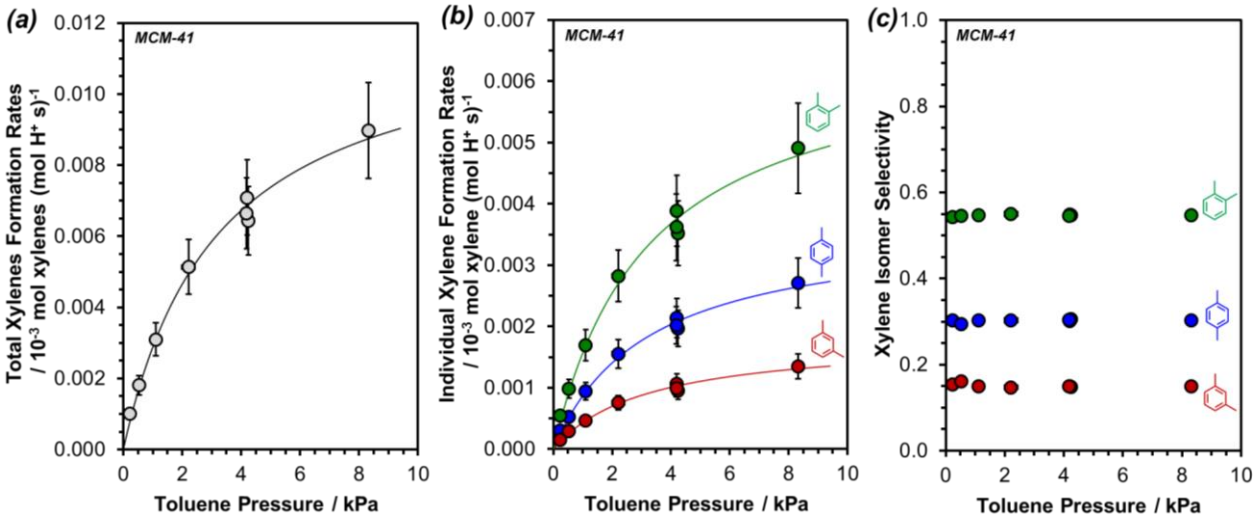

Fig. S18. (a) Total xylenes formation rates, (b) individual xylene formation rates, and (c) xylene isomer selectivity as a function of toluene pressures during toluene methylation (403 K, 0.2–8.3 kPa, 66-68 kPa DME) on MCM-41. Solid lines represent regressed best fits of measured data to Equation 2 in main text. Error bars on rates represent ±15% uncertainty in rate measurements while error bars on toluene pressures represent one standard deviation of average toluene pressures.

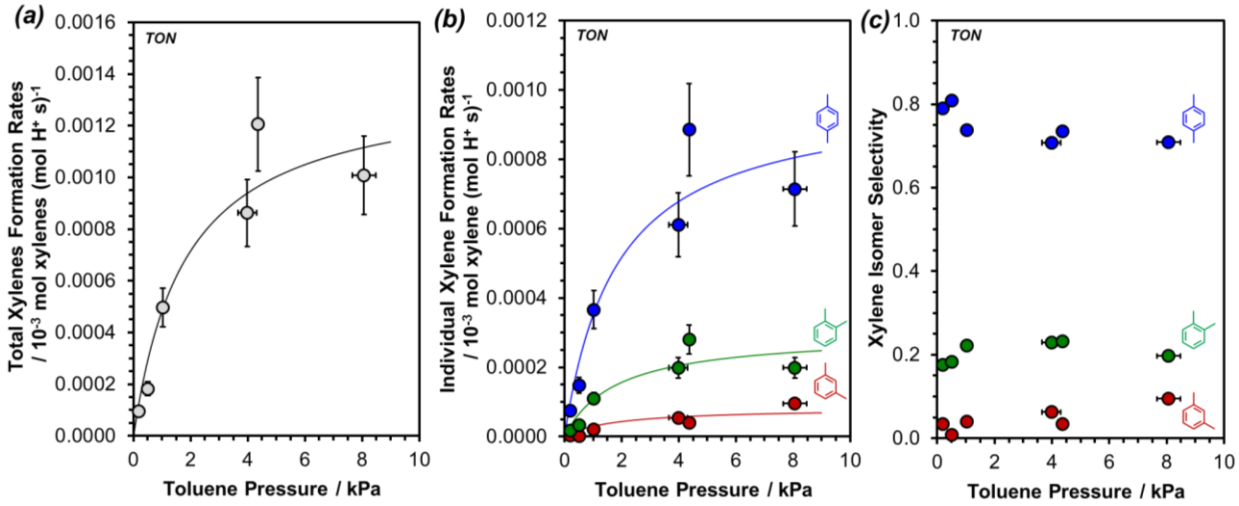

Fig. S19. (a) Total xylenes formation rates, (b) individual xylene formation rates, and (c) xylene isomer selectivity as a function of toluene pressures during toluene methylation (403 K, 0.2–8.1 kPa, 66-68 kPa DME) on TON. Solid lines represent regressed best fits of measured data to Equation 2 in main text. Error bars on rates represent ±15% uncertainty in rate measurements while error bars on toluene pressures represent one standard deviation of average toluene pressures.

S5.7. Derivation of toluene methylation rate expression

The rate expression for toluene methylation with DME to form xylenes is derived using assumptions about the irreversible or quasi-equilibrated (QE) nature of proposed elementary steps for the sequential (or dissociative) pathway and using insights from previous studies[28,38,59]. The sequence of elementary steps begins with the QE adsorption of DME from gas phase ($(CH_3)_2O_{(g)}$) onto a Brønsted acid site (H–Z) and subsequent QE methylation of the zeolite to form a surface methoxy (CH_3–Z) while liberating methanol into the gas phase ($CH_3OH_{(g)}$). This latter step is followed by the QE co-adsorption of toluene from gas phase ($C_7H_{8(g)}$) onto CH_3–Z and then the irreversible and kinetically relevant C–C bond formation between co-adsorbed toluene-surface methoxy intermediate (C_7H_8--CH_3–Z) to form xylenes that desorbs into the gas phase ($C_8H_{10(g)}$). For brevity, steps involving the physisorption of reactants and products from external bulk gas phase ($A_{(g)}$) into the zeolite micropores ($A_{(p)}$) are omitted because equilibrium is established between extracrystalline gas-phase and intracrystalline pore phase and these steps are typically kinetically irrelevant[59]. In addition, under the high DME:toluene ratios ($P_{DME}/P_{Toluene}>8$) of this study, the adsorption of toluene onto Brønsted acid sites is assumed to be negligible as sites are covered with DME-derived species (Fig. S13). Similarly, the surface coverages of products (xylene and methanol) on Brønsted acid sites are assumed to be negligible because of the low reactant conversion ($X_{toluene}<1\%$, $X_{DME}<0.1\%$) that lead to very low product pressures ($P_{Methanol}<0.05$ kPa, $P_{Xylene}<0.05$ kPa) relative to reactant pressures (P_{DME} = 66 kPa, $P_{Toluene}$ = 0.2-8.8 kPa). Thus, elementary steps corresponding to the desorption/adsorption of C_7H_8, CH_3OH, and C_8H_{10} onto Brønsted acid sites are omitted as they negligibly contribute to the surface coverages.

This sequence of elementary steps for toluene methylation with DME is given below:

$$(CH_3)_2O_{(g)} + H\text{–}Z \overset{K_A}{\rightleftharpoons} (CH_3)_2O\cdot H\text{–}Z \quad \text{(S30)}$$

$$(CH_3)_2O\cdot H\text{–}Z \overset{K_M}{\rightleftharpoons} CH_3\text{–}Z + CH_3OH_{(g)} \quad \text{(S31)}$$

$$C_7H_{8(g)} + CH_3\text{–}Z \overset{K_C}{\rightleftharpoons} C_7H_8\cdot CH_3\text{–}Z \quad \text{(S32)}$$

$$C_7H_8\cdot CH_3\text{–}Z \overset{k_{iX}}{\longrightarrow} C_8H_{10(g)} + H\text{–}Z \quad \text{(S33)}$$

Here K_A, K_M, and K_C are respectively the equilibrium constants for DME adsorption, surface methylation, and toluene co-adsorption, while k_{iX} represents the forward rate constant for C-C bond formation to xylenes. The deprotonation of the resulting xylenium intermediate after C-C bond-formation was omitted because of the kinetic irrelevance of such steps during toluene methylation in both heterogenous and homogeneous acid catalysis[28,57]. The elementary steps are also represented in a catalytic cycle in Scheme 2 in main text.

The xylene formation rate (r_{iX}) can be expressed as the net rate of a non-equilibrated step (Eq. S34), taken here as the irreversible C-C bond formation between co-adsorbed toluene-surface methoxy intermediate:

$$r_{iX} = k_{iX}[C_7H_8\cdot CH_3\text{–}Z] \quad \text{(S34)}$$

where $[A]$ is the concentration of a surface intermediate A. Based on the assumed QE of adsorption, surface methylation and co-adsorption steps, the concentrations of the surface intermediates can

be written in terms of concentration of empty sites ($[H-Z]$) and partial pressures of gas-phase reactant and product species ($P_{DME}, P_{Methanol}, P_{Toluene}$) :

$$[(CH_3)_2O \cdot H{-}Z] = K_A P_{DME}[H-Z] \tag{S35}$$

$$[CH_3{-}Z] = K_M K_A \frac{P_{DME}}{P_{Methanol}}[H-Z] \tag{S36}$$

$$[C_7H_8 \cdot CH_3{-}Z] = K_C K_M K_A \frac{P_{DME}}{P_{Methanol}} P_{Toluene}[H-Z] \tag{S37}$$

Substituting Equation S37 into Equation S34 yields the xylenes formation rate expression:

$$r_{iX} = k_{iX} K_C K_M K_A \frac{P_{DME}}{P_{Methanol}} P_{Toluene}[H-Z] \tag{S38}$$

The concentration of empty sites ($[H-Z]$) can be determined using a site balance where the total number of active sites ($[L]$) accessible to reactants regardless of their state (unoccupied or occupied by guest species) are conserved:

$$[L] = [H-Z] + [(CH_3)_2O \cdot H{-}Z] + [CH_3{-}Z] + [C_7H_8 \cdot CH_3{-}Z] \tag{S39}$$

Using Equations S35–S37, Equation S39 can be recast to express the concentration of unoccupied sites ($[H-Z]$):

$$[H-Z] = \frac{1}{1 + K_A P_{DME} + K_M K_A \frac{P_{DME}}{P_{Methanol}} + K_C K_M K_A \frac{P_{DME}}{P_{Methanol}} P_{Toluene}}[L] \tag{S40}$$

Substituting Equation S40 into Equation S39 gives a rate expression in terms of only measurable quantities, equilibrium constants and rate constants:

$$\frac{r_{iX}}{[L]} = \frac{k_{iX} K_C K_M K_A \frac{P_{DME}}{P_{Methanol}} P_{Toluene}}{1 + K_A P_{DME} + K_M K_A \frac{P_{DME}}{P_{Methanol}} + K_C K_M K_A \frac{P_{DME}}{P_{Methanol}} P_{Toluene}} \tag{S41}$$

where the denominator terms, in order, respectively represent ratios (relative to H-Z) of concentrations of unoccupied Brønsted acid sites (H–Z), adsorbed DME ($(CH_3)_2O{\cdot}H–Z$) surface methoxides ($[CH_3{-}Z]$) and co-adsorbed toluene-surface methoxides (C_7H_8--CH_3–Z). Based on previous IR spectroscopic studies (438 K) during short pulses of DME, the O–H stretching band disappeared because of occupation of acid sites by DME-derived intermediates (CH_3–Z, $(CH_3)_2O{\cdot}H$–Z).[38] DFT studies also predict that under the study conditions (403 K, 68 kPa DME, 3 kPa toluene, 0.1% C_7H_8 conversion), the fraction of unoccupied sites is negligible ($<10^{-6}$) because surfaces are covered with DME-derived species under the study conditions.[28]

However, there is a lack of consensus among previous experimental and DFT analysis on the predominant DME-derived species (e.g., adsorbed DME, surface methoxides) during methylation reactions with DME at low temperatures (<500 K). Rapid isotopic scrambling ($^{12}CH_3/^{13}CH_3$ or CH_3/CD_3) to binomial isotopologue distributions in equimolar mixtures of $^{12}CH_3O^{12}CH_3$–$^{13}CH_3O^{13}CH_3$ during steady-state CO methylation (438 K, 4 kPa DME, 97 kPa ^{12}CO) in MOR zeolites [38] or CH_3OCH_3–CD_3OCD_3 during steady-state toluene methylation (343 K, 20 kPa DME, 1 kPa C_7H_8) in MFI zeolites [59] were used to evidence the quasi-equilibration of

the DME adsorption (438 K) and surface methylation steps and the prevalence of surface methoxides at low temperatures (<500 K). Further stoichiometric evidence from DME titration of H–Z on fresh MOR and MFI ($DME_{adsorbed}$/Al = 0.5±0.05; 438 K) [60] or during post-reaction H_2O titration of surface methoxides on MFI ($CH_3OH_{evolved}$/Al = 0.95–0.98; 423 K) [59] also supported the experimental conclusions that surface methoxy species are the predominant DME-derived intermediates under their study conditions. In contrast, from maximum rate analyses using DFT-obtained adsorption energies, CH_3–Z was predicted to be the most abundant surface intermediates (MASI) only at temperatures above 503 K, while $(CH_3)_2O{\cdot}H$–Z is the MASI between 383 and 493 K [28]. Furthermore, toluene co-adsorbed on DME-derived species can contribute to the MASI (e.g., C_7H_8--CH_3–Z).

At the high DME:methanol pressures measured in the reactor effluent (P_{DME}:$P_{Methanol}$ ratios $>10^3$), we assume that surface methoxides and toluene co-adsorbed on surface methoxides are the MASI under our study conditions (403 K, >25 kPa DME). This assumption further stems from insights from previous studies (discussed above) during toluene methylation with DME (29-68 kPa DME, 353-403 K) [59] and CO methylation with DME (1-67 kPa DME, 423-463 K) [38,60] that provided kinetic, isotopic and spectroscopic evidence that surface methoxides are the DME-derived intermediates during methylation reactions under their study conditions which is similar to ours. With these assumptions the full mechanism-derived rate expression (Eq. S41) becomes:

$$\frac{r_{iX}}{[L]} = \frac{k_{iX}K_C K_M K_A \frac{P_{DME}}{P_{Methanol}} P_{Toluene}}{K_M K_A \frac{P_{DME}}{P_{Methanol}} + K_C K_M K_A \frac{P_{DME}}{P_{Methanol}} P_{Toluene}} \quad \text{(S42)}$$

which simplifies to the following rate expression (Eq. S43) for formation of individual xylenes:

$$\frac{r_{iX}}{[L]} = \frac{k_{iX}K_C P_{Toluene}}{1 + K_C P_{Toluene}} \quad \text{(S43)}$$

Similarly, the total xylenes formation rates are given by the expression:

$$\frac{r_{totalX}}{[L]} = \frac{k_{totalX}K_C P_{Toluene}}{1 + K_C P_{Toluene}} \quad \text{(S44)}$$

$$k_{totalX} = k_{pX} + k_{oX} + k_{mX} \quad \text{(S45)}$$

The kinetic parameters k_{iX} and K_C were estimated by non-linear regression of Equation S43 to the rate data which was performed as a global fit of the individual xylenes formation rates as a function of pressure using the Levenberg-Marquardt (LM) algorithm in OriginPro 2021. The results of these fits are reported in Table S4 and fitted curves are shown in Figures S14a,b to S19a,b.

Table S4. Summary of rate and equilibrium constants obtained from fitting rate data

Sample	K_C / kPa^{-1}	k_{pX} / 10^{-3} mol *p*-xylene (mol H^+ s)$^{-1}$	k_{mX} / 10^{-3} mol *m*-xylene (mol H^+ s)$^{-1}$	k_{oX} / 10^{-3} mol *o*-xylene (mol H^+ s)$^{-1}$	k_{totalX}[a] / 10^{-3} mol xylene (mol H^+ s)$^{-1}$
TON	0.55 (± 0.33)	0.00099 (± 0.00020)	0.00008 (± 0.00009)	0.00030 (± 0.00010)	0.00137 (± 0.00024)
MFI-EDA-1	1.01 (± 0.12)	0.0841 (± 0.0028)	0.0025 (± 0.0017)	0.0153 (± 0.0018)	0.102 (± 0.004)
MFI-DABCO-1	1.34 (± 0.20)	0.0914 (± 0.0034)	0.0014 (± 0.0022)	0.0247 (± 0.0023)	0.118 (± 0.005)
MFI-TPA-C	0.99 (± 0.30)	0.203 (± 0.032)	0.046 (± 0.028)	0.520 (± 0.050)	0.769 (± 0.065)
BEA-1[b]	0.65 (± 0.05)	0.407 (± 0.013)	0.196 (± 0.011)	0.878 (± 0.021)	1.53 (± 0.03)
BEA-2[b]	0.64 (± 0.12)	0.354 (± 0.027)	0.168 (± 0.023)	0.658 (± 0.038)	1.21 (± 0.06)
MCM-41	0.31 (± 0.04)	0.0037 (± 0.0003)	0.0018 (± 0.0002)	0.0066 (± 0.0004)	0.0121 (± 0.0005)

Uncertainty in measured kinetic and equilibrium constants represent two times the standard error.

[a] k_{totalX} obtained from sum of k_{iX} (Eq. 45)

[b] k_{TMB} is included in k_{totalX} for BEA samples and the values are respectively (0.053 ± 0.010) × 10^{-3} mol trimethylbenzene (mol H^+ s)$^{-1}$ and (0.032 ± 0.021) × 10^{-3} mol trimethylbenzene (mol H^+ s)$^{-1}$ for BEA-1 and BEA-2.

S5.8. Interpretation of rate constants using transition state theory

The measured rate constants during toluene methylation (Section S5.7) are further interpreted by depicting the sequence of elementary steps on a reaction coordinate diagram and using transition state formalisms to describe the rate constants in terms of the relative Gibbs free energies of the transition states and intermediates along the reaction coordinate. On active sites covered by DME-derived methoxy intermediates (CH_3–Z), the toluene co-adsorption (Eq. S32) and C–C bond formation (Eq. S33) steps are schematically represented in a reaction coordinate diagram (Scheme S2).

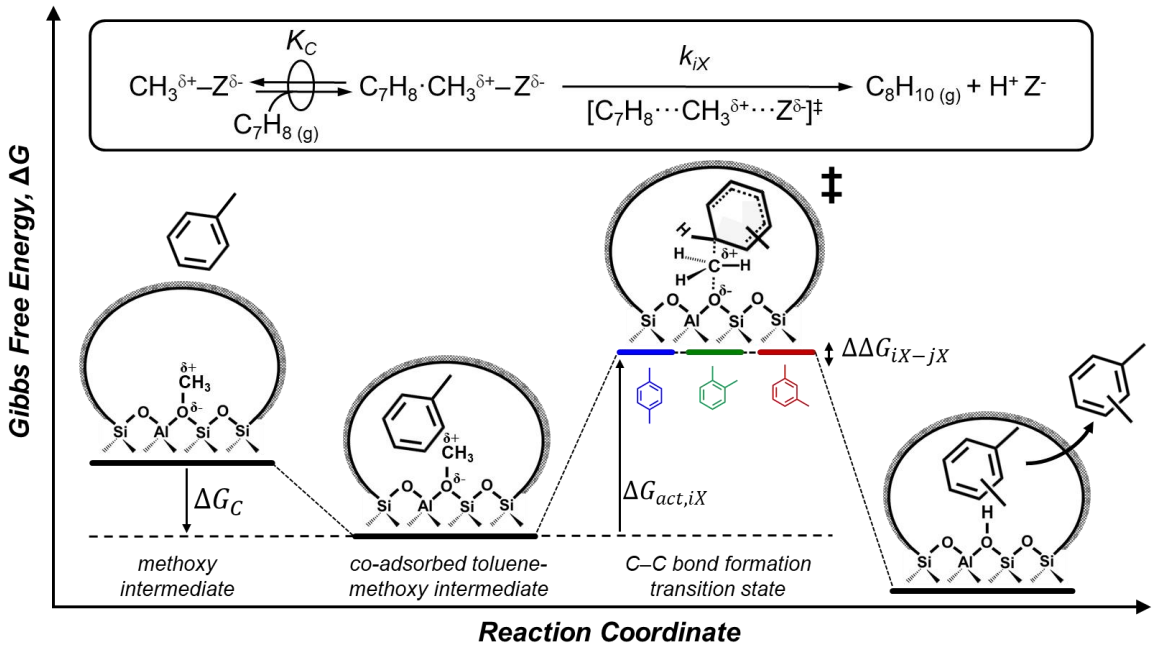

Scheme S2. Reaction coordinate diagram for toluene methylation on acid sites in zeolites covered with DME-derived surface methoxy species.

From the reaction coordinate diagram, ΔG_C and $\Delta G_{act,iX}$ are respectively the Gibbs free energies to co-adsorb toluene next to a surface methoxide intermediate and to form the kinetically relevant transition states from the co-adsorbed toluene-methoxide precursor. While the thermodynamic co-adsorption constant (K_C) reflects ΔG_C via Equation S46, the kinetic rate constant to form each xylene isomer (k_{iX}) is related to $\Delta G_{act,iX}$ through the formalism of transition state theory[61,62] (Eq. S47) where h and k_B represent Planck's and Boltzmann's constants, respectively. Equation S47 also accounts for the number of equivalent ring positions ($n_{C-C,i}$) in toluene that can form each xylene isomer.

$$K_C = e^{\frac{-\Delta G_C}{RT}} \tag{S46}$$

$$k_{iX} = n_{C-C,i}\frac{k_B T}{h} e^{\frac{-\Delta G_{act,iX}}{RT}} \tag{S47}$$

Rate constant ratios (k_{iX}/k_{jX}) reflect Gibbs free energy differences between individual xylene formation transition states ($\Delta\Delta G_{iX-jX}$) as shown in Equation S48 and are independent of the precursor state:

$$\frac{k_{iX}}{k_{jX}} = \frac{n_{C-C,i}}{n_{C-C,j}} e^{\frac{-\Delta\Delta G_{iX-jX}}{RT}} \quad \text{(S48)}$$

From the experimentally measured k_{iX} values (Section S5.7, Table S4) during toluene methylation (403 K, 0.2–8.8 kPa, 66–68 kPa DME) on various aluminosilicates, the k_{iX}/k_{jX} and $\Delta\Delta G_{iX-jX}$ values are calculated and summarized in Table S5.

Table S5. Rate constant ratios and Gibbs free energy differences for xylene formation transition states across aluminosilicates during toluene methylation (403 K, 0.2–8.8 kPa, 66 kPa DME).

Sample	k_{pX}/k_{oX}	k_{mX}/k_{oX}	$\Delta\Delta G_{pX-oX}$ / kJ mol^{-1}	$\Delta\Delta G_{mX-oX}$ / kJ mol^{-1}
TON	3.31 (± 0.67)	0.28 (± 0.16)	-6.3 (± 0.7)	4.3 (± 1.9)
MFI-EDA-1	5.49 (± 0.33)	0.16 (± 0.06)	-8.0 (± 0.2)	6.0 (± 1.2)
MFI-DABCO-1	3.71 (± 0.18)	0.06 (± 0.04)	-6.7 (± 0.2)	9.5 (± 2.5)
MFI-TPA-C	0.39 (± 0.04)	0.09 (± 0.03)	0.8 (± 0.3)	8.1 (± 1.0)
BEA-1	0.46 (± 0.01)	0.22 (± 0.01)	0.3 (± 0.1)	5.0 (± 0.1)
BEA-2	0.54 (± 0.03)	0.25 (± 0.02)	-0.3 (± 0.2)	4.6 (± 0.2)
MCM-41	0.55 (± 0.03)	0.27 (± 0.02)	-0.3 (± 0.2)	4.3 (± 0.2)

Uncertainties reflect one standard error obtained from propagating standard errors in fitted rate constants (Table S4) using established error propagation formula.

S5.9. Assessment of influence of external acid sites

The influence of external acid sites on measured rates and selectivity during toluene methylation with methanol and DME was assessed using 2,6-di-*tert*-butylpyridine (DTBP; ~0.80 nm kinetic diameter) to selectively poison external Brønsted acid sites that are located at crystallite surfaces of medium-pore (~0.55 nm diameter) zeolites such as MFI[63]. The bulky *tert*-butyl groups prevent both DTBP access to micropores and coordination to Lewis acid centers, but allow protonation by Brønsted acid sites. After establishing steady-state rates (2 kPa toluene, 4 kPa methanol, 403 K), DTBP was co-fed (20 Pa) on MFI-TPA-C as shown in Figure S20.

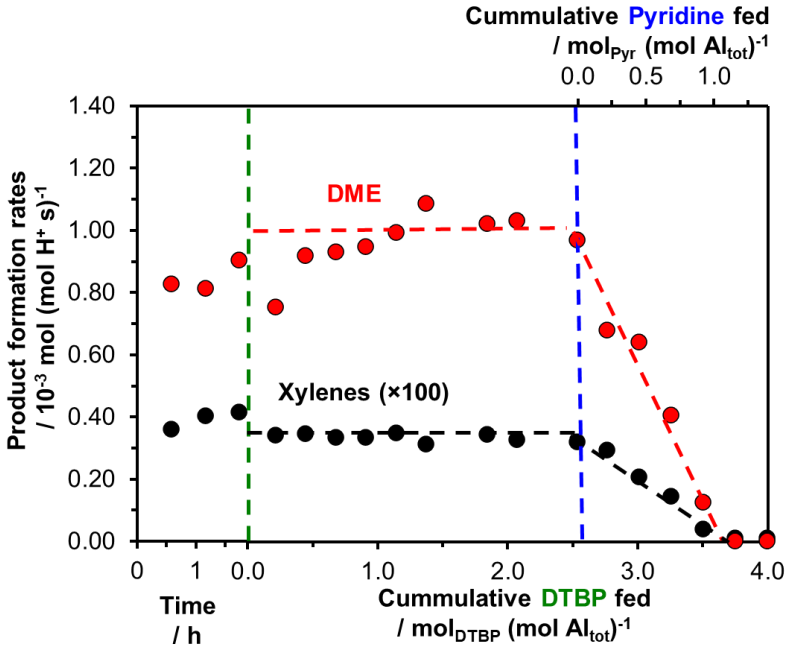

Fig. S20. Xylenes and DME STY before and after titrant introduction (20 Pa DTBP and 20 Pa Pyridine) during toluene methylation on MFI-TPA-C at 2 kPa toluene, 4 kPa methanol 403 K.

During the 5 h time-on-stream of co-fed DTBP (corresponding to 2.5 moles of DTBP fed per total Al), no significant change (<10%) was observed for both the total xylenes formation rates from toluene methylation and DME formation rates (from parallel methanol dehydration). While maintaining DTBP cofeeds, pyridine was introduced (20 Pa) as a non-selective titrant of all acid site types to further confirm that measured rates predominantly reflect internal acid sites. Xylenes and DME formation rates decreased linearly with increasing cumulative moles of pyridine fed. The similarity of the amount of fed pyridine needed to completely suppress rates (Pyridine/Al ≈ 0.9) and the *ex-situ* H^+ site titration (NH_4^+/Al = 0.85) indicate that majority (>85%) of the H^+ present in MFI-TPA-C are located within microporous domains and contribute similarly to both methylation and dehydration rates. In addition, as shown in Figure S21, there are negligible changes (<10%) to individual xylenes formation rates before and after DTBP (20-40 Pa) introduction during toluene methylation (2 kPa toluene, 4 kPa methanol, 403 K) on MFI-TPA-C and MFI-TPA-C-2, while pyridine introduction suppresses the formation rate of all three xylenes. These insights on the negligible effects of external acid sites during toluene methylation with methanol on MFI-TPA-C and MFI-TPA-C-2 (surmised to be synthesized with TPA^+) are expected to hold for other MFI-TPA samples (*ortho*-selective) as well as for toluene methylation with DME.

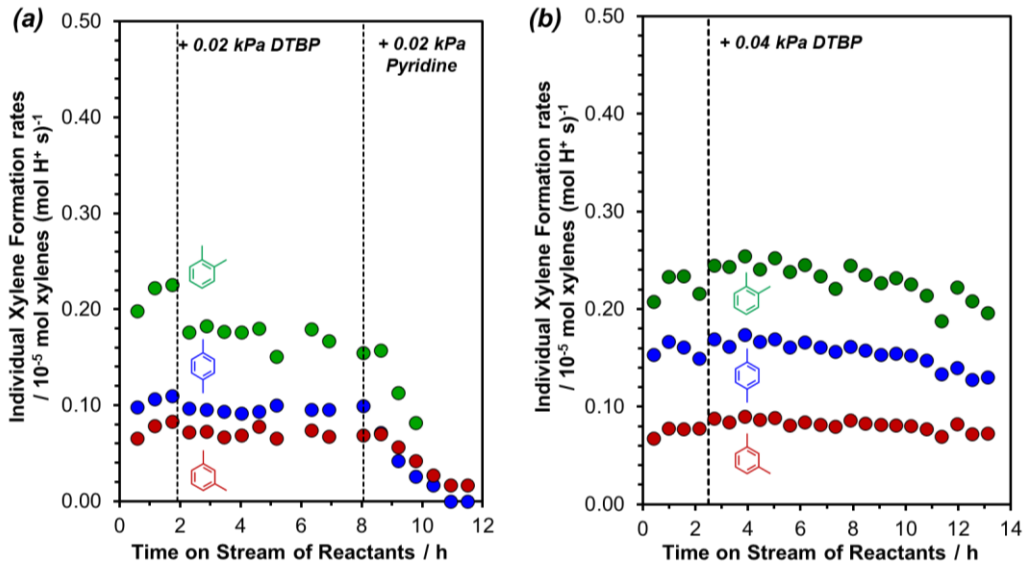

Fig. S21. Individual xylenes formation rates vs time-on-stream during toluene methylation (2 kPa toluene, 4 kPa DME, 403 K) before and after titrant (20-40 Pa DTBP, 20 Pa Pyridine) introduction on **(a)** MFI-TPA-C **(b)** MFI-TPA-C-2. Because of an overlap of the pyridine GC peak and *o*-X GC peak, the actual *o*-X formation rates could not be quantified past 10 h time-on-stream (0.7 moles Pyridine fed per Al) during pyridine cofeeds.

Similarly, during toluene methylation with DME on MFI-TPA-C (Fig. S22a), the initial rates were similar (within 5%) with or without DTBP cofeed, however the rates at much longer times on stream, were significantly lower (e.g., by 2× at 10 h time-on-stream). On the other hand, the xylene selectivity profile across the entire time on stream remained unperturbed by the presence of DTBP in the reactant feed (Fig. S22b). These results further indicate that external acid sites play a negligible role during toluene methylation with DME at initial times but become significant at much later times on stream when access to the internal acid sites are restricted by bulky polymethylbenzenes that deactivate the MFI zeolite. We further show in Figure S23–S24 that external acid sites also have a negligible influence on initial measured rates and selectivity during toluene methylation with DME on MFI-DABCO-1 and MFI-EDA-3. However, at later times on stream when the internal acid sites have been significantly deactivated by the slowly accumulating bulky polymethylbenzenes (i.e., when the ratio of instantaneous rates to initial rates is less than 20%), the external acid sites start to significantly contribute to observed xylene selectivity. The ability of DTBP to selectively poison Brønsted acid sites in external (unconfined) environment is further confirmed by co-feeding DTBP during toluene methylation in MCM-41, a mesoporous amorphous aluminosilicate. As shown in Figure S25. during DTBP cofeed (5 Pa) in MCM-41, the xylenes formation rates are completely suppressed by DTBP, confirming that DTBP is an appropriate titrant for external acid sites in MFI and that observed toluene methylation rates in all aluminosilicates in this study are solely because of Brønsted acid sites and not the Lewis acid sites.

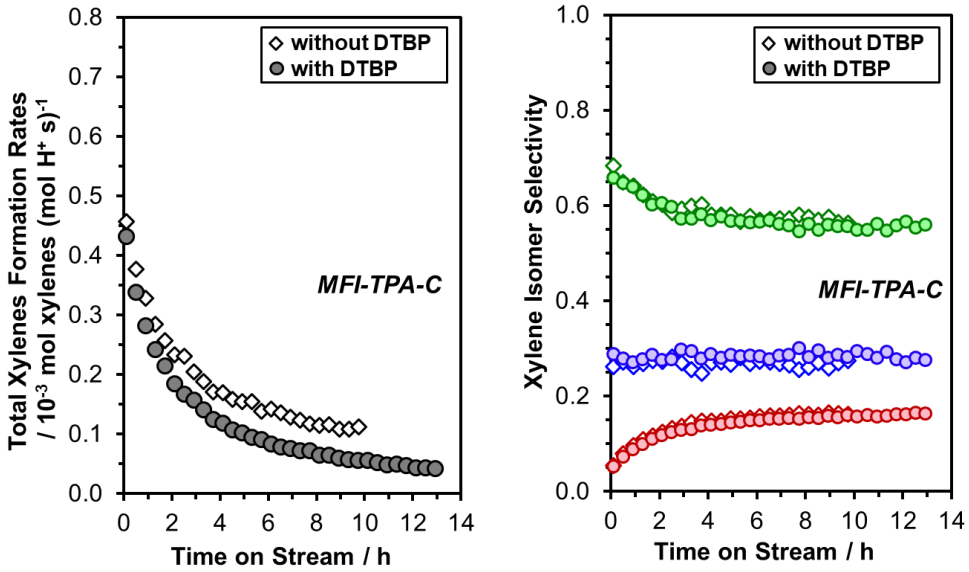

Fig. S22. (a) Product formation rates and (b) xylene isomer selectivity as a function of time-on-stream during toluene methylation (4.0 kPa toluene, 68 kPa DME, 403 K) with and without DTBP cofeed (10 Pa DTBP) on MFI-TPA-C.

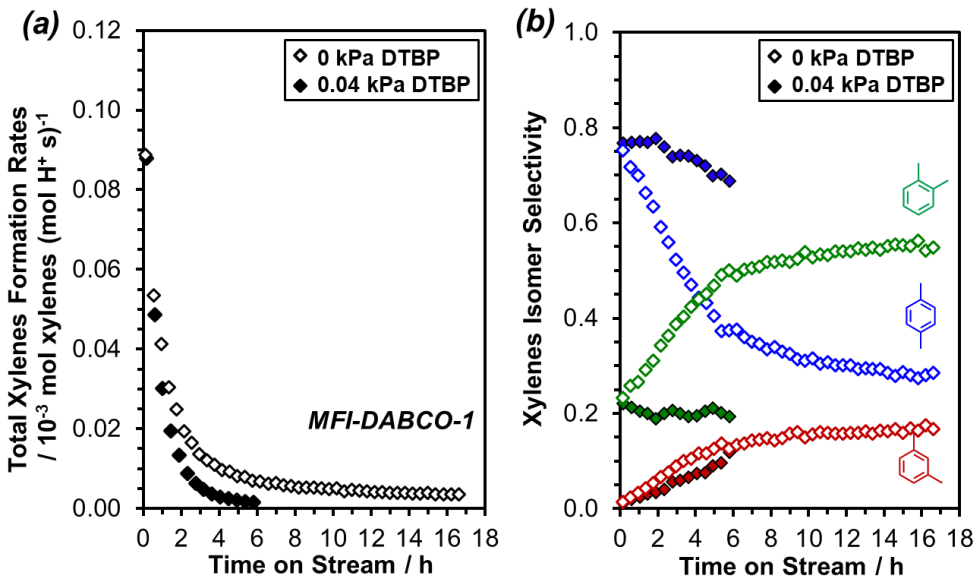

Fig. S23. (a) Product formation rates and (b) xylene isomer selectivity as a function of time-on-stream during toluene methylation (4.5 kPa toluene, 68 kPa DME, 403 K) with and without DTBP cofeed (40 Pa DTBP) on MFI-DABCO-1.

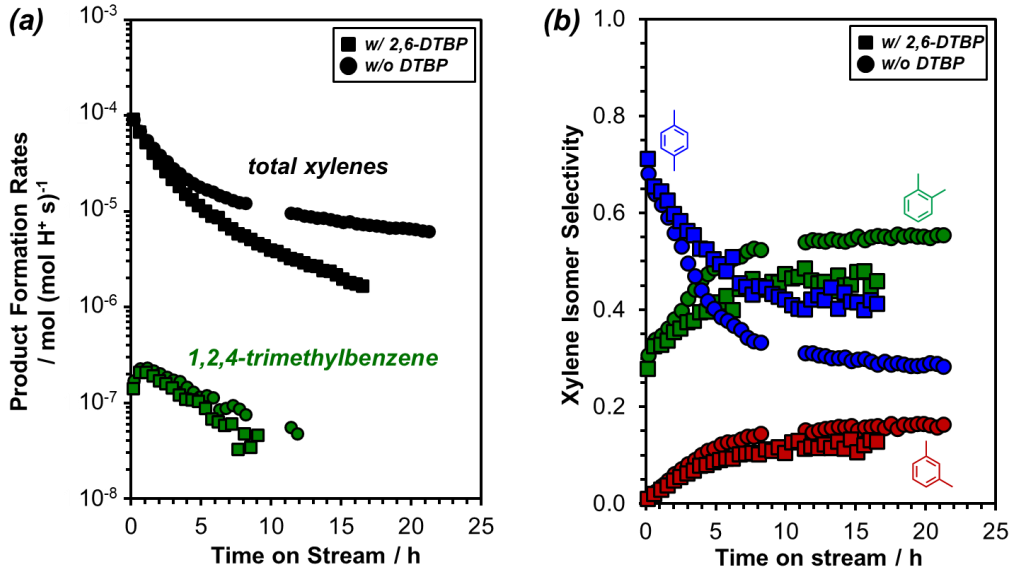

Fig. S24. (a) Product formation rates and (b) xylene isomer selectivity as a function of time-on-stream during toluene methylation (4.5 kPa toluene, 68 kPa DME, 403 K) with and without DTBP cofeed (22 Pa DTBP) on MFI-EDA-3.

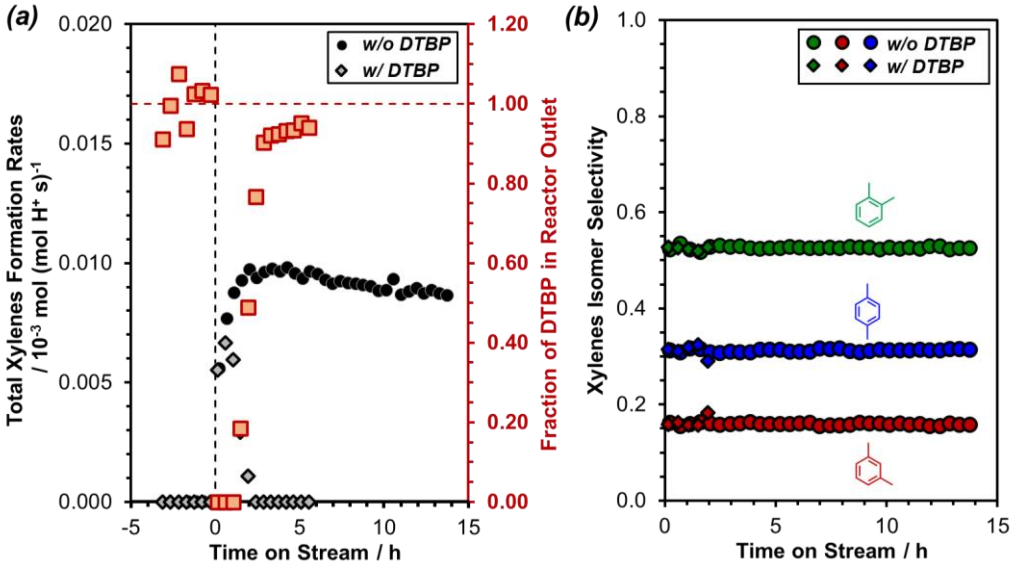

Fig. S25. (a) Total xylenes formation rates and (b) xylene isomer selectivity as a function of time-on-stream during toluene methylation (4.0 kPa toluene, 66 kPa DME, 403 K) with and without DTBP cofeed (5 Pa DTBP) on MCM-41.

Furthermore, we show that during toluene methylation on TON, there are significant contributions of external acid sites to observed rates and selectivity as shown in Fig. S26. The observed rate on TON (2.9×10^{-6} mol xylenes (mol H^+ s)$^{-1}$) is lower than the methylation rate on external acid sites on MCM-41 (1.0×10^{-5} mol xylenes (mol H^+ s)$^{-1}$). Thus, DTBP cofeeds (20 Pa) were required to eliminate the contributions of external acid sites to observed rates and selectivity.

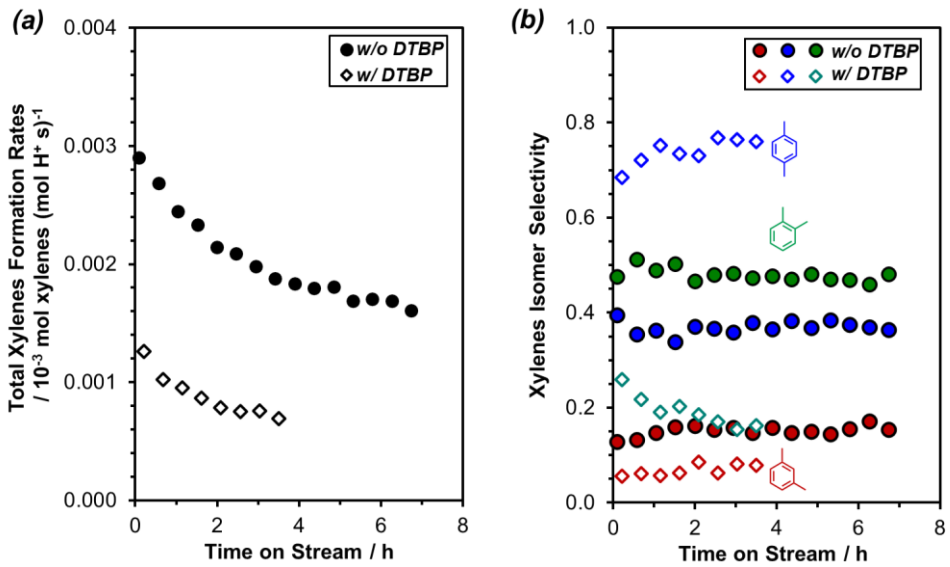

Fig. S26. (a) Total xylenes formation rates and (b) xylene isomer selectivity as a function of time-on-stream during toluene methylation (4.0 kPa toluene, 66 kPa DME, 403 K) with and without DTBP cofeed (20 Pa DTBP) on TON. For both cases, the xylene formation rates are normalized by the bulk proton content obtained using ammonium TPD.

S5.10. Assessment of effects of B incorporation during MFI synthesis

Previous reports from our group identified the incorporation of B atoms (via boric acid) in the synthesis gel as a strategy to influence MFI crystallite size independently of Al content and proximity[1,4]. The catalytic irrelevance of protons that charge-compensate framework B (H_B^+) in boroaluminosilicates was demonstrated in one of those previous reports by measuring methanol dehydration rates that depend only on protons that charge-compensate Al (H_{Al}^+).[4] Those findings were consistent with previous studies[64–66] that concluded that H_B^+ are typically catalytically irrelevant relative to H_{Al}^+ because the deprotonation energy of H_B^+ is ~70 kJ/mol greater than that of H_{Al}^+ [64]. Herein, we observe similar catalytic irrelevance of H_B^+ on toluene methylation rates and xylene isomer selectivity. From the similar xylenes formation rates (per H_{Al}^+) and selectivity on both MFI-EDA-1,4 (2–4 B/unit cell; Table S6) and MFI-EDA-2,3 (0 B/unit cell; Table S6), we infer H_B^+ negligibly influences toluene methylation in the boroaluminosilicates synthesized using mixtures of EDA and TPA^+ (MFI-EDA-1, MFI-EDA-4). Similar toluene methylation behavior on MFI-TPA-1,3 (0 B/unit cell; Table S6) and MFI-TPA-2,4 (0.1–2 B/unit cell; Table S6) also support the conclusion that the presence of B heteroatoms in boroaluminosilicates synthesized using TPA^+ only (MFI-TPA-2, MFI-TPA-4) have negligible consequences for toluene methylation rates and selectivity under the study conditions.

Table S6. Al and B contents of MFI samples in this study.

Sample	Al per unit cell[a]	B per unit cell[a]
MFI-TPA-C	2.2	-
MFI-TPA-1	1.9	-
MFI-TPA-2	1.6	2.0
MFI-TPA-3	1.7	-
MFI-TPA-4	2.2	0.1
MFI-TPA-C666	1.9	-
MFI-EDA-1	1.7	3.5
MFI-EDA-2	1.6	-
MFI-EDA-3	2.0	-
MFI-EDA-4	1.7	1.8
MFI-DABCO-1	2.1	-
MFI-DABCO-2	2.1	-

[a]Calculated from elemental analysis (ICP-OES (Si, Al, B) or AAS (Al)) and unit cell formula. Uncertainties are 10%
"-" indicates B content was neither detected nor measured because of absence of B in synthesis solution.

S5.11. Assessment of Al proximity effects

The influence of Al proximity was assessed to eliminate the alternative hypothesis that Al proximity influences observed toluene methylation rates and selectivity. Among the suite of MFI with similar Al contents (Si/Al~50; 1.6–2.2 Al per unit cell), the fraction of proximal anionic Al ($AlO_{4/2}^-$) were measured by previously reported and validated cobalt divalent ion (Co^{2+}) titration techniques [1,2]. Co^{2+} aqueous ion-exchanges were performed using 150 cm^3 of 0.5 M $Co(NO_3)_2$ (Sigma Aldrich, 98%) solution per gram of Na-form zeolite while stirring at 353 K for 24 h. Sodium ion (Na^+) exchanges were performed using 150 cm^3 of 1 M NaCl (Sigma-Aldrich, 99.9%) solution per gram of zeolite while stirring at ambient conditions for 24 h. Among the MFI samples, the fraction of proximal Al varied from 1% to 76% (Table S7). These fraction of proximal Al reflects only the Al-Al site pair ensembles that are Co^{2+} titratable and does not necessarily reflect the length scale between adjacent protons that may be more relevant for catalysis[67].

Table S7. Al and H^+ contents, and Co uptake values of MFI samples in this study.

Sample	MFI-TPA-C	MFI-TPA-1	MFI-TPA-2	MFI-TPA-3	MFI-TPA-4	MFI-TPA-C666	MFI-EDA-1	MFI-EDA-2	MFI-EDA-3	MFI-DABCO-1	MFI-DABCO-2
Si/Al	43	50	59	55	42	47	53	58	49	44	44
Al/u.c.	2.1	1.9	1.6	1.7	2.2	2.0	1.7	1.6	2.0	2.1	2.1
H_{Al}^+/u.c.	1.8	1.9	1.3	1.7	1.8	1.6	1.7	1.5	1.2	2.0	1.9
$2\times Co^{2+}$/Al	0.46	0.24	0.20	0.44	0.30	0.76	0.01	0.01	0.01	0.14	0.06

Across all MFI samples, the initial xylene isomer selectivity and total xylenes formation rates did not systematically vary with the fraction of Co^{2+}-titratable Al ($2\times Co^{2+}$/Al) (Fig. S27a). Within the MFI-TPA-X subset, the xylene isomer selectivity (Fig. S27b) remained invariant of fraction of proximal Al (0.20–0.76) and the xylenes formation rates did not show a systematic dependence on the proximal Al content. Similarly, within the MFI-EDA and MFI-DABCO subset, the xylene isomer selectivity and total formation rates did not exhibit any discernible trends with fraction of proximal Al (0.01–0.14).

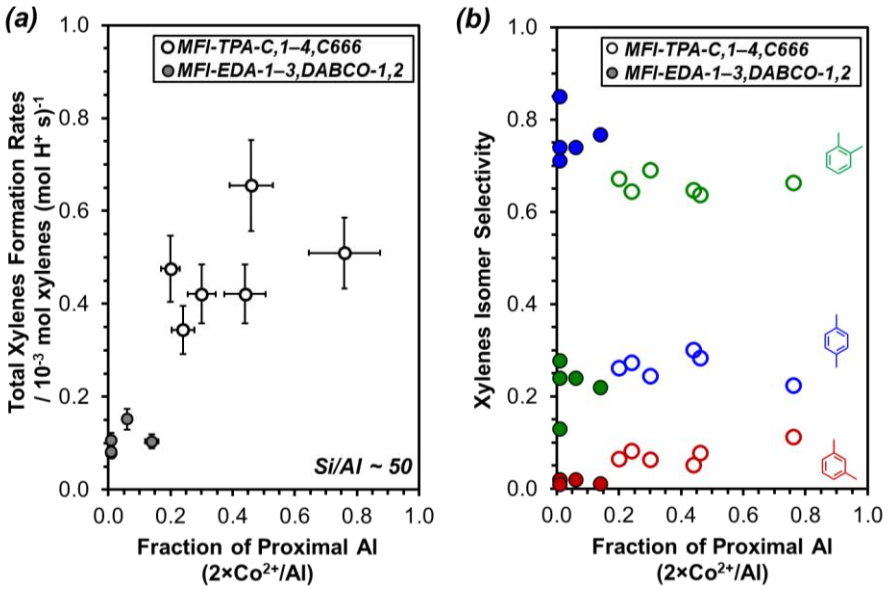

Fig. S27. (a) Total xylenes formation rates and (b) xylene isomer selectivity as a function of fraction of proximal Al during toluene methylation (4.0-4.4 kPa toluene, 66 kPa DME, 403 K) on MFI samples of similar Al content (Si/Al ~ 50; ~1.9 Al per unit cell).

The effects of proximal Al content on toluene methylation were further accessed on another commercial MFI (Zeolyst CBV28014; denoted here as MFI-TPA-C2) with isolated Al ($2\times Co^{2+}$/Al = 5%) as a result of the dilute Al content (Si/Al 134; 0.7 Al per unit cell) and surmised to be synthesized using the conventional TPA^+ organic SDA. The xylene isomer selectivity on MFI-TPA-C2 was similar to that observed on MFI-TPA-C (46% proximal Al), the representative sample in MFI-TPA-*Y* subset, as well as on the suite of other MFI-TPA samples with significant fractions of proximal Al (0.20–0.76) (Fig. S28b). Although, the initial total xylene formation rate on MFI-TPA-C2 was 3× lower than that on MFI-TPA-C, it is also 3× higher than that on MFI-EDA-1, the representative sample in the MFI-EDA and MFI-DABCO subset (Fig. S28b).

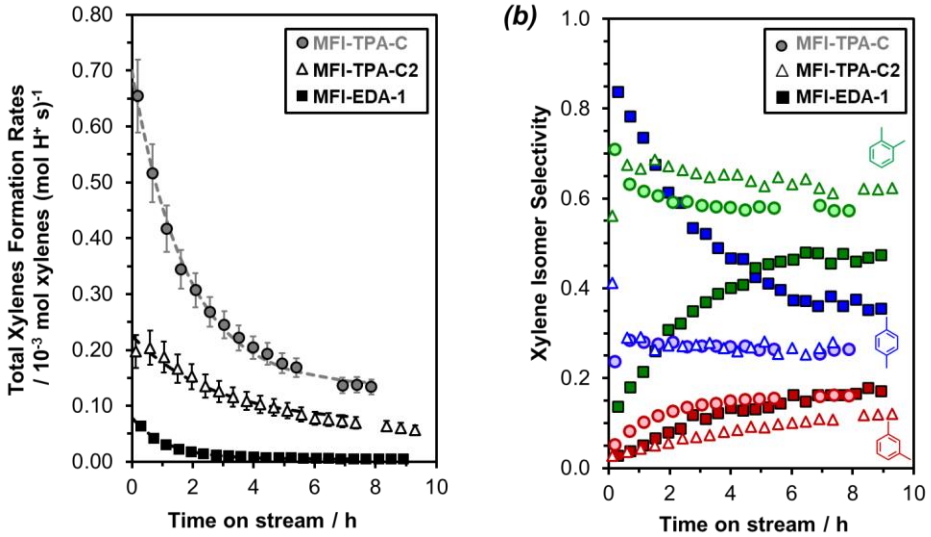

Fig. S28. (a) Total xylenes formation rates and (b) xylene isomer selectivity as a function of time-on-stream (4.0 kPa toluene, 66 kPa DME, 403 K, 4.4–7.6 mol H^+·s (mol toluene)$^{-1}$) on MFI-TPA-C (Si/Al 43), MFI-TPA-C-2 (Si/Al 134), MFI-EDA-1 (Si/Al 53).

We further studied Beta (BEA) zeolite to access the potential influence of Al proximity without the convoluting effects of multiple MFI void environments. Comparison of BEA-2 (Si/Al 13; 4.6 Al per unit cell; $2\times Co^{2+}/Al$ = 0.70) and BEA-1 (Si/Al 93; 0.7 Al per unit cell) showed similar xylene isomer selectivities (within 3%) and insignificant differences in the total xylene formation rate constant (k_{totalX}, within 1.2×) and co-adsorption constant (K_C, 0.95×) (See Fig. S17; Table S4, Table S8). Taken together, the influence of Al proximity on the measured xylene isomer selectivity and total formation rates were found to be negligible under the current study conditions.

Table S8. Summary of characterization data and catalytic data on BEA samples in this study

	Si/Al	Al / u.c.	H^+ / u.c.	$2\times Co^{2+}/Al$	Initial xylene selectivity (*p*-X : *m*-X : *o*-X)	k_{totalX} / 10^{-3} mol xylenes (mol H^+ s)$^{-1}$	K_C / kPa^{-1}
BEA-1	93	0.7	0.6	n.m.	0.28 : 0.13 : 0.58	1.53 ± 0.03	0.65 ± 0.05
BEA-2	13	4.6	3.0	0.70	0.31 : 0.15 : 0.56	1.21 ± 0.06	0.64 ± 0.12

Uncertainty in measured kinetic and equilibrium constants represent two times the standard error.

S5.12. Analyses of local environments of framework Al atoms from solid-state ^{27}Al MAS NMR

Solid-state ^{27}Al MAS NMR spectra are sensitive to differences in the local coordination environments of ^{27}Al nuclei, which are manifested by differences in the positions (i.e., frequencies) and lineshapes of ^{27}Al NMR signals. As shown in Figure S29A, the solid-state 1D ^{27}Al MAS NMR spectrum of MFI-TPA-3 exhibits two regions of intensity centered at 56 ppm and 0 ppm, which respectively correspond to tetrahedrally coordinated framework Al^{IV} species and octahedrally coordinated extra-framework Al^{VI} species. Similarly, ^{27}Al MAS NMR spectra were acquired under identical conditions (described in Section S2) for other MFI samples that were synthesized using different OSDAs (Fig. S30). The fraction of observed ^{27}Al NMR signal attributable to framework Al^{IV} for each MFI sample is summarized in Table 1 (main text) and shows no noticeable trend between different MFI preparations. Although certain framework Al sites in some zeolite framework topologies[68–71] can be partially resolved, the 12 crystallographically distinct T-sites in the orthorhombic MFI structure with subtly different local coordination environments result in ^{27}Al signals that are too close to be unambiguously resolved experimentally[72–75]. Furthermore, the influence of framework defects or distributions of local environments near Al atoms contributes to the resolution challenges that preclude assignments of spectral features to specific T-sites.

Nevertheless, MFI samples synthesized under different conditions, including with different OSDAs, yield $^{27}Al^{IV}$ NMR signals with subtly different lineshapes that suggest different distributions of Al atoms within their respective MFI frameworks. Figure S29B shows 1D direct-excitation ^{27}Al MAS NMR spectra for MFI-TPA-3, MFI-EDA-2, MFI-DABCO-2, and MFI-TPA-C666 that contain similar $^{27}Al^{IV}$ signal intensity in the 50–60 ppm range. The spectra exhibit similar shoulder-like features at 53, 54, 56, and 58 ppm, with subtle differences in their relative intensities at 53 and 54 ppm. Thus, the ^{27}Al MAS NMR analyses indicate that the MFI samples synthesized using various organic structure-directing agents manifest modest qualitative differences in their respective distributions of framework Al coordination environments, though the ^{27}Al NMR spectra are not sufficiently resolved to permit the relative populations of Al atoms to be assigned to specific zeolite framework sites.

The connectivity of framework aluminum within the zeolite framework can be further understood through solid-state 2D ^{27}Al–^{29}Si *J*-mediated MAS NMR correlation spectra[76]. Each spectrum represents a 2D frequency map of correlated signals that arise only from ^{27}Al and ^{29}Si nuclei that are *J*-coupled through ^{27}Al–O–^{29}Si covalent bonds. Such spectra thus provide information on the locations and distributions of framework Al atoms based on differences in their local bonding environments with *J*-coupled ^{29}Si moieties. Representative solid-state 2D ^{27}Al–^{29}Si *J*-mediated correlation NMR spectra of MFI-TPA-1 and MFI-EDA-3 are shown in Figure S31A,B. Both spectra show a region of correlated intensity between a signal at 54 ppm in the ^{27}Al dimension, corresponding to four-coordinate framework $^{27}Al^{IV}$ species, and a signal centered at –105 ppm (ranging from –102 ppm to –111 ppm) in the ^{29}Si dimension, assigned to a distribution of Q^4(1Al) ^{29}Si chemical framework environments. The relatively broad distribution of ^{29}Si intensity associated with these Q^4(1Al) species results from a distribution of nearby Al T-site occupancies that produce local differences in Q^4(1Al) bonding environments. Due to the large number of T-sites in MFI, subtly different 2D signals from *J*-coupled ^{27}Al–O–^{29}Si moieties are not resolved between the two MFI samples, further underscoring the challenges of experimentally detecting differences in aluminum T-site distributions.

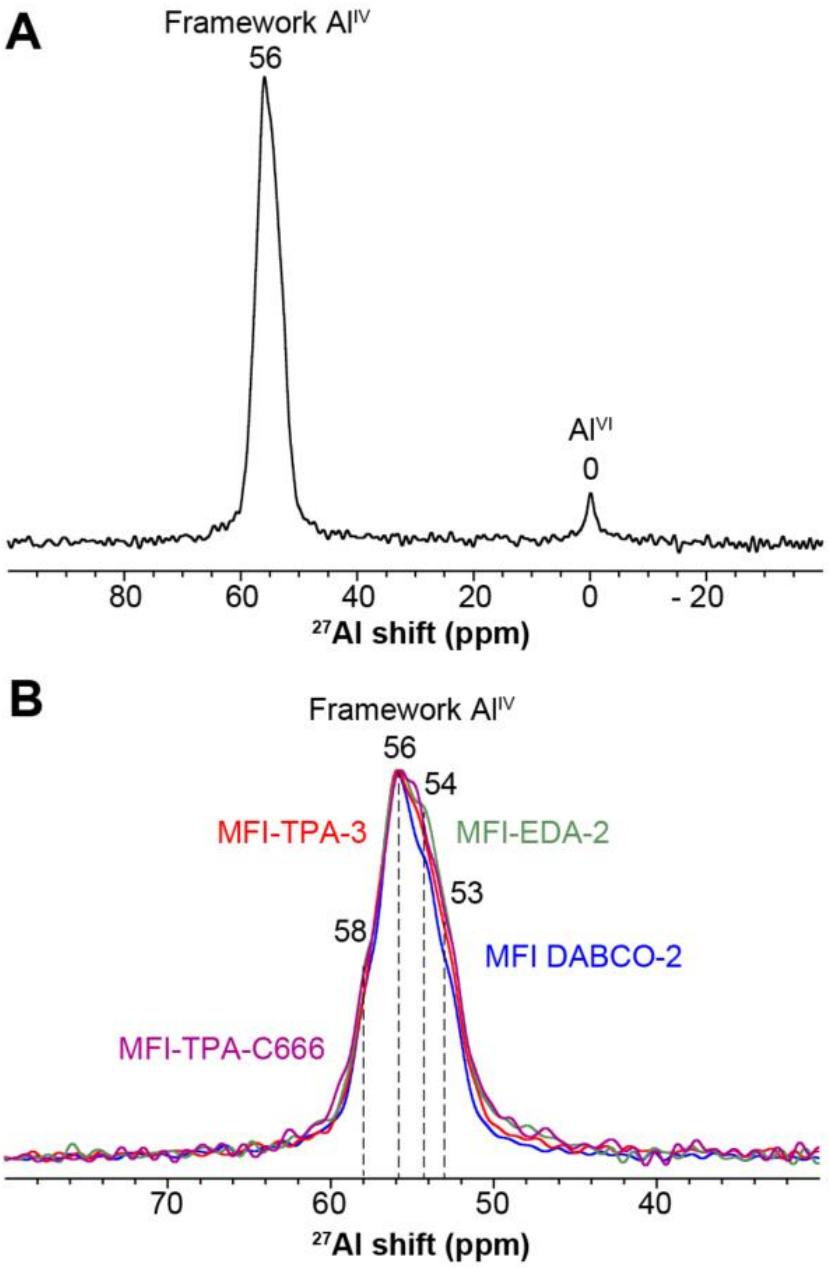

Fig. S29. Solid-state 1D direct-excitation ^{27}Al MAS NMR spectra of hydrated MFI zeolite TPA-3 (A) showing well-resolved signals from Al^{IV} framework moieties and Al^{VI} extra-framework species and (B) comparing the ^{27}Al lineshapes that correspond to framework Al^{IV} species in hydrated MFI-TPA-3 (red), MFI-EDA-2 (green), MFI-DABCO-2 (blue), and MFI-TPA-C666 (purple). All spectra were acquired at 18.8 T and 30 kHz MAS at room temperature.

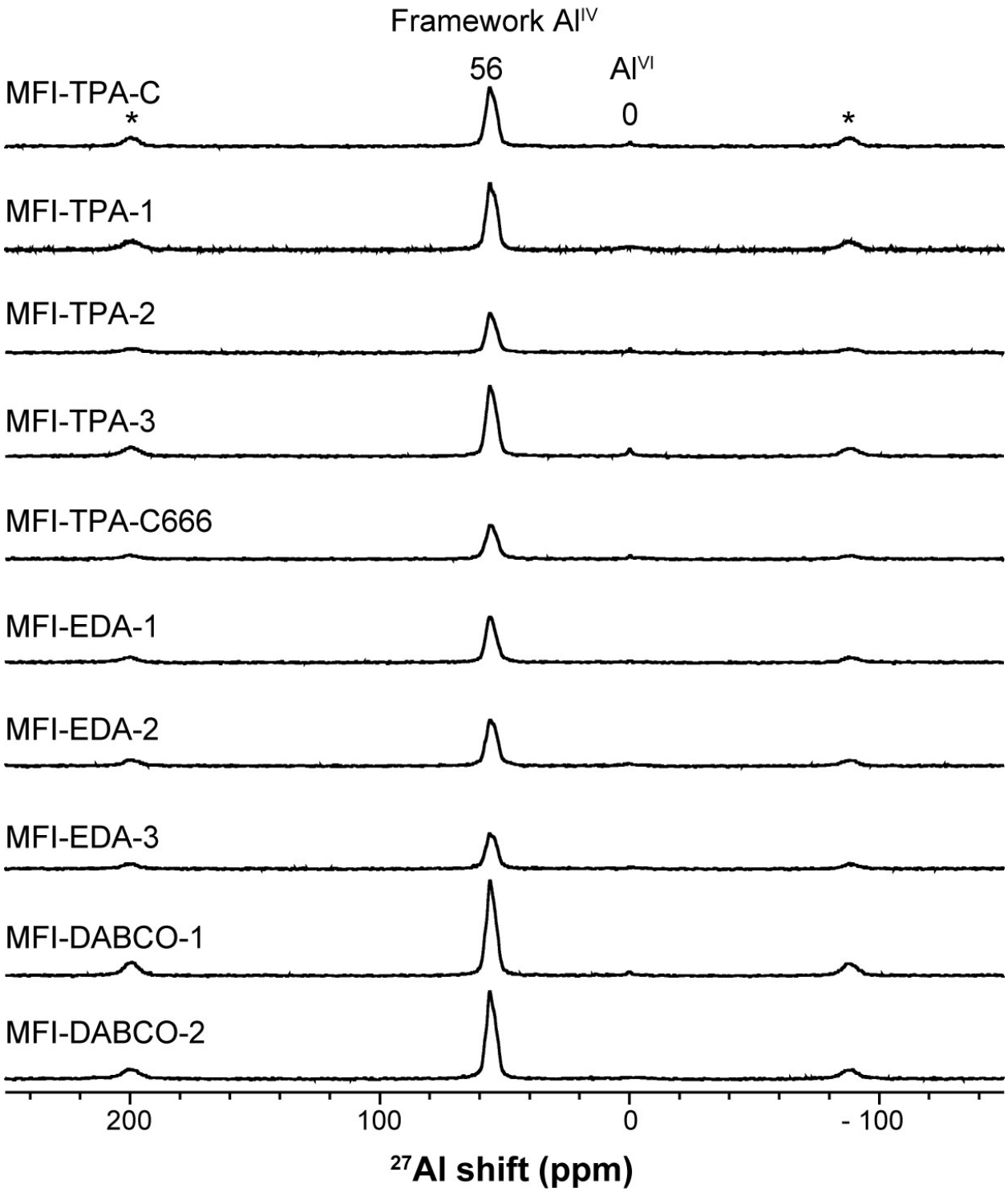

Figure S30. Solid-state 1D direct-excitation ^{27}Al MAS NMR spectra of MFI zeolites synthesized with different organic structure-directing agents. Asterisks (*) represent spinning sidebands of the $^{27}Al^{IV}$ signal at 56 ppm. All samples were measured in the H^+-form and were fully hydrated. All spectra were acquired at 18.8 T and 30 kHz MAS at room temperature.

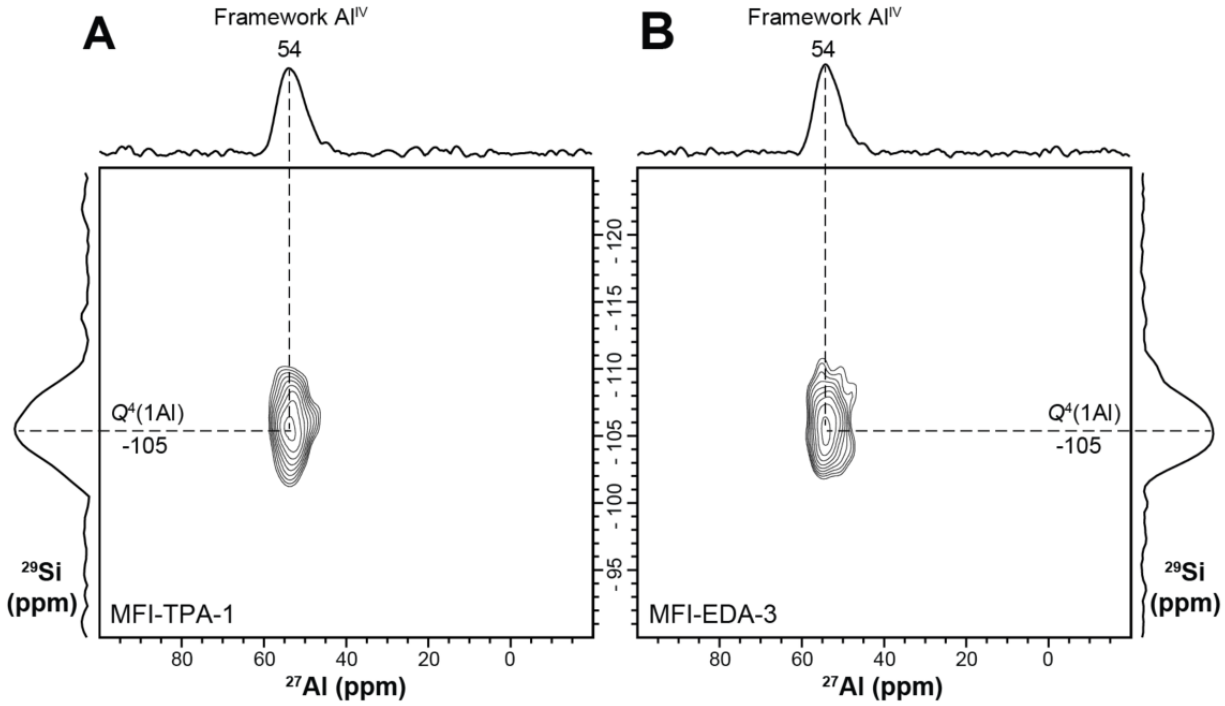

Fig. S31. Solid-state 2D ^{27}Al–^{29}Si *J*-HMQC MAS NMR spectra of (A) hydrated MFI-TPA-1 and (B) hydrated MFI-EDA-3. Projected ^{27}Al intensity is shown on top of each spectrum and projected ^{29}Si intensity is shown along the vertical axes. The spectra were acquired at 9.4 T, 100 K, and 8 kHz MAS.

S5.13. Summary of characterization of MFI samples and other aluminosilicates in this study

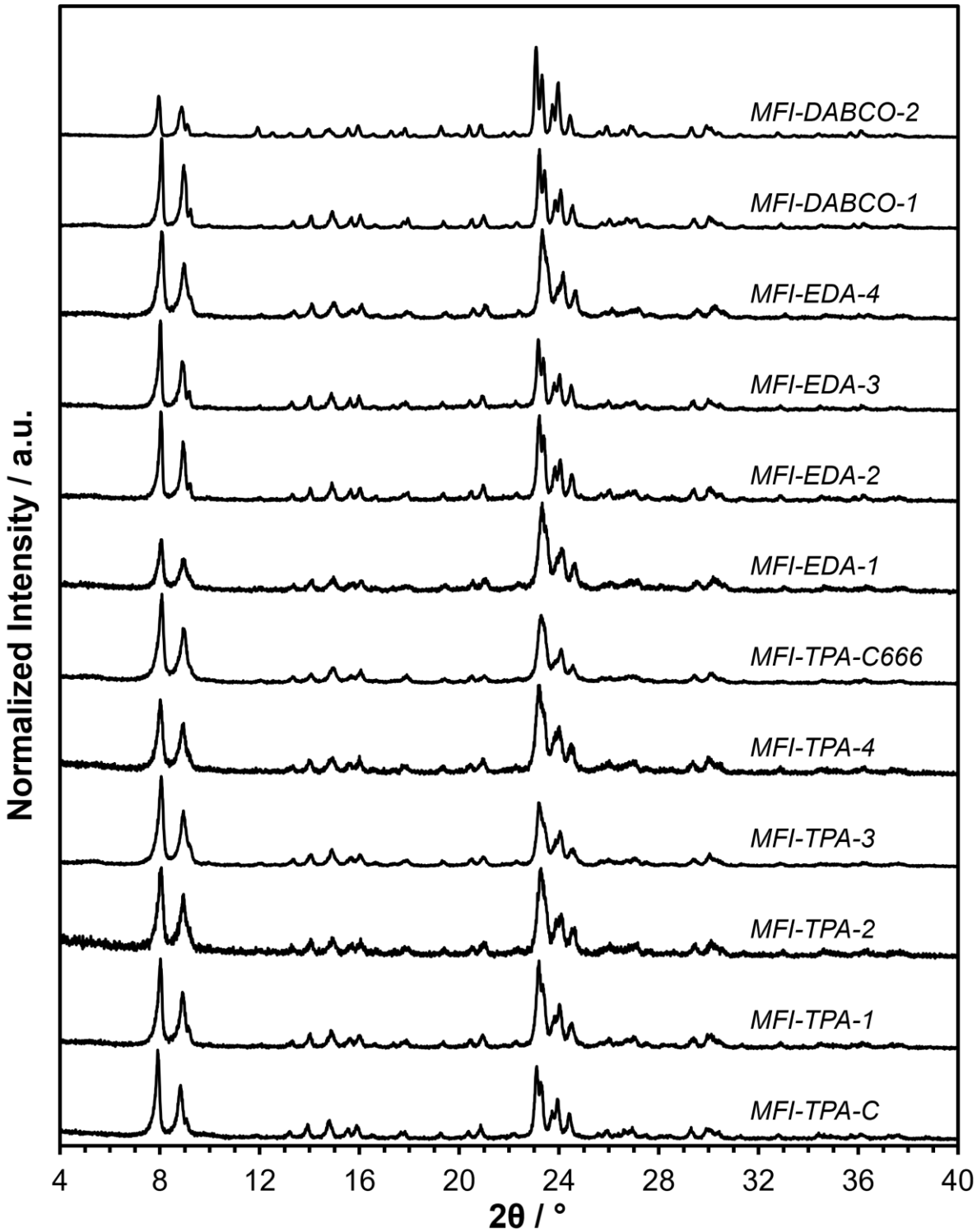

Fig. S32. XRD patterns of MFI samples of varied synthetic provenance. Diffraction patterns are vertically offset for clarity

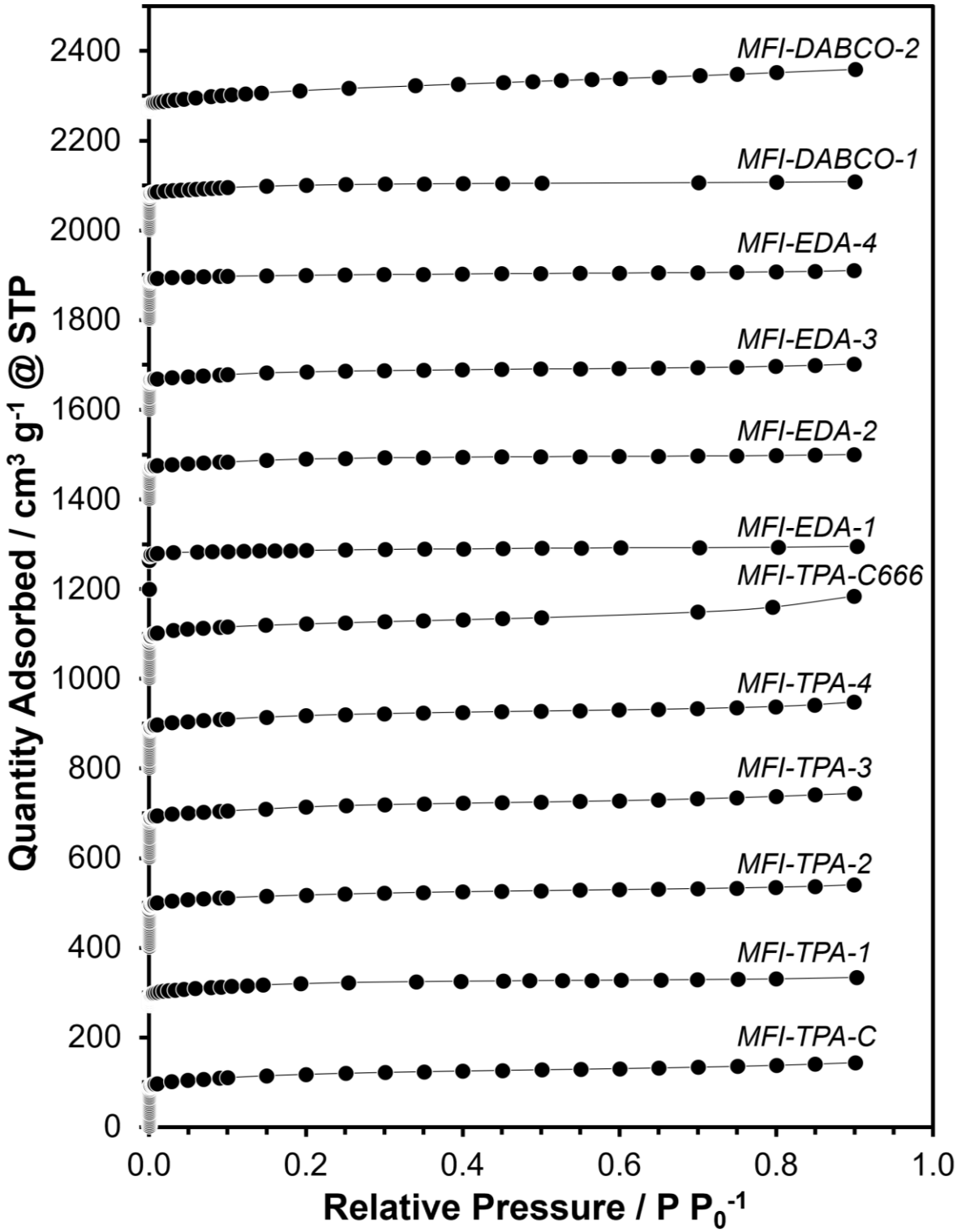

Fig. S33. N_2 adsorption isotherms (77 K) of MFI samples of varied synthetic provenance. Isotherms are vertically offset by 200 cm^3 g^{-1} for clarity.

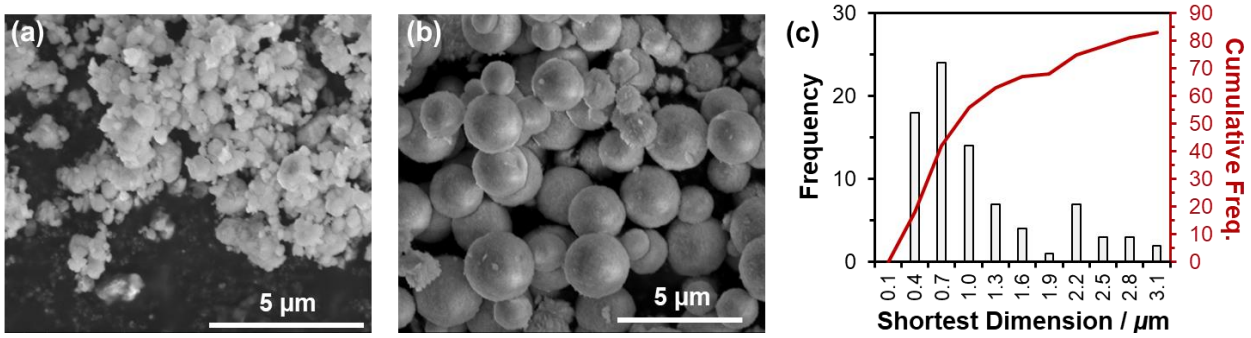

Fig. S34. (a-b) SEM images and (c) crystallite size distribution of MFI-TPA-C

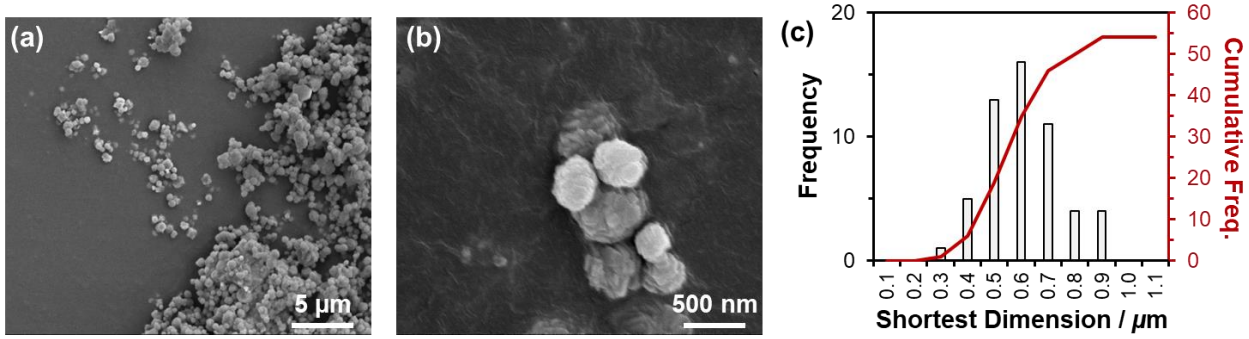

Fig. S35. (a-b) SEM images and (c) crystallite size distribution of MFI-TPA-1

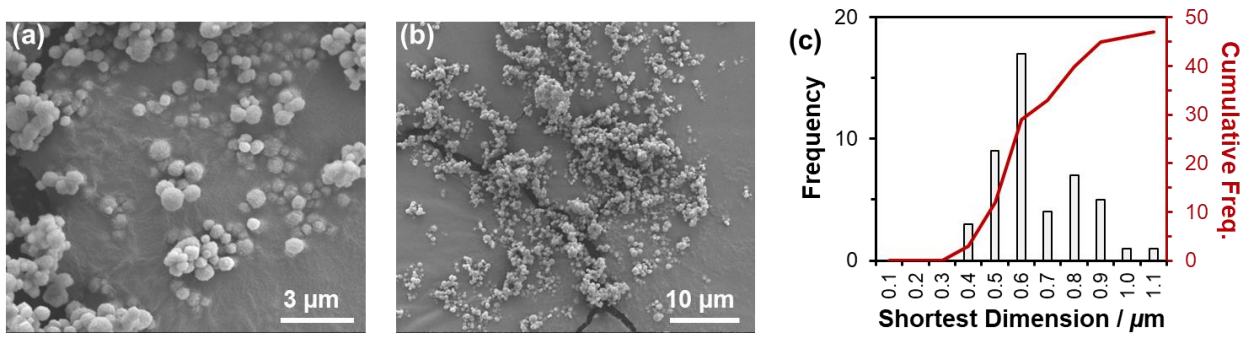

Fig. S36. (a-b) SEM images and (c) crystallite size distribution of MFI-TPA-2

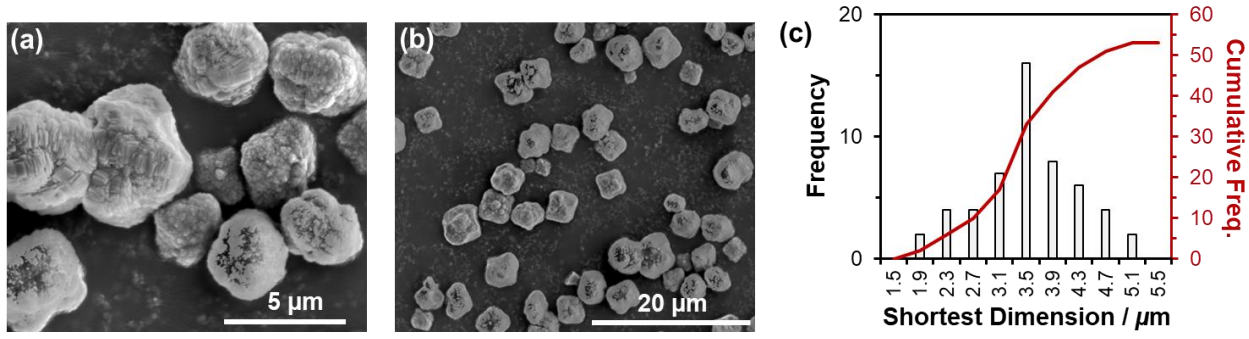

Fig. S37. (a-b) SEM images and (c) crystallite size distribution of MFI-TPA-3

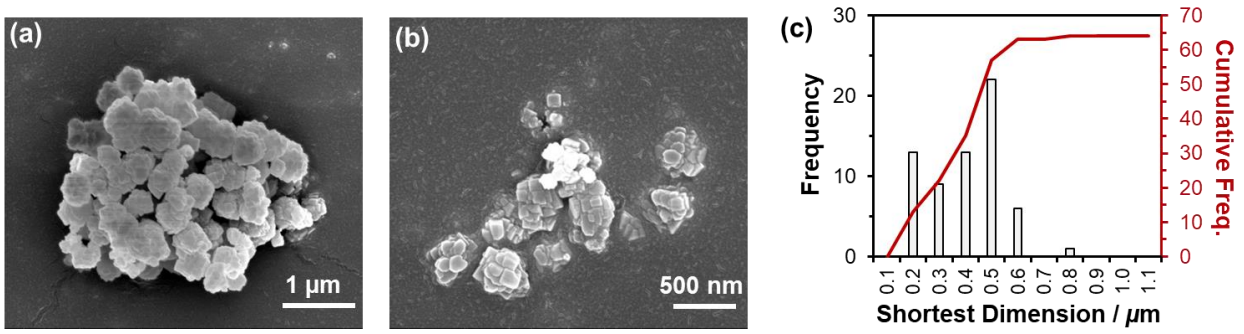

Fig. S38. (a-b) SEM images and (c) crystallite size distribution of MFI-TPA-4

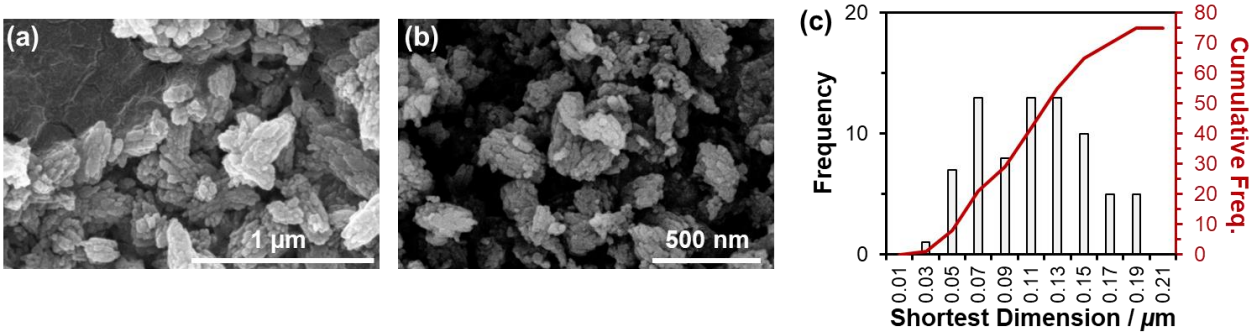

Fig. S39. (a-b) SEM images and (c) crystallite size distribution of MFI-TPA-C666

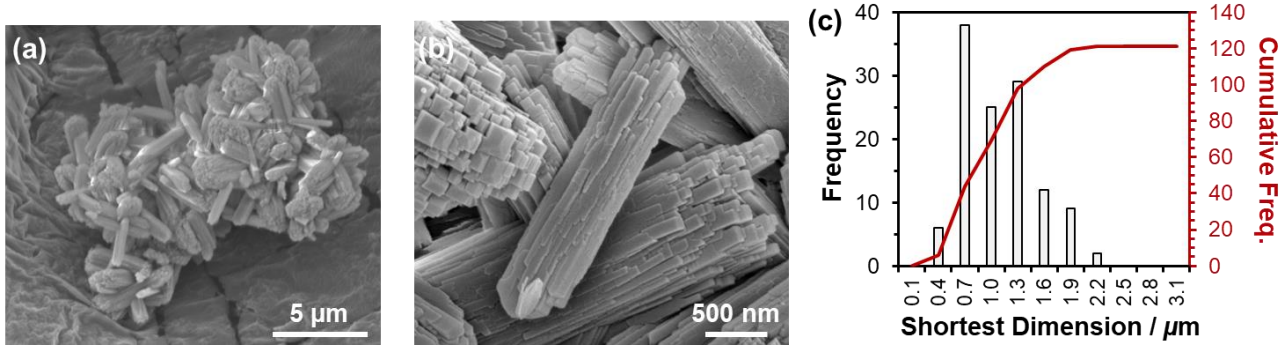

Fig. S40. (a-b) SEM images and (c) crystallite size distribution of MFI-EDA-1

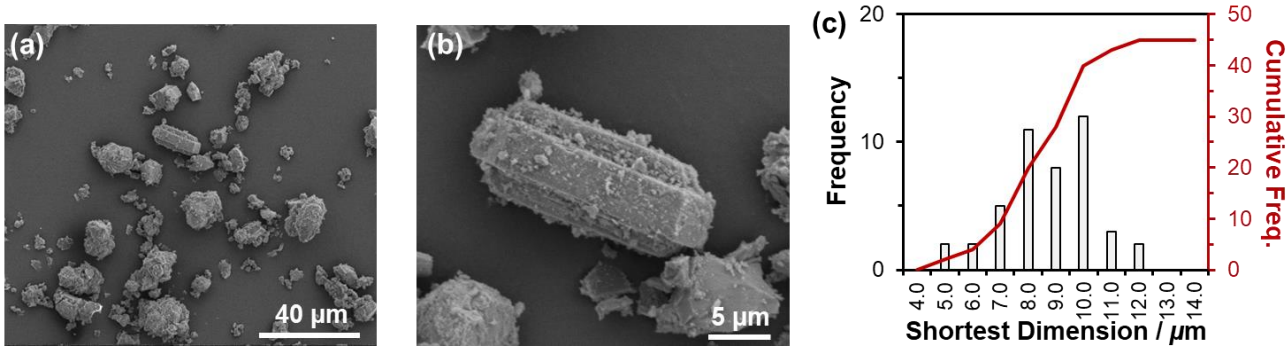

Fig. S41. (a-b) SEM images and (c) crystallite size distribution of MFI-EDA-2

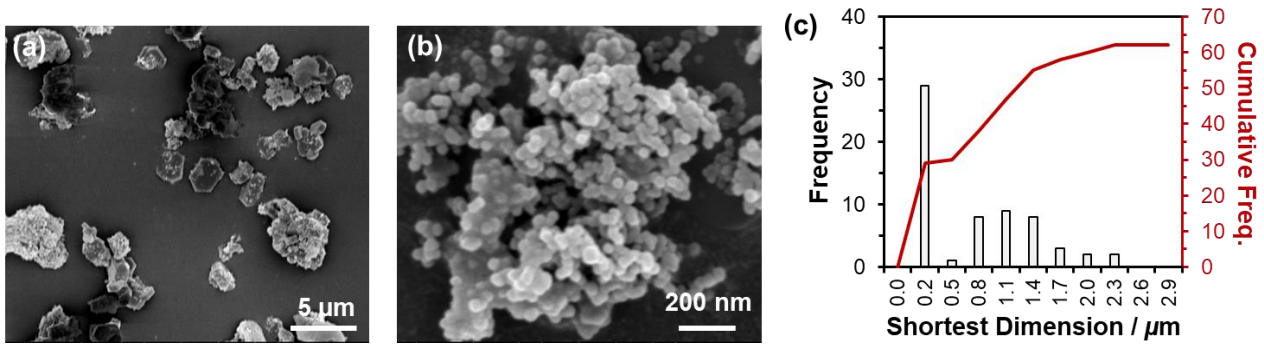

Fig. S42. (a-b) SEM images and (c) crystallite size distribution of MFI-EDA-3

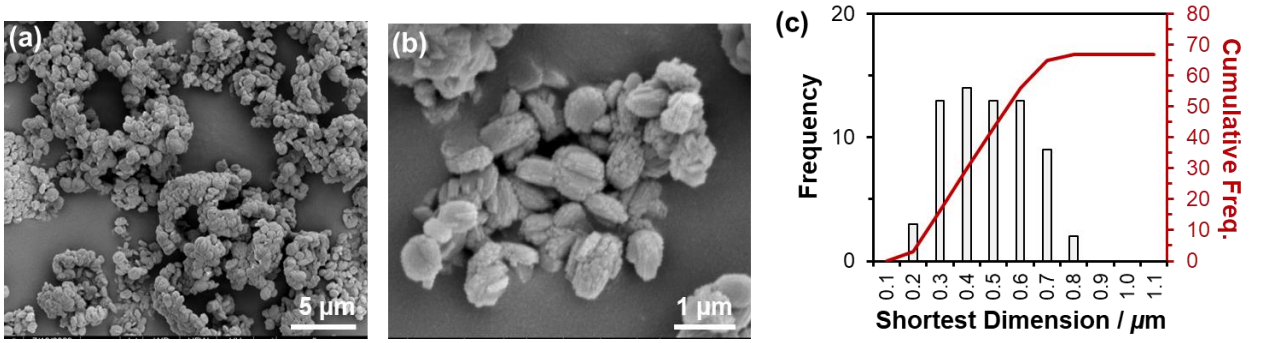

Fig. S43. (a-b) SEM images and (c) crystallite size distribution of MFI-EDA-4

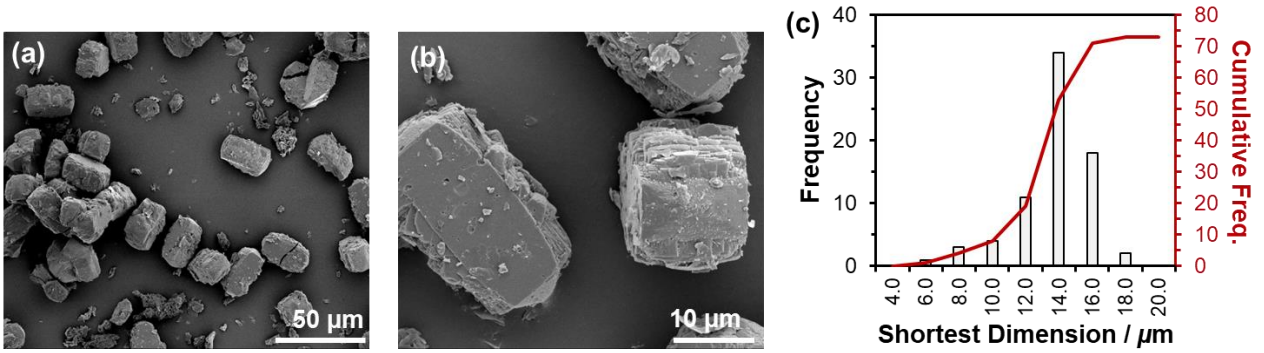

Fig. S44. (a-b) SEM images and (c) crystallite size distribution of MFI-DABCO-1

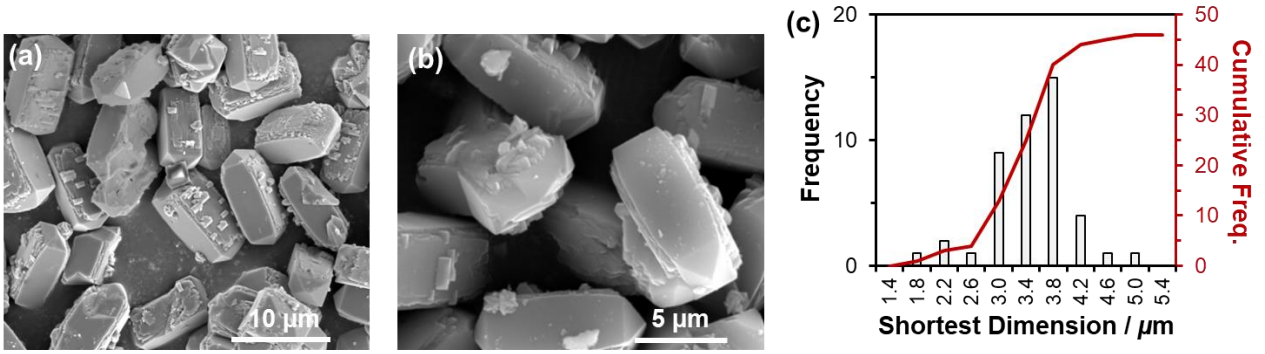

Fig. S45. (a-b) SEM images and (c) crystallite size distribution of MFI-DABCO-2

In contrast to TPA^+-only solutions that crystallize MFI at a wide range of synthesis conditions, syntheses from solutions containing EDA as the sole organic SDA result in various solid products (e.g., MFI, FER, MRE)[77–82] depending on synthesis conditions. To ensure crystallization to MFI phase and incorporation of EDA, our MFI-EDA synthesis (described in Section S1.3) was designed as a "mixed template" system[83] (under Na^+-free conditions) where TPA^+ is supplied in sub-stoichiometric amounts (0.02 TPA^+ molecules per T-atom) with excess EDA (0.29 EDA molecules per T-atom). Through thermogravimetric analysis (TGA) and carbon hydrogen (CHN) analysis (described in Section S2.6, SI), the as-synthesized MFI-EDA samples were found to occlude 1.5–2.0 TPA^+ and 2.4–5.0 EDA molecules per unit cell (96 T-atoms) while the as-synthesized MFI-TPA samples occlude 3.6–4.0 TPA^+ per unit cell (Table S9, SI); the latter reflects synthesis compositions (≥0.04 TPA^+ molecules per T-atom) required to fill up each of the four MFI intersections (per unit cell) with one TPA^+ molecule.

The use of DABCO and Na^+ (MA-free) during unseeded synthesis has been reported to result in MFI, MOR or MTW depending on the synthesis solution composition[78,79]. On the other hand, the use of DABCO and MA under Na^+ free conditions during seeded synthesis (2 wt% BEA/SiO_2) has been reported to result in BEA or MTW depending on the synthesis conditions[84]. Thus, our primary goal in this work was to first ensure that phase-pure MFI was formed (in the presence of DABCO), to probe the possible influences of DABCO on altering Al siting preferences. We show using TGA and CHN analysis (Table S9, SI) that DABCO and MA are co-occluded in the as-synthesized MFI and further show using ^{13}C CP SS MAS NMR (Section S5.22) that both DABCO and MA remain intact during crystallization (Figure S81, SI).

Table S9. Summary of organic and inorganic SDA content of as-synthesized MFI zeolites

		SDA content per unit cell[b] / molecules (unit cell)$^{-1}$				
Sample	C/N[a]	TPA	EDA	DABCO	MA	Na^+
MFI-TPA-1	n.m.	3.8	-	-	-	-
MFI-TPA-2	11.0	4.0	-	-	-	-
MFI-TPA-3	n.m.	3.6	-	-	-	2.4
MFI-TPA-4	10.9	3.9	-	-	-	-
MFI-TPA-C666	n.m.	-	-	-	-	1.0
MFI-EDA-1	2.3	1.5	5.0	-	-	-
MFI-EDA-2	4.2	2.0	2.4	-	-	-
MFI-EDA-3	3.9	1.7	2.4	-	-	-
MFI-EDA-4	n.m.	n.m.	n.m.	-	-	-
MFI-DABCO-1	2.7	-	-	3.7	1.1	1.1
MFI-DABCO-2	2.8	-	-	4.5	0.9	0.3

[a]Determined by CHN elemental analysis. Uncertainties are ±10%.

[b]Calculated from total organic weight loss using TGA (for TPA^+ only synthesis) and C/N using CHN analysis (for EDA/TPA^+ and DABCO/MeN synthesis). Uncertainties are ±10%.

"-" indicates that the organic or inorganic SDA was not included in the synthesis solution.

Table S10. Summary of characterization and properties of aluminosilicates in this study

Sample	Source	Pore limiting diameter[a] / nm	Largest cavity diameter[a] / nm	Pore environment[a]	Si/Al_{tot}[c]	V_{micro}[d] / $cm^3\ g^{-1}$	H^+/Al_{tot}[e]
MFI-*X*-*Y*	Zeolyst, Purdue	0.55	0.67	10 MR 0.51×0.55 nm (sinusoidal), 0.53×0.56 nm (straight) 0.67 nm (intersections)	42–59	0.12–017	0.7–1.0
BEA-1	Purdue[85]	0.67	0.67	12 MR 0.76 x 0.64 nm	93	0.23	0.84
BEA-2	Zeolyst (CP814E)	0.67	0.67	12 MR 0.76 x 0.64 nm	13	0.27	0.65
TON	ACS Materials (MSZ22H12)	0.55	0.55	10 MR 4.6 x 5.7 nm	43	0.046	0.77
MCM-41	Sigma-Aldrich (643653)	3.0[b]	3.0[b]	Mesopores ~3.0 nm	17	-	0.35

[a]Pore diameter and environments from IZA Database of Zeolite Structures [6] and Zeomics [86]. Uncertainties in pore diameter is ±0.2 nm.
[b]Supplier provided pore size (BJH).
[c]Determined from ICP-OES (Si, Al) or AAS (Al). Uncertainties are ±10%.
[d]Determined from N_2 adsorption isotherms at 77 K by linear extrapolation of the volumetric uptake of liquid.N_2 at 0.05–0.35 P/P_0 to zero pressure. Uncertainties are ±0.01 $cm^3\ g^{-1}$.
[e]Determined from liquid-phase NH_4^+ ion exchange followed by NH_3 TPD.

S5.14. Gas-phase DFT calculations on xylene isomers and carbocations

Gas phase DFT calculations provide information on the inherent relative stability of reaction products and transition states while decoupling these from sterics effects within the zeolite framework. Table S11 summarizes gas phase calculations for toluene methylation transition state formation using three cationic methylating agents ($CH_3OH_2^+$, $CH_3OH(CH_3)^+$, and $CH_3O(CH_3)_2^+$). Gas phase barriers are consistently similar for *o*X and *p*X isomers irrespective of the methylating gas cation, while being consistently higher for meta-xylene isomer formation. These trends in gas-phase barriers are consistent with those expected from the relative carbocations stability corresponding to each xylene regioisomer, which were found to be 5.4 kJ mol^{-1} for *o*X and as high as 18.4 kJ mol^{-1} for *m*X relative to *p*X isomer. The relative stability of the regioisomer molecules, however, differs from this trend, as *m*X was found to be the most stable isomer. These trends in relative molecule stability are consistent with the equilibrium product distribution (~50% *m*-X, ~25% *p*-X, ~25% *o*-X; 573–673 K). On the other hand, trends in carbocation stability are consistent with the established selectivity trends dictated by electrophilic substitution patterns (~60% *o*X, ~10% *m*X, ~30% *p*X) during toluene methylation on acid catalysts.

Table S11. Gas-phase electronic toluene methylation barriers[a]

	Rel. Stability *kJ mol^{-1}*	Gas-phase barriers [b] *kJ mol^{-1}*			Rel. Stability *kJ mol^{-1}*
Xylene	Molecule	$CH_3OH_2^+$	$CH_3OH(CH_3)^+$	$CH_3O(CH_3)_2^+$	Carbocation
ortho	3.9	3.9	24.0	40.6	5.4
meta	0.0	6.3	30.2	47.8	18.4
para	0.6	4.0	24.5	43.4	0.0

[a] Gas phase calculations were done on a 15 x 15 x 15 Å vacuum box

[b] Gas phase methylating cation

S5.15. Detailed reaction coordinate diagram for toluene methylation

Toluene methylation can occur via two distinct pathways, namely, the concerted and sequential pathway. The sequential pathway is initiated by surface methylation with methanol or DME to form a surface bound methyl (Z–CH_3), followed by the toluene methylation step. In the concerted pathway, however, toluene is directly methylated with methanol or DME, resulting in the concurrent formation of water or methanol, respectively. Previous DFT calculations on arene methylation reactions found the surface methylation step to be rate determining in the sequential pathway for toluene methylation[28]. The surface methylation step, however, was found to occur with barriers that are 20 kJ mol^{-1} and 30 kJ mol^{-1} lower than the corresponding concerted pathway with methanol and DME respectively. All reactant, product, and transition states reported in this work thus correspond to the toluene methylation sequential mechanism. The transition state structure for the toluene methylation step in the sequential mechanism (i.e., the selectivity determining step toward xylenes) was found to resemble a SN_2 transition state with a planar CH_3 carbocation between toluene and the framework O-atom.

Figure S46 shows two reaction coordinate diagrams of the sequential reaction mechanism for toluene methylation reaction with DME as the methylating agent, as occurring at T12 and T4 of MFI. The formation DME derived Z–CH_3 is shown in black and occurs with similar activation barriers of 89 and 87 kJ mol^{-1} relative to bare Z–H at T12 and T4 of MFI, respectively. Once Z–CH_3 is formed, toluene co-adsorbs nearby, forming the precursor state for toluene methylation transition state formation. This co-adsorbed toluene near Z–CH_3 state is more negative than its corresponding Z–H state for the both T-sites, but it is less stable in T4 than in T12 by 22 kJ mol^{-1}. This suggests that colocation of toluene near Z–CH_3 is more favorable in MFI channel intersections than in more confined T4 at sinusoidal channel. Accordingly, the corresponding activation barriers for toluene methylation are consistently lower at T12 for all xylene isomers. The differences between *p*X and *o*X activation barriers ($\Delta\Delta G_{pX-oX}$), however, becomes more negative at T4 (3 kJ mol^{-1} T12, –22 kJ mol^{-1} T4) suggesting a higher selectivity toward *p*X at T4. This, in turn, suggests that tighter confinements are more selective toward *p*X, even when all barriers systematically increase, because the extent of this penalty is less detrimental to *p*X transition state formation among all xylene regioisomers.

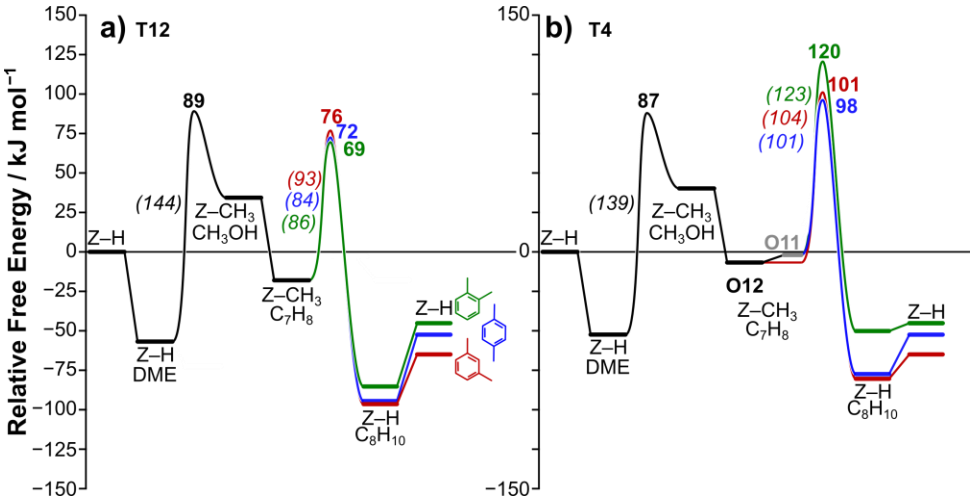

Fig. S46. Reaction coordinate diagram for toluene methylation with DME at (a) T12 and (b) T4 sites of MFI framework. Effective (**bold**) and intrinsic (*italics*) barriers for toluene methylation are shown for *o*-X (green), *m*-X (red), and *p*-X (blue)

S5.16. Analysis of DFT-calculated activation enthalpies for toluene methylation to xylene isomers

Gibbs free energies are used as descriptors to address the experimentally relevant selectivity toward transition state formation during toluene methylation reaction. However, free energies account for both enthalpic and entropic effects during reaction. Decoupling free energies into their corresponding enthalpic and entropic contributions is informative of the role of these contributions and thus of the governing parameters for transition state formation and their selectivity. Figure S47 shows the corresponding enthalpy methylation (ΔH_{act}) and relative ($\Delta\Delta H_{pX-oX}$) barriers for toluene methylation transition state formation. Values for $\Delta\Delta H_{pX-oX}$ strongly correlate ($R^2 = 0.97$) with their corresponding $\Delta\Delta G_{pX-oX}$ values and the slope for such correlation is close to unity (0.82). This suggest that the observed trends in DFT-predicted rates and selectivities as a function of T-O site location ($\Delta\Delta G_{pX-oX}$) are likely driven by—and consistent with—activation enthalpy trends. This, in turn, suggests that the xylene selectivity in a given T-O pair is governed by the relative stability between transition states and not due to any differences in entropy losses upon transition state formation.

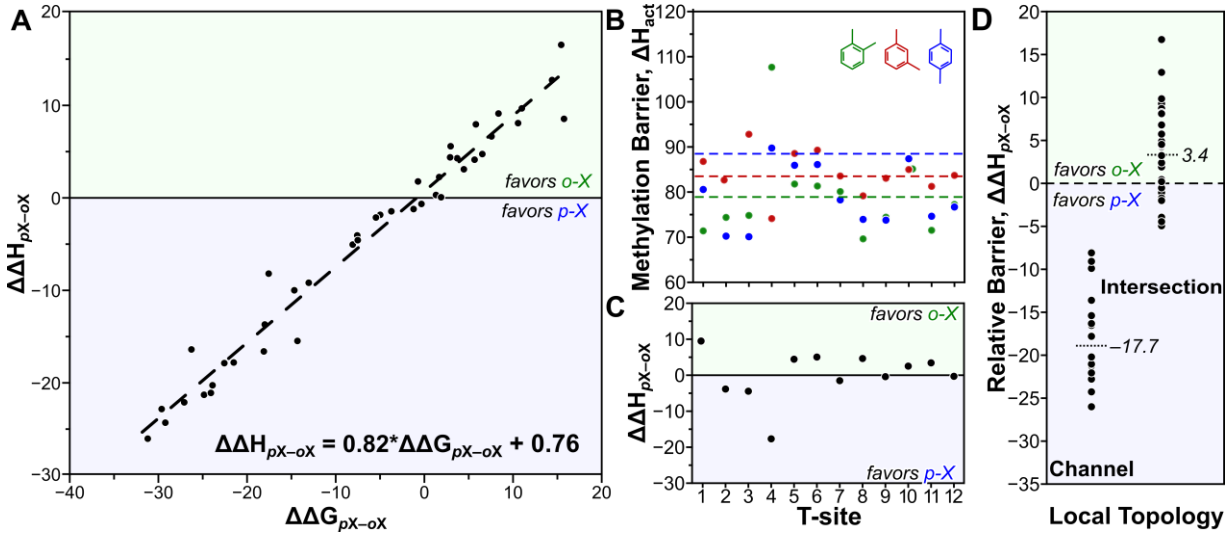

Fig. S47. Correlation ($R^2 = 0.97$) of $\Delta\Delta H_{pX\text{-}oX}$ against $\Delta\Delta G_{pX\text{-}oX}$ for all T-O pairs explored in MFI. Panels B–D are the corresponding $\Delta\Delta H_{pX\text{-}oX}$ values for $\Delta\Delta G_{pX\text{-}oX}$ shown in Figure 3C and 3D from the main text.

S5.17. T-site maps for MFI framework and DFT transition state sampling

Toluene methylation transition states were systematically explored across all 12 crystallographically unique T-sites in the MFI zeolite model, shown in Figure S48 Each T-site is tetrahedrally coordinated with 4 O-atoms, resulting in 48 crystallographically distinct T-O pairs that could potentially mediate toluene methylation transition states. Oxygen atoms O4, O20, and O24 were excluded from investigation because they were inaccessible to intermediates larger than CH_3OH. Figure S49 shows three MFI framework maps featuring the location of all the converged transition state structures for xylene formation, colored by the T-site that mediated transition state formation. The total number of converged transition state structures amounts to 19138, reflecting the exhaustive DFT sampling across the MFI framework.

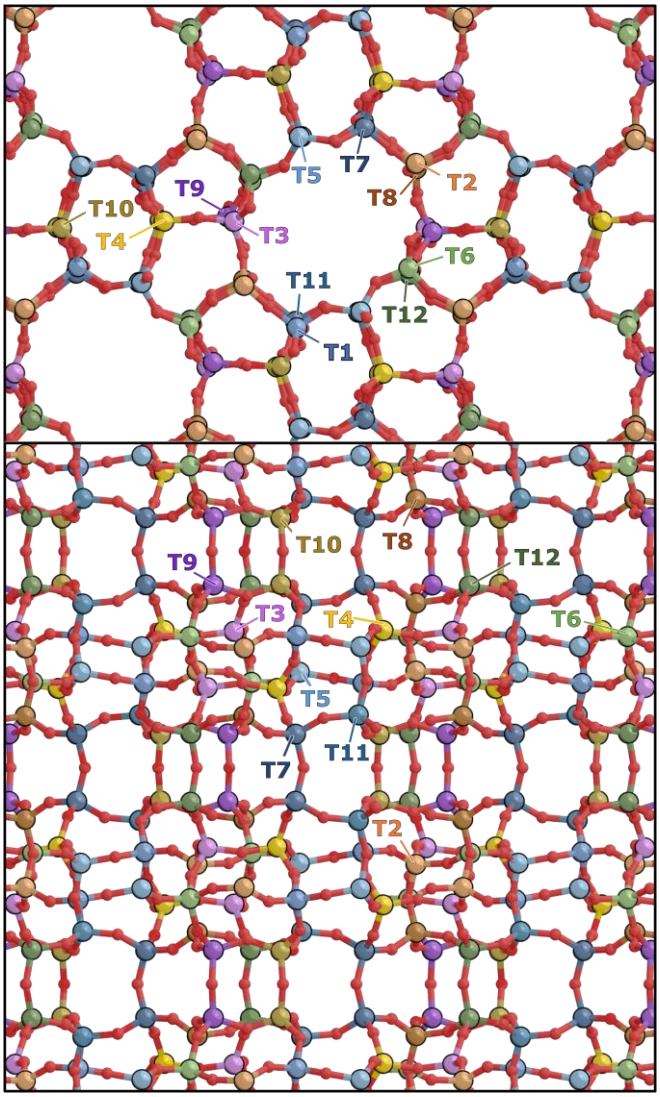

Fig. S48. MFI framework view along the 010 (top) and 001 (bottom) views with T-sites identified by color.

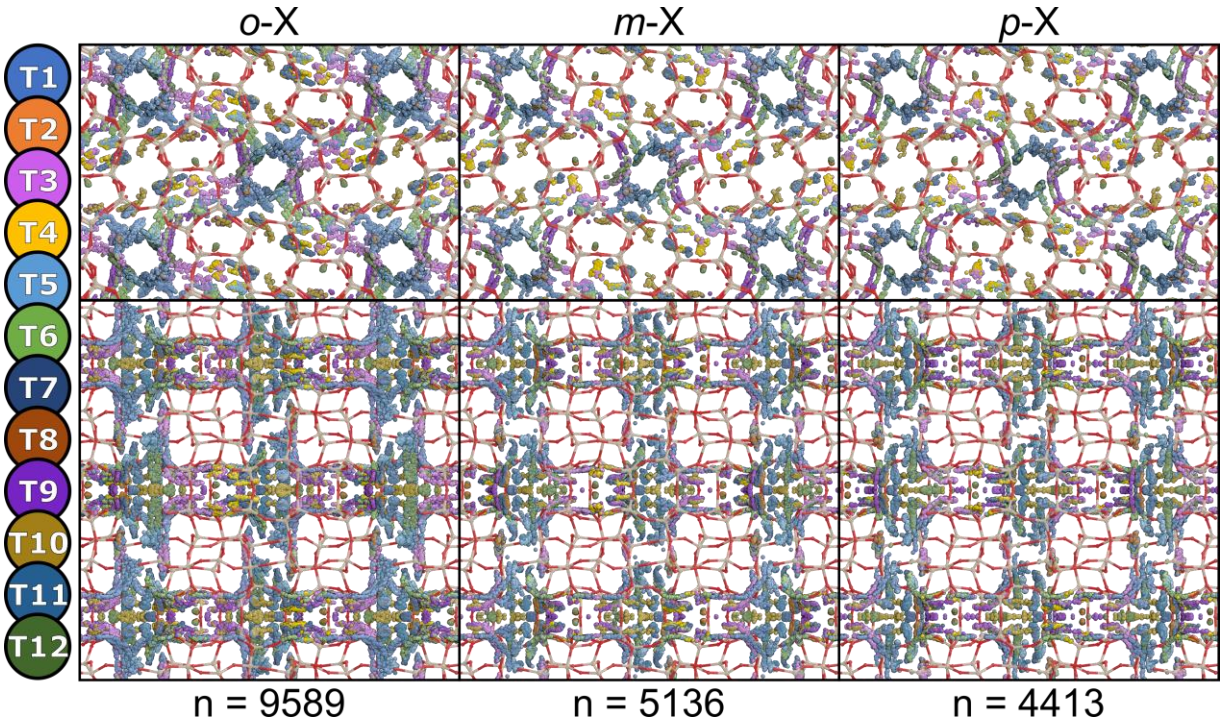

Fig. S49. Locations of CH_3^+ species for transition states within MFI along the 010 (top) and 001 (bottom) views with color representing the T-site that mediates transition state formation for *o*X, *m*X, and *p*X, respectively. The total number of converged transition states (n) is also given for each isomer. Total overall: 19,138 converged toluene methylation transition states.

S5.18. Transition state structures across all 12 T-sites in MFI

Figures S50–S61 show the structures of the best toluene methylation transition states for the xylene regioisomers at each T-site of MFI, along the straight and sinusoidal channel views of MFI. Effective barriers are consistently higher than their intrinsic counterparts, reflecting that adsorbed DME* is more thermodynamically favored than toluene coadsorbed near a surface methyl, Z–CH_3. Transition state structures reflect an S_N2-like transition states which features a planar CH_3^+ carbocation between the ring-C atom of toluene and the O-atom from zeolite framework. As such, all transition states presented here are geometrically similar, suggesting that—since T-sites have similar acid strengths—differences in their relative stabilities must result from differences in confinement effects. For Figures S50–S61, the specific O-atom associated with the reaction, the intrinsic barrier (relative to toluene coadsorbed near Z–CH_3) and the effective barrier (relative to DME bound to a surface proton, Z–H) are shown.

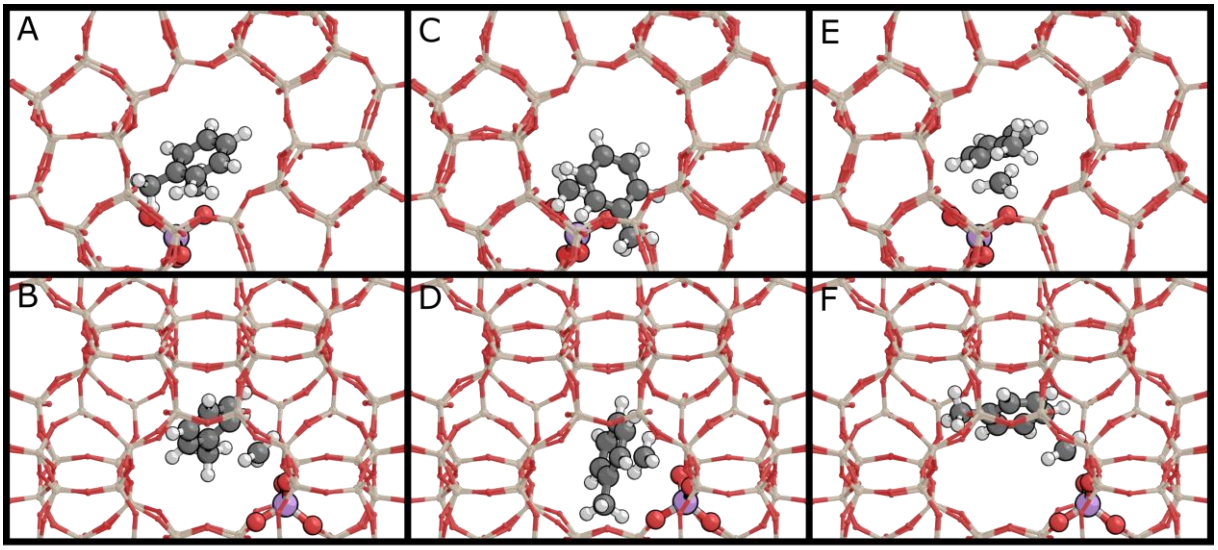

T1	o-xylene	m-xylene	p-xylene
O-atom	O1	O2	O1
$\Delta G_{act,int}$	*79*	*94*	*87*
$\Delta G_{act,eff}$	**113**	**129**	**122**

Fig. S50. Transition state structures for toluene methylation at T1 viewed along the (010) (top) and 100 (bottom) axes. Activation free energies (ΔG_{act},kJ mol^{-1}) are reported at 403 K.

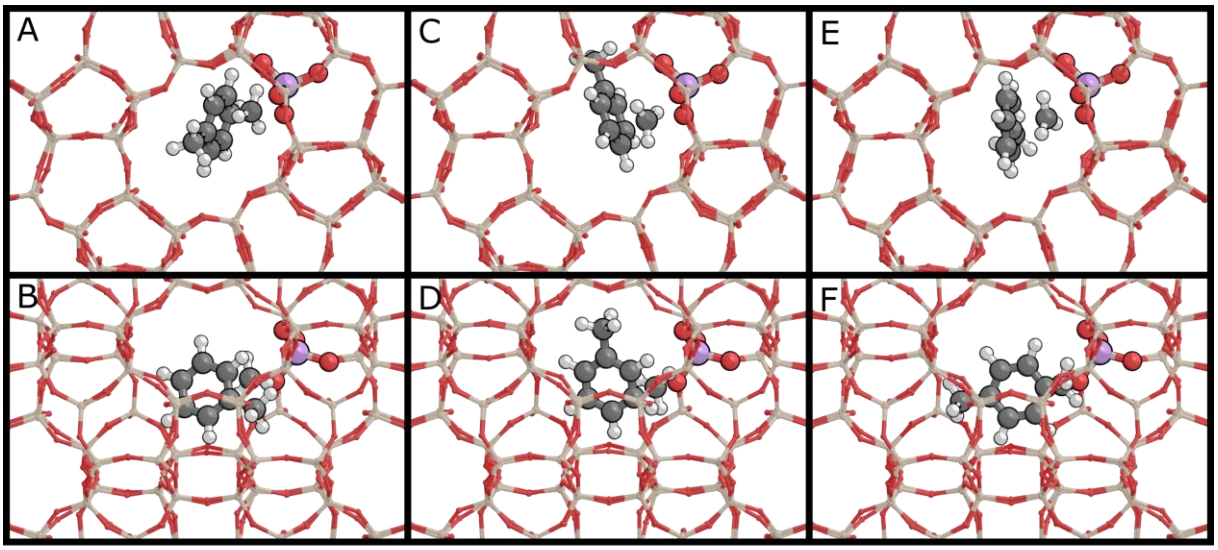

T2	o-xylene	m-xylene	p-xylene
O-atom	O5	O5	O5
$\Delta G_{act,int}$	*88*	*92*	*80*
$\Delta G_{act,eff}$	**129**	**133**	**121**

Fig. S51. Transition state structures for toluene methylation at T2 viewed along the (010) (top) and 100 (bottom) axes. Activation free energies (ΔG_{act},kJ mol^{-1}) are reported at 403 K.

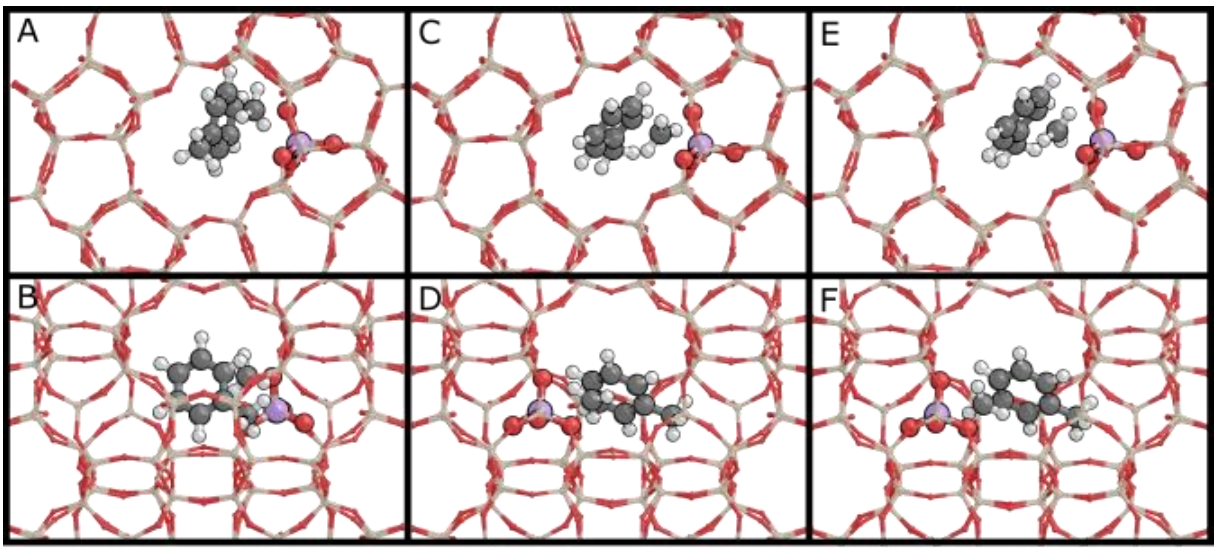

T3	o-xylene	m-xylene	p-xylene
O-atom	O5	O8	O8
$\Delta G_{act,int}$	*86*	*86*	*81*
$\Delta G_{act,eff}$	**133**	**133**	**128**

Fig. S52. Transition state structures for toluene methylation at T3 viewed along the 010 (top) and 100 (bottom) axes. Activation free energies (ΔG_{act},kJ mol^{-1}) are reported at 403 K.

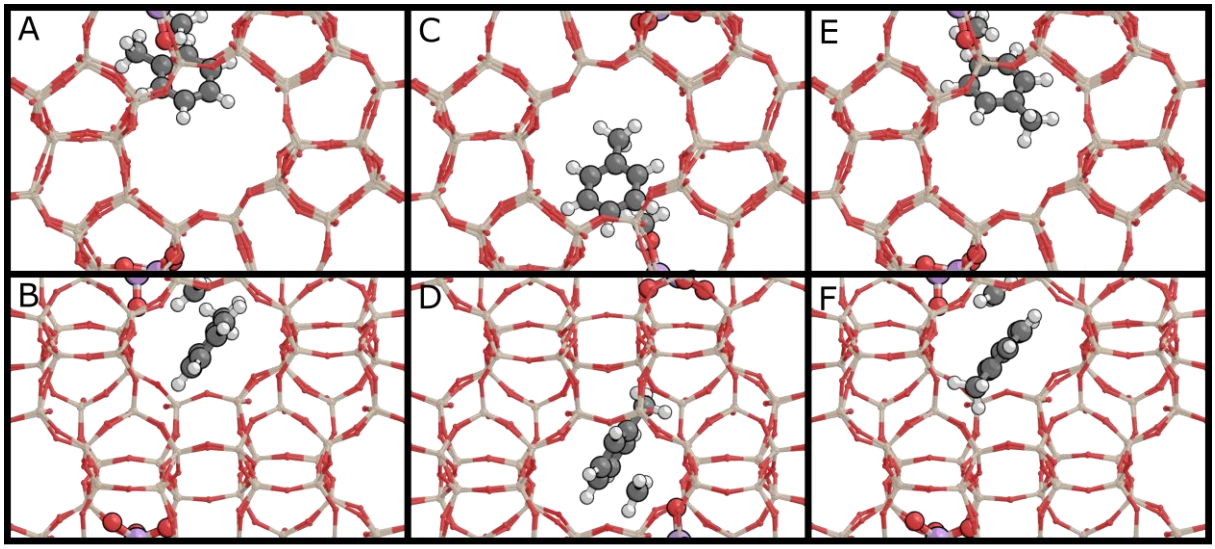

T4	o-xylene	m-xylene	p-xylene
O-atom	O11	O12	O11
$\Delta G_{act,int}$	*123*	*104*	*101*
$\Delta G_{act,eff}$	**172**	**152**	**149**

Fig. S53. Transition state structures for toluene methylation at T4 viewed along the 010 (top) and 100 (bottom) axes. Activation free energies (ΔG_{act},kJ mol^{-1}) are reported at 403 K.

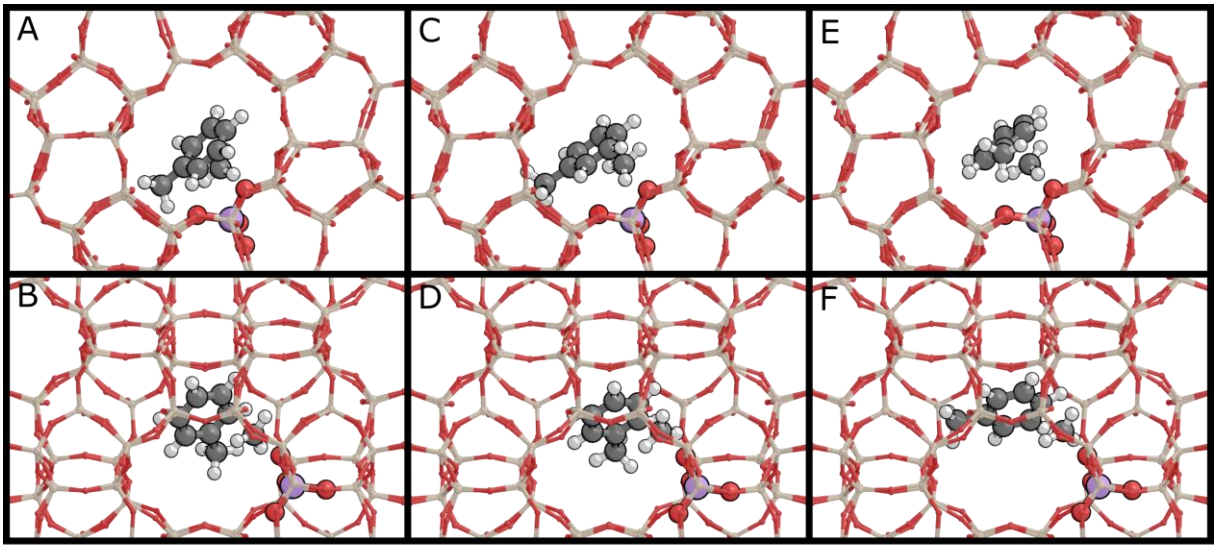

T5	o-xylene	m-xylene	p-xylene
O-atom	O13	O13	O13
$\Delta G_{act,int}$	*90*	*98*	*96*
$\Delta G_{act,eff}$	**124**	**132**	**130**

Fig. S54. Transition state structures for toluene methylation at T5 viewed along the 010 (top) and 100 (bottom) axes. Activation free energies (ΔG_{act},kJ mol^{-1}) are reported at 403 K.

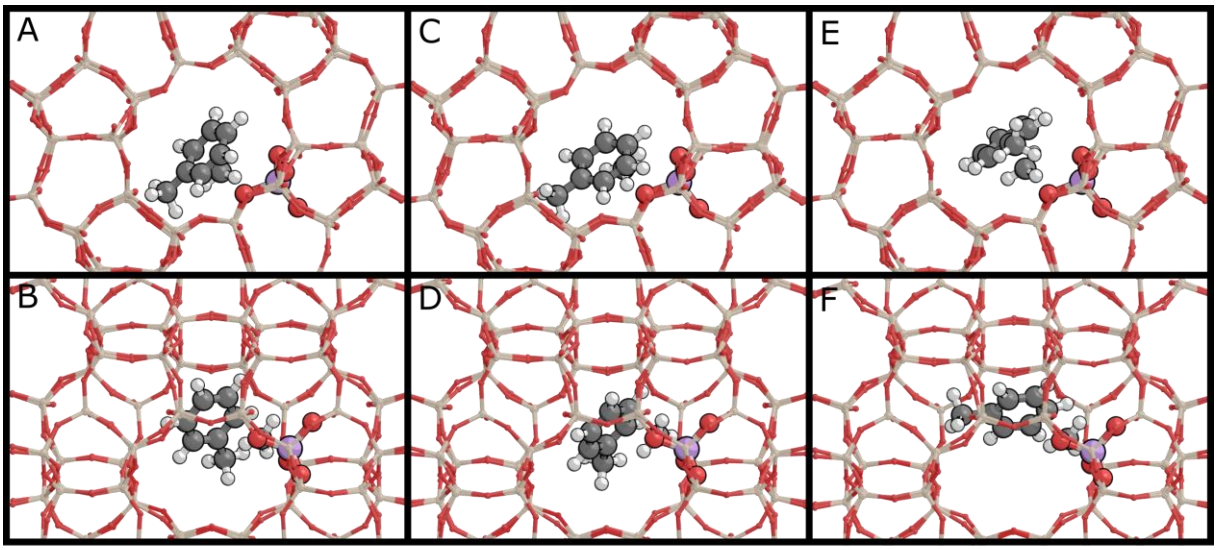

T6	o-xylene	m-xylene	p-xylene
O-atom	O13	O13	O13
$\Delta G_{act,int}$	*90*	*98*	*96*
$\Delta G_{act,eff}$	**127**	**136**	**133**

Fig. S55. Transition state structures for toluene methylation at T6 viewed along the 010 (top) and 100 (bottom) axes. Activation free energies (ΔG_{act},kJ mol^{-1}) are reported at 403 K.

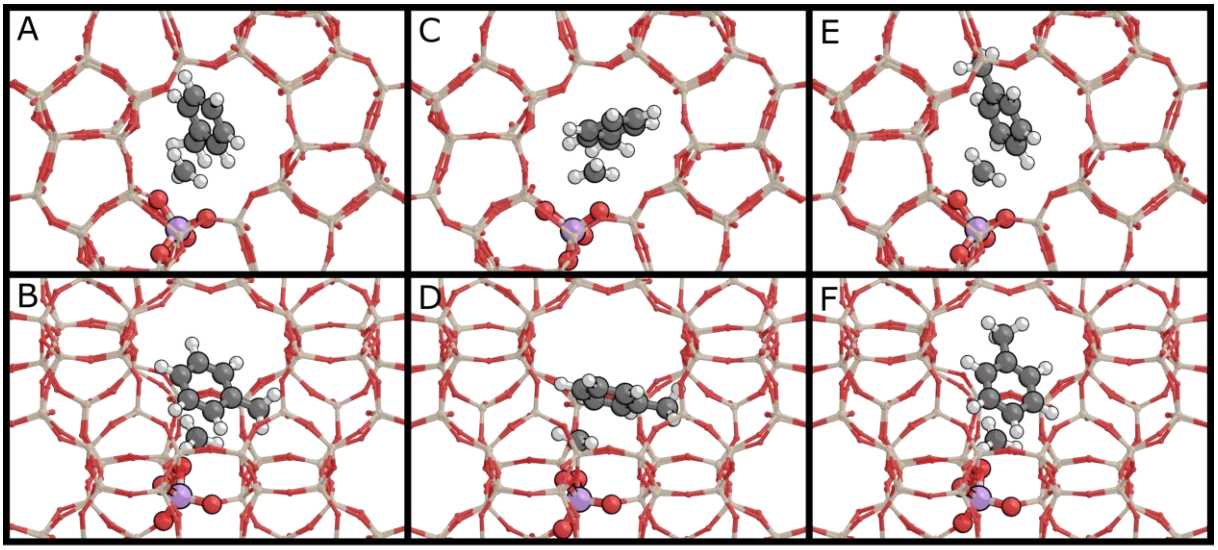

T7	o-xylene	m-xylene	p-xylene
O-atom	O3	O16	O17
$\Delta G_{act,int}$	*93*	*94*	*88*
$\Delta G_{act,eff}$	**136**	**137**	**132**

Fig. S56. Transition state structures for toluene methylation at T7 viewed along the 010 (top) and 100 (bottom) axes. Activation free energies (ΔG_{act},kJ mol^{-1}) are reported at 403 K.

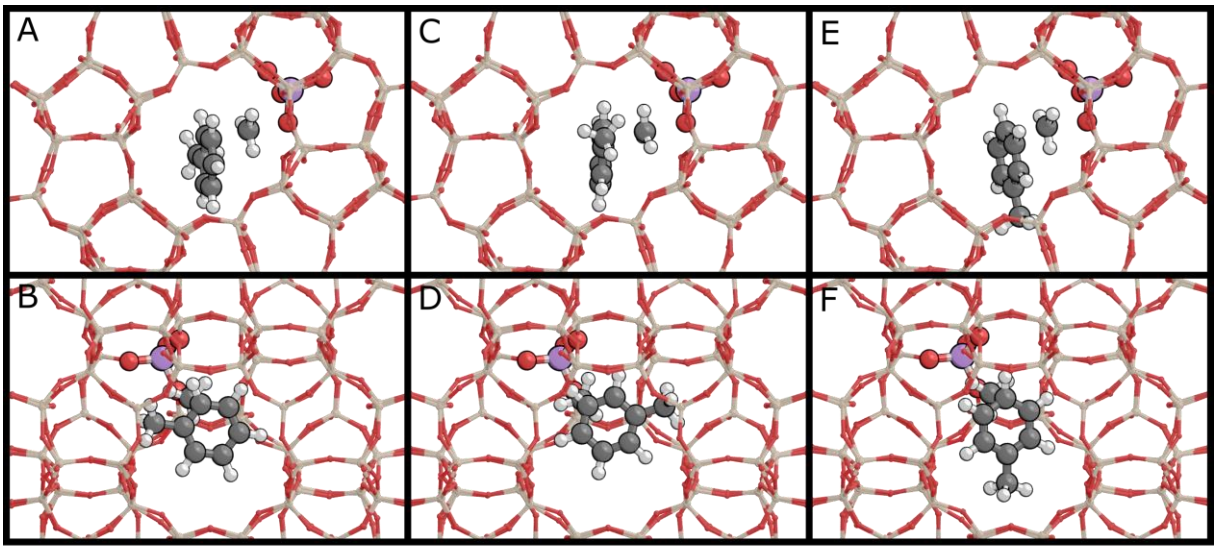

T8	o-xylene	m-xylene	p-xylene
O-atom	O3	O19	O19
$\Delta G_{act,int}$	*78*	*86*	*81*
$\Delta G_{act,eff}$	**113**	**122**	**117**

Fig. S57. Transition state structures for toluene methylation at T8 viewed along the 010 (top) and 100 (bottom) axes. Activation free energies (ΔG_{act},kJ mol^{-1}) are reported at 403 K.

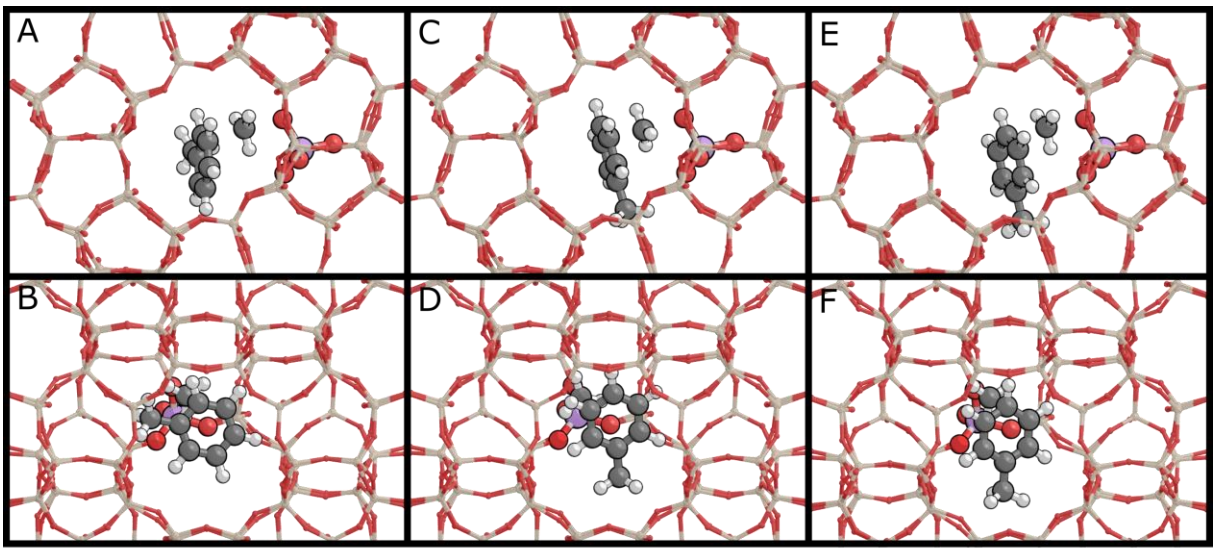

T9	o-xylene	m-xylene	p-xylene
O-atom	O19	O19	O19
$\Delta G_{act,int}$	*86*	*96*	*88*
$\Delta G_{act,eff}$	**126**	**135**	**127**

Fig. S58. Transition state structures for toluene methylation at T9 viewed along the 010 (top) and 100 (bottom) axes. Activation free energies (ΔG_{act},kJ mol^{-1}) are reported at 403 K.

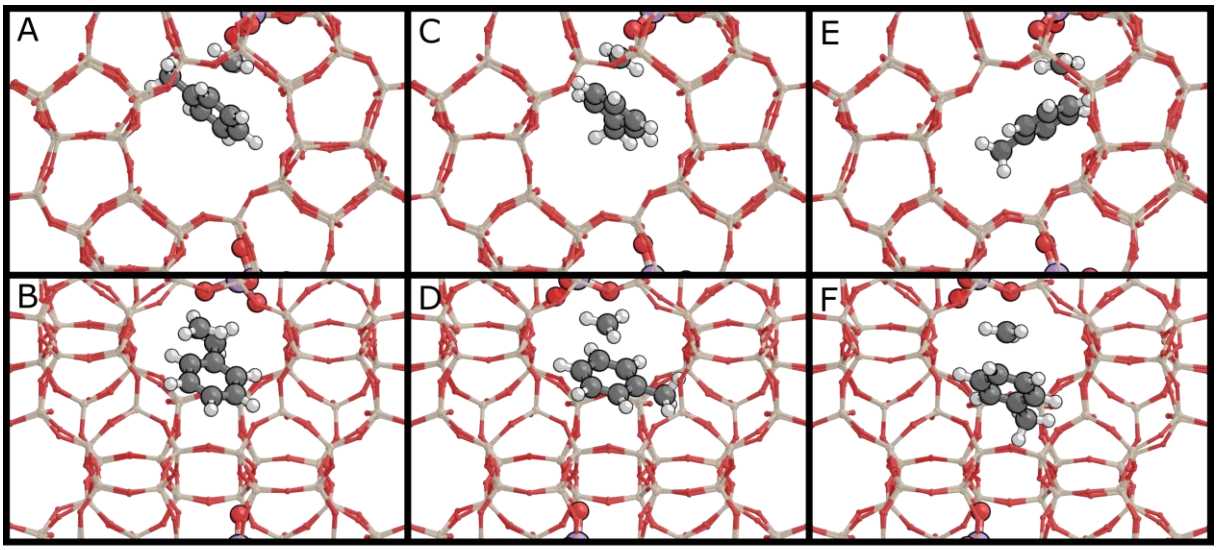

T10	o-xylene	m-xylene	p-xylene
O-atom	O23	O23	O23
$\Delta G_{act,int}$	*94*	*94*	*95*
$\Delta G_{act,eff}$	**132**	**132**	**133**

Fig. S59. Transition state structures for toluene methylation at T10 viewed along the 010 (top) and 100 (bottom) axes. Activation free energies (ΔG_{act},kJ mol^{-1}) are reported at 403 K.

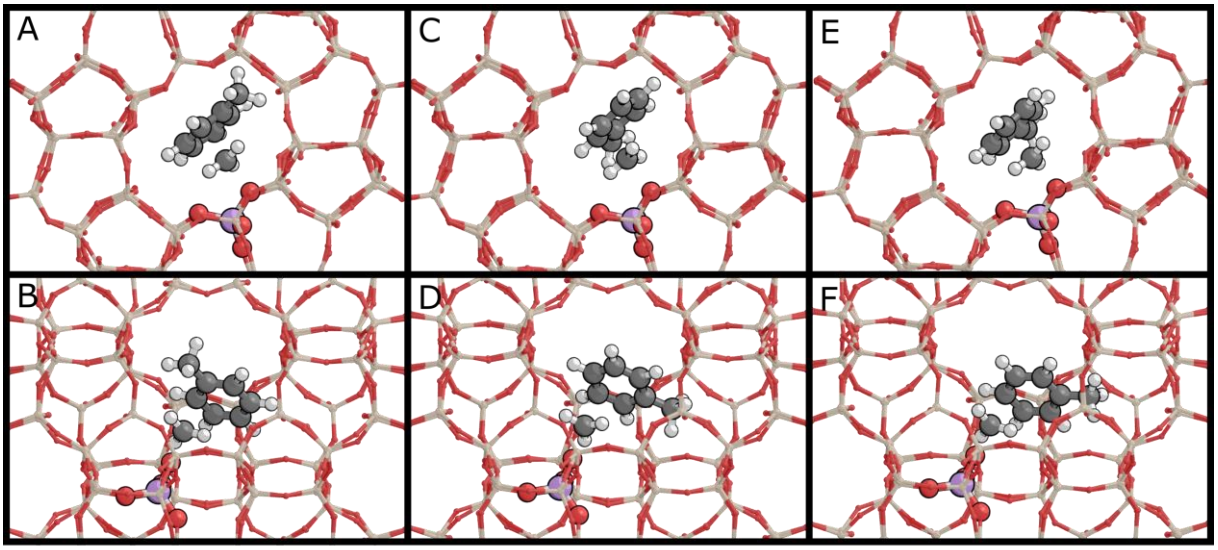

T11	o-xylene	m-xylene	p-xylene
O-atom	O25	O25	O25
$\Delta G_{act,int}$	*80*	*88*	*84*
$\Delta G_{act,eff}$	**118**	**127**	**123**

Fig. S60. Transition state structures for toluene methylation at T11 viewed along the 010 (top) and 100 (bottom) axes. Activation free energies (ΔG_{act},kJ mol^{-1}) are reported at 403 K.

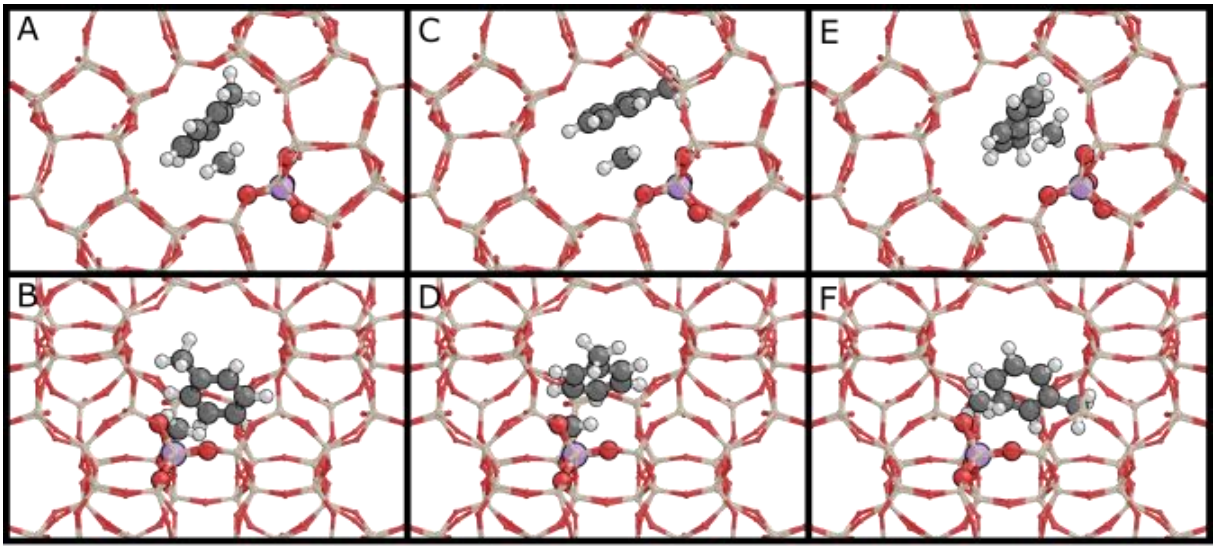

T12	o-xylene	m-xylene	p-xylene
O-atom	O3	O25	O8
$\Delta G_{act,int}$	*86*	*93*	*84*
$\Delta G_{act,eff}$	**125**	**132**	**123**

Fig. S61. Transition state structures for toluene methylation at T12 viewed along the 010 (top) and 100 (bottom) axes. Activation free energies (ΔG_{act},kJ mol^{-1}) are reported at 403 K.

S5.19. DFT calculated barriers for xylene formation across all T-O pairs in MFI

Figure S62a–c show intrinsic (relative to toluene coadsorbed with Z–CH_3) activation barriers across all unique T-O pairs in MFI zeolite for *o*X, *m*X, and *p*X formation, respectively (with the exception of those excluded because of being inaccessible for toluene methylation transition states). Intrinsic barriers are classified as "Channel" if the corresponding transition state resides within the straight or sinusoidal channels of MFI, otherwise they are classified as "Intersection" when residing in the channel intersections of MFI. Toluene methylation barriers spread on a wide and overlapping range between Channel and Intersection transition states. Their averages, however, are consistently higher for transition states occurring in the straight and sinusoidal channels (120 vs 84 kJ mol^{-1} *o*X; 102 vs 89 kJ mol^{-1} for *m*X; 97 vs 87 kJ mol^{-1} for *p*X) than in channel intersections, suggesting that toluene methylation transition states are penalized in tighter environments. The differences between the averages, however, are lower for *p*X (36 > 13 > 10 kJ mol^{-1}), suggesting that the penalty in activation barriers in toluene methylation transition states is less detrimental for *p*X among xylene regioisomers. These differences, in turn, result in channel environments being more selective toward para-xylene, as shown in Figure 3D in the main text, which shows the corresponding $\Delta\Delta G_{pX-oX}$ values for all the considered T-O pairs also classified by the environment at which the transition state occurs. Overall, this demonstrates that the environment at which the Z–CH_3 resides directly influences the relative barriers and thus selectivity among xylene regioisomers during toluene methylation, and that it does so by favoring *p*X formation transition states when occurring in tighter environments.

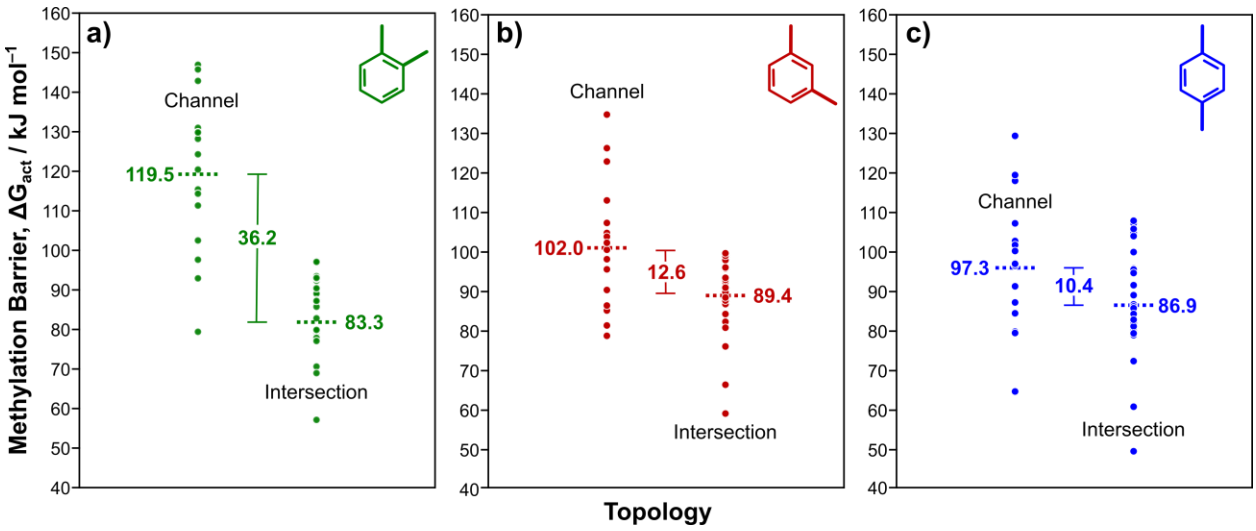

Fig. S62. Toluene methylation barriers toward a) *o*X, b) *m*X, and c) *p*X as a function of zeolite topology. Framework environment (Intersection vs. Channel) indicates the location of the transition state structure within MFI. Free energy barriers are reported at 403 K and referenced to toluene adsorbed near a surface-bound methyl (Z–CH_3) at the corresponding T-site.

S5.20. DFT calculated toluene methylation barriers across aluminosilicate with varying pore sizes

Toluene methylation transition states were systematically explored across other aluminosilicates with varying pore sizes: TON (~0.55 nm), BEA (~0.67 nm), and a 2D unconfined model representative of MCM-41 (~3.0 nm). TON and BEA were selected because their pore sizes are representative from those at MFI channels and intersections, respectively, which serves as a proxy to decouple the pore size distribution in MFI from the measured and calculated selectivity patterns. An unconfined 2D model was chosen to further decouple xylene regioisomers selectivity patterns from confinement effects. Figure S63 shows the corresponding best intrinsic activation barriers for toluene methylation transition state formation toward each xylene regioisomer across all zeolite models considered in this work. The corresponding selectivity descriptor, $\Delta\Delta G_{pX-oX}$, is also shown in Figure S63. Values for $\Delta\Delta G_{pX-oX}$, in TON are consistently below zero, suggesting a preference toward *p*X. This, in turn, is qualitatively consistent with negative $\Delta\Delta G_{pX-oX}$ values at T4 of MFI. $\Delta\Delta G_{pX-oX}$ values on BEA, however, are mostly near 0 with 7 T-sites having a slight preference toward *o*X. This is similar to values found on the majority of T-sites in MFI, suggesting that larger pores in BEA are less selective toward *p*X. This is further confirmed by the value of $\Delta\Delta G_{pX-oX}$ at 2D model, which lacking confinement shows similar barriers for *o*X and *p*X formation but high barriers for *m*X. Overall, $\Delta\Delta G_{pX-oX}$ values at TON, BEA, and 2D aluminosilicate models are consistent with the hypothesis and experimental observations that *p*X selectivity decreases when increasing pore size (0.55 nm → 0.67 nm) and remains invariant to further increasing pore size (>0.67 nm). This, in turn, may further indicate that the observed differences in selectivities on MFI samples reflect differences in aluminum siting that subsequentially influence the available environments for toluene methylation transition state formation.

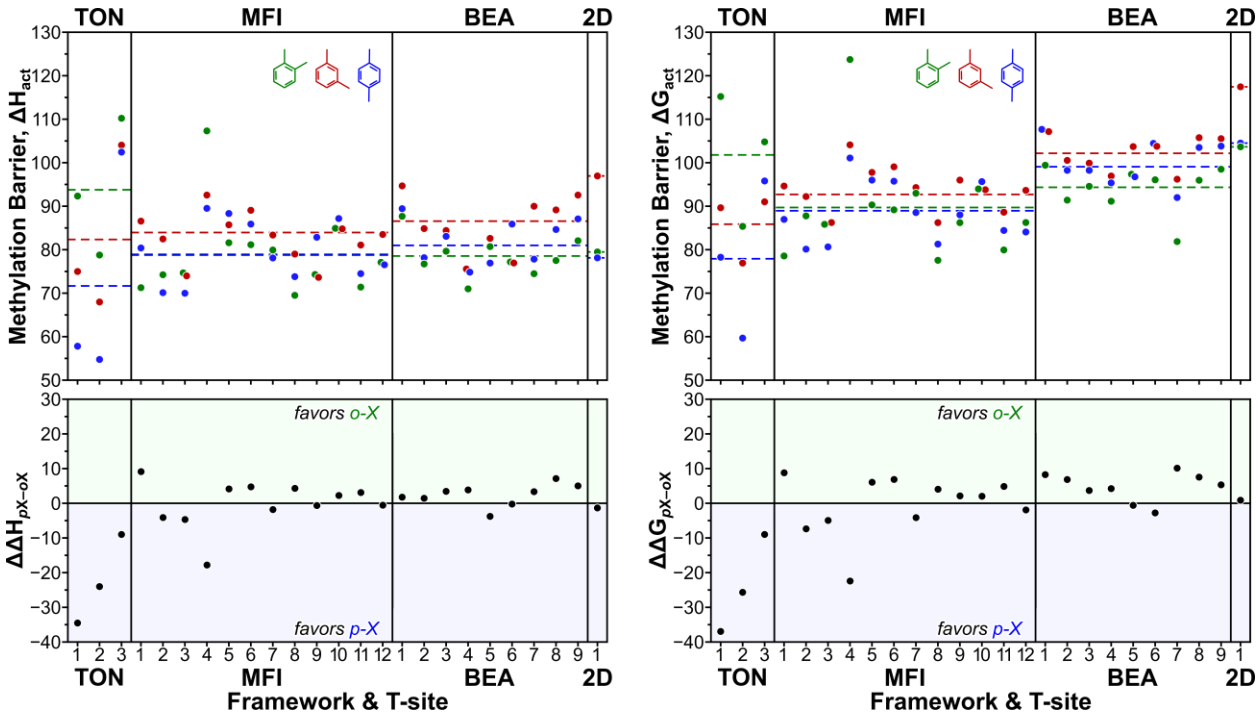

Fig. S63. Best toluene methylation barriers (ΔH_{act} and ΔG_{act}) and their corresponding relative barriers ($\Delta\Delta H_{pX-oX}$ and $\Delta\Delta G_{pX-oX}$) across all T-sites in TON, MFI, BEA, and 2D. Barriers are reported at 403 K and relative to toluene coadsorbed with Z–CH_3. Horizontal dashed lines represent average barriers across all T-sites in each aluminosilicate.

Transition state structures are shown for toluene methylation across all T-sites in TON (Figs. S64 to S66), BEA (Figs. S67 to S75) and unconfined aluminosilicate (2D) (Fig. S76).

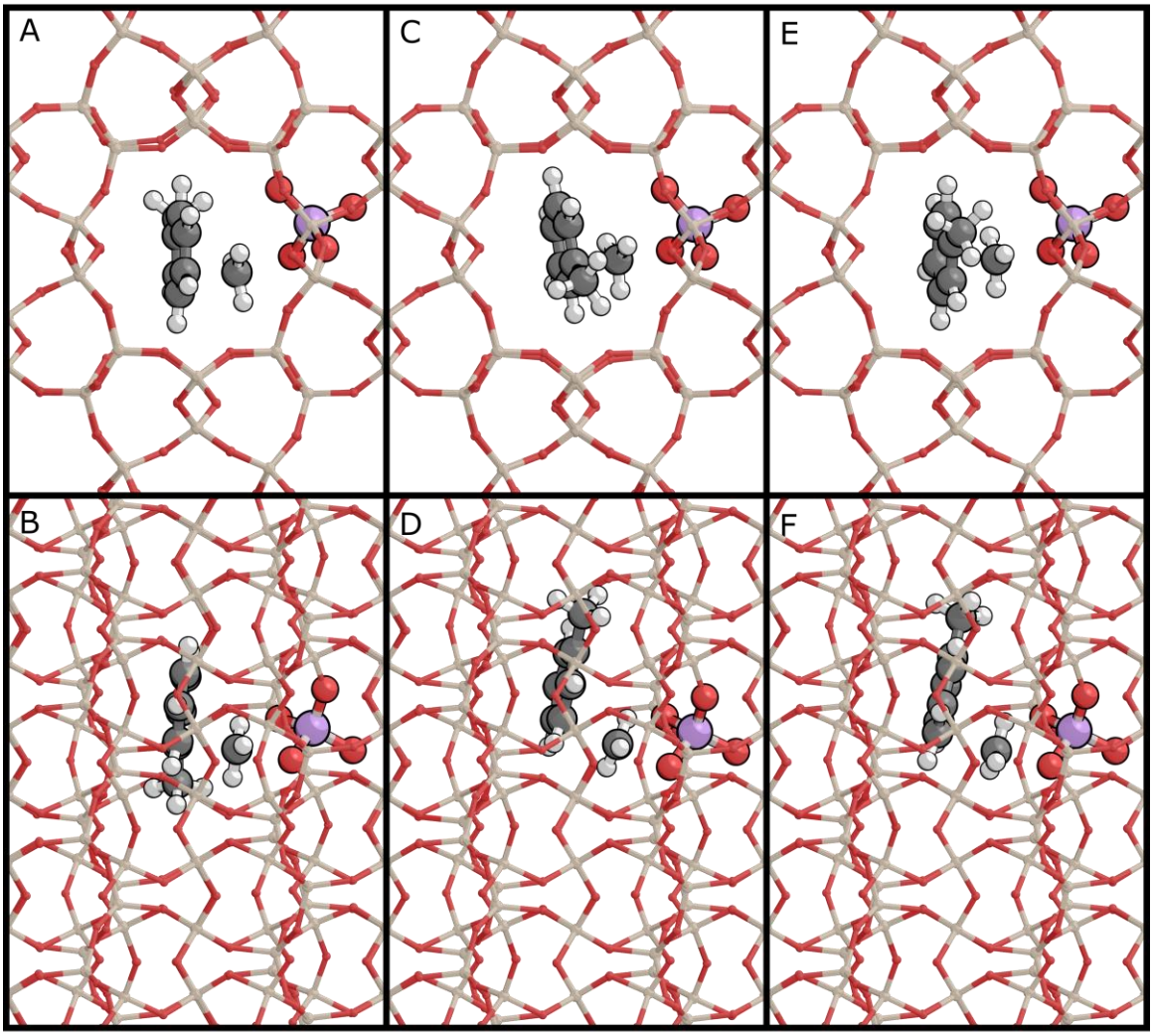

T1	o-xylene	m-xylene	p-xylene
O-atom	O1	O1	O1
$\Delta G_{act,int}$	*115*	*90*	*78*
$\Delta G_{act,eff}$	**171**	**146**	**134**

Fig. S64. Transition state structures for toluene methylation at TON-T1 viewed along the 010 (top) and 100 (bottom) axes. Activation free energies (ΔG_{act},kJ mol^{-1}) are reported at 403 K.

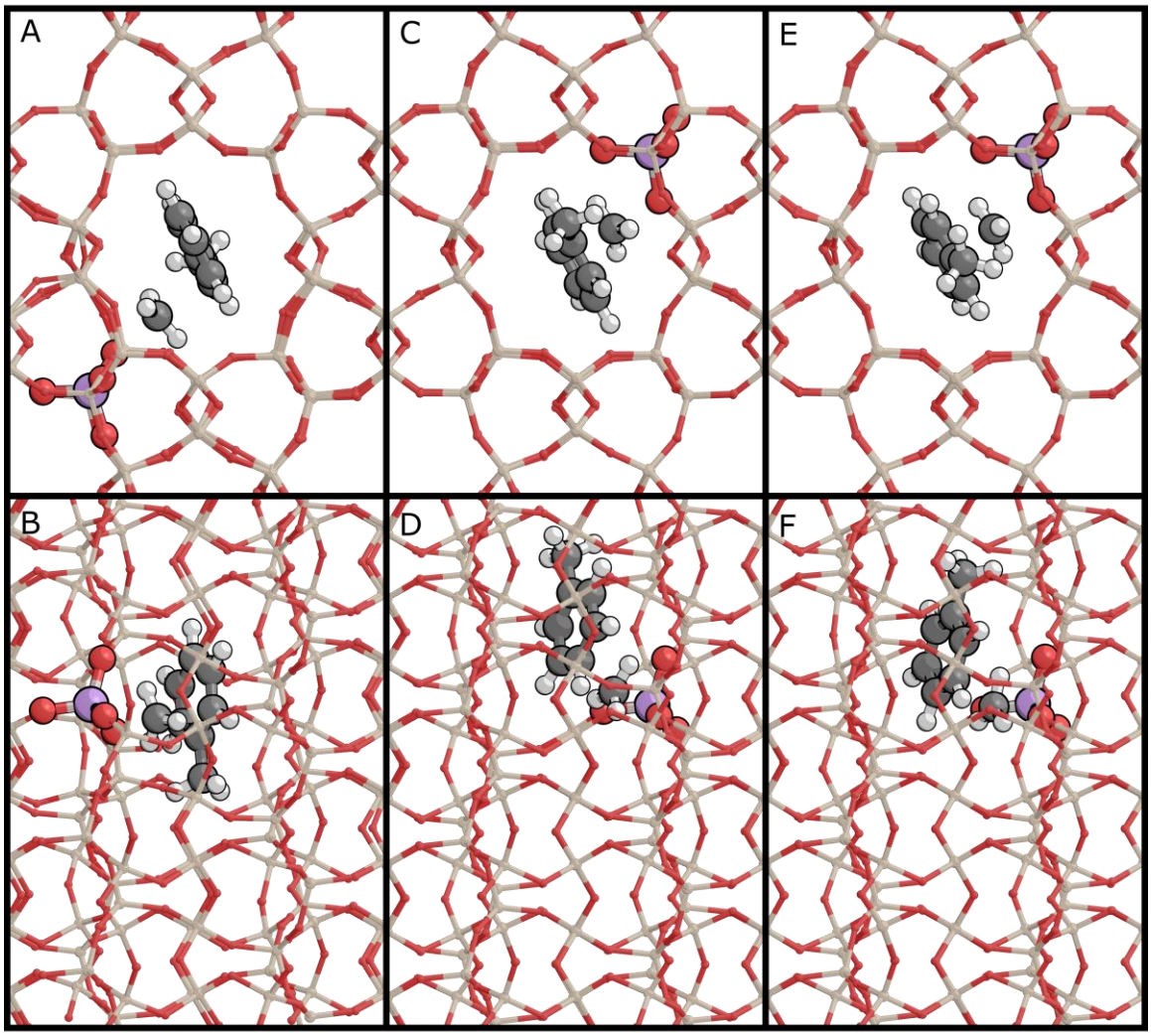

T2	o-xylene	m-xylene	p-xylene
O-atom	O5	O3	O3
$\Delta G_{act,int}$	*85*	*77*	*60*
$\Delta G_{act,eff}$	**166**	**157**	**140**

Fig. S65. Transition state structures for toluene methylation at TON-T2 viewed along the 010 (top) and 100 (bottom) axes. Activation free energies (ΔG_{act},kJ mol^{-1}) are reported at 403 K.

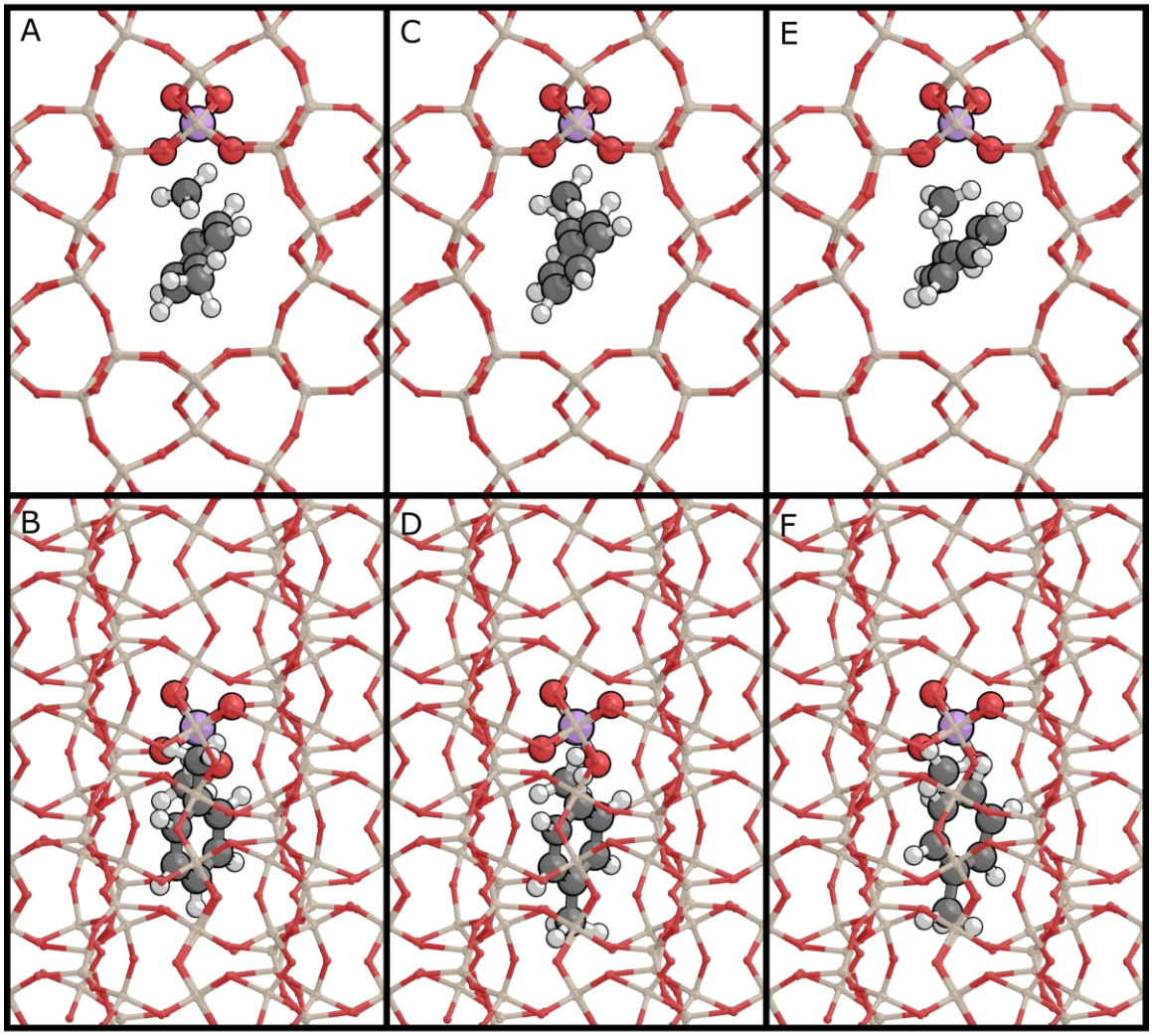

T3	o-xylene	m-xylene	p-xylene
O-atom	O4	O4	O4
$\Delta G_{act,int}$	*105*	*91*	*96*
$\Delta G_{act,eff}$	**143**	**129**	**134**

Fig. S66. Transition state structures for toluene methylation at TON-T3 viewed along the 010 (top) and 100 (bottom) axes. Activation free energies (ΔG_{act},kJ mol^{-1}) are reported at 403 K.

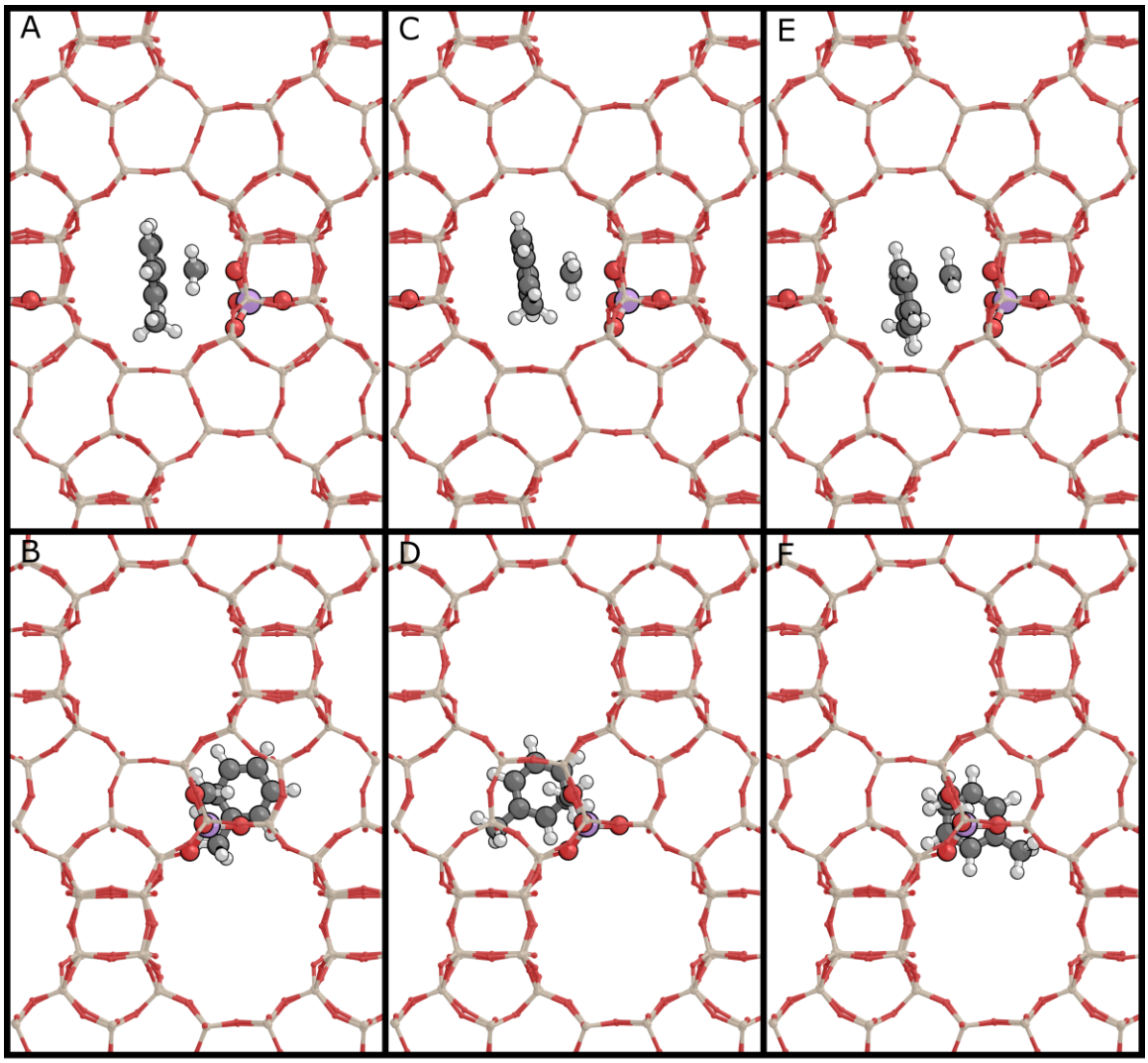

T1	o-xylene	m-xylene	p-xylene
O-atom	O2	O2	O2
$\Delta G_{act,int}$	*99*	*107*	*108*
$\Delta G_{act,eff}$	**73**	**81**	**82**

Fig. S67. Transition state structures for toluene methylation at BEA-T1 viewed along the 010 (top) and 100 (bottom) axes. Activation free energies (ΔG_{act},kJ mol^{-1}) are reported at 403 K.

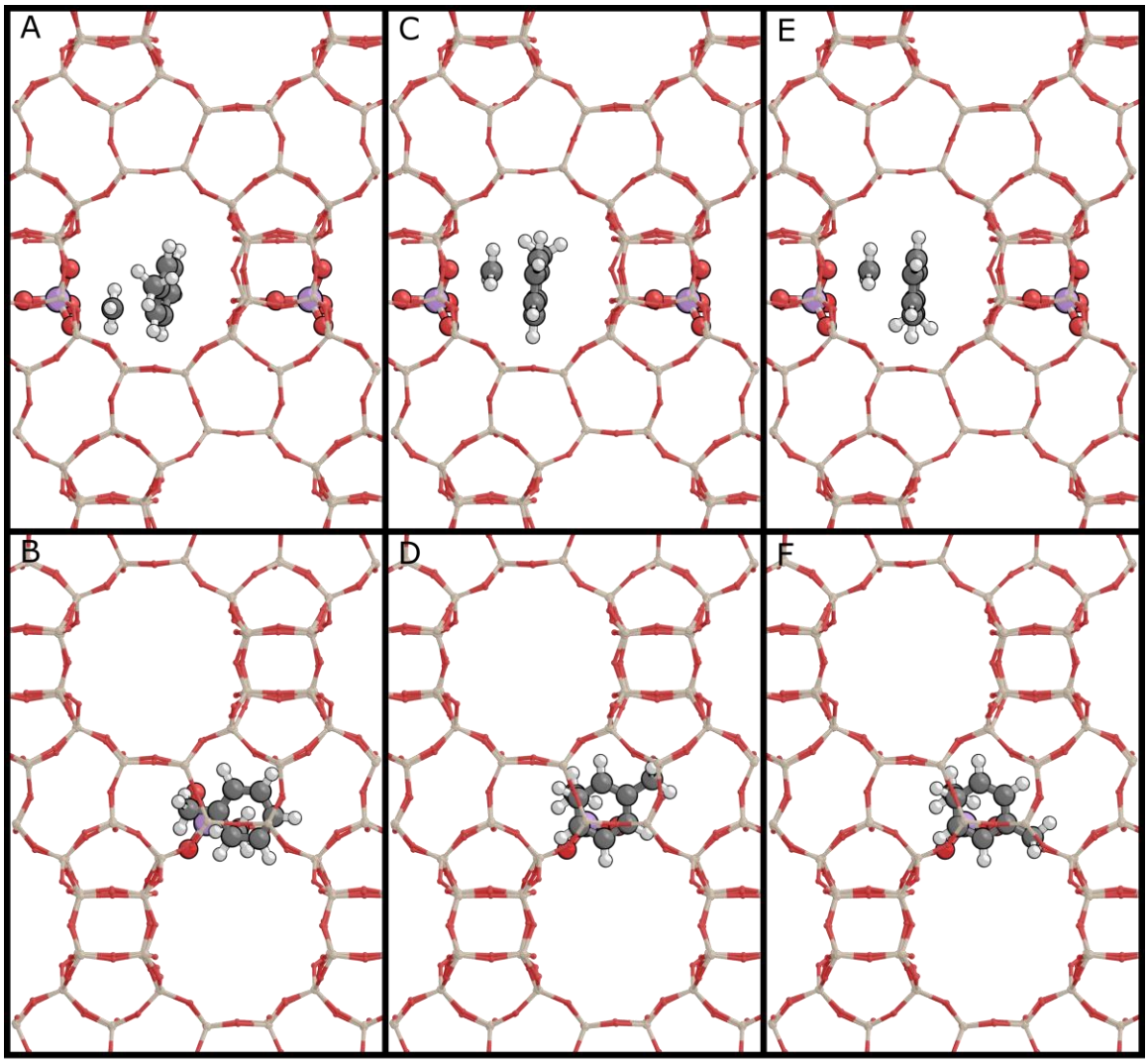

T2	o-xylene	m-xylene	p-xylene
O-atom	O5	O6	O6
$\Delta G_{act,int}$	*91*	*101*	*98*
$\Delta G_{act,eff}$	**75**	**84**	**81**

Fig. S68. Transition state structures for toluene methylation at BEA-T2 viewed along the 010 (top) and 100 (bottom) axes. Activation free energies (ΔG_{act},kJ mol^{-1}) are reported at 403 K.

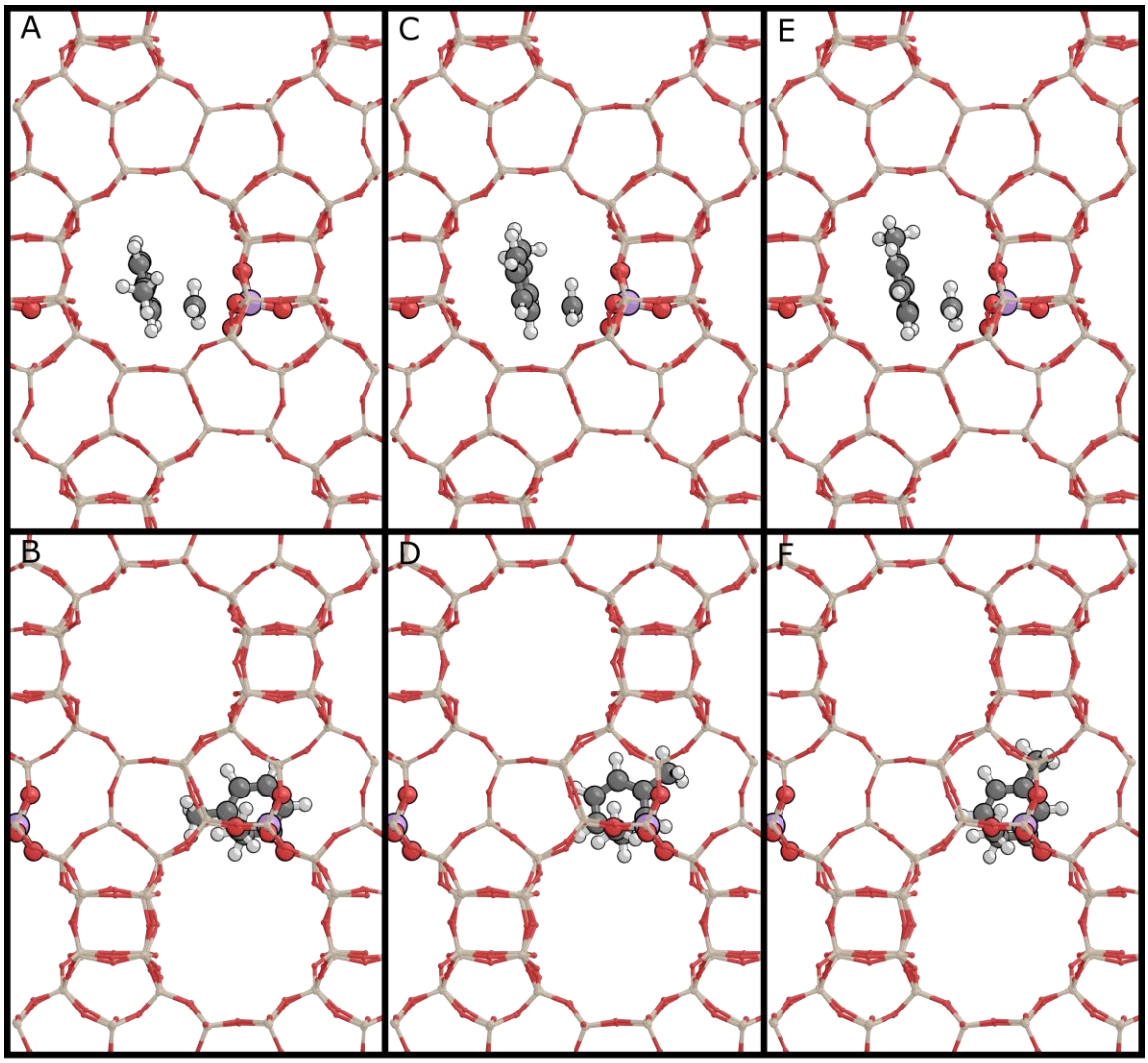

T3	o-xylene	m-xylene	p-xylene
O-atom	O1	O1	O1
$\Delta G_{act,int}$	*95*	*100*	*98*
$\Delta G_{act,eff}$	**74**	**79**	**77**

Fig. S69. Transition state structures for toluene methylation at BEA-T3 viewed along the 010 (top) and 100 (bottom) axes. Activation free energies (ΔG_{act},kJ mol^{-1}) are reported at 403 K.

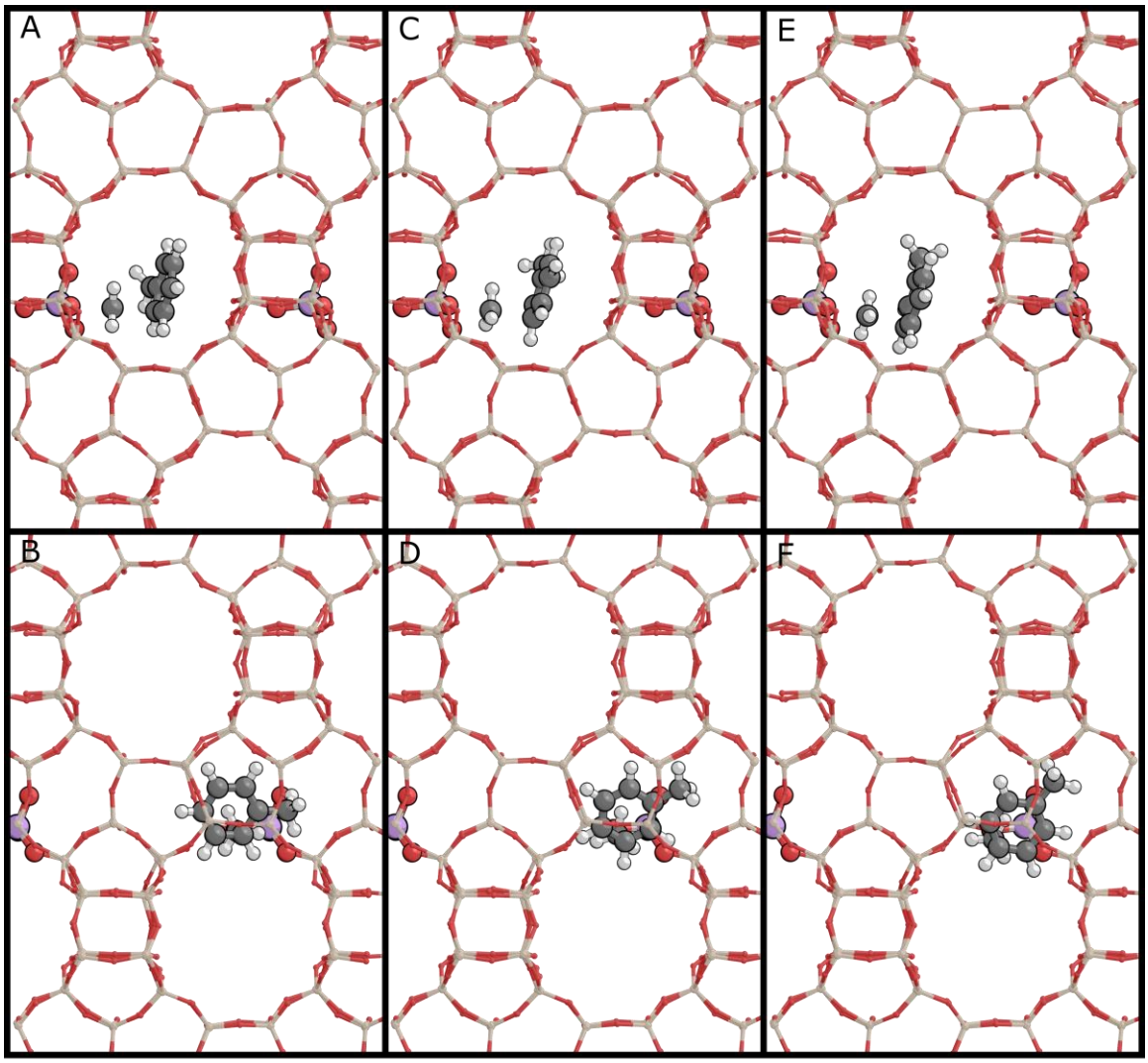

T4	o-xylene	m-xylene	p-xylene
O-atom	O5	O5	O5
$\Delta G_{act,int}$	*91*	*97*	*95*
$\Delta G_{act,eff}$	**76**	**82**	**80**

Fig. S70. Transition state structures for toluene methylation at BEA-T4 viewed along the 010 (top) and 100 (bottom) axes. Activation free energies (ΔG_{act},kJ mol^{-1}) are reported at 403 K.

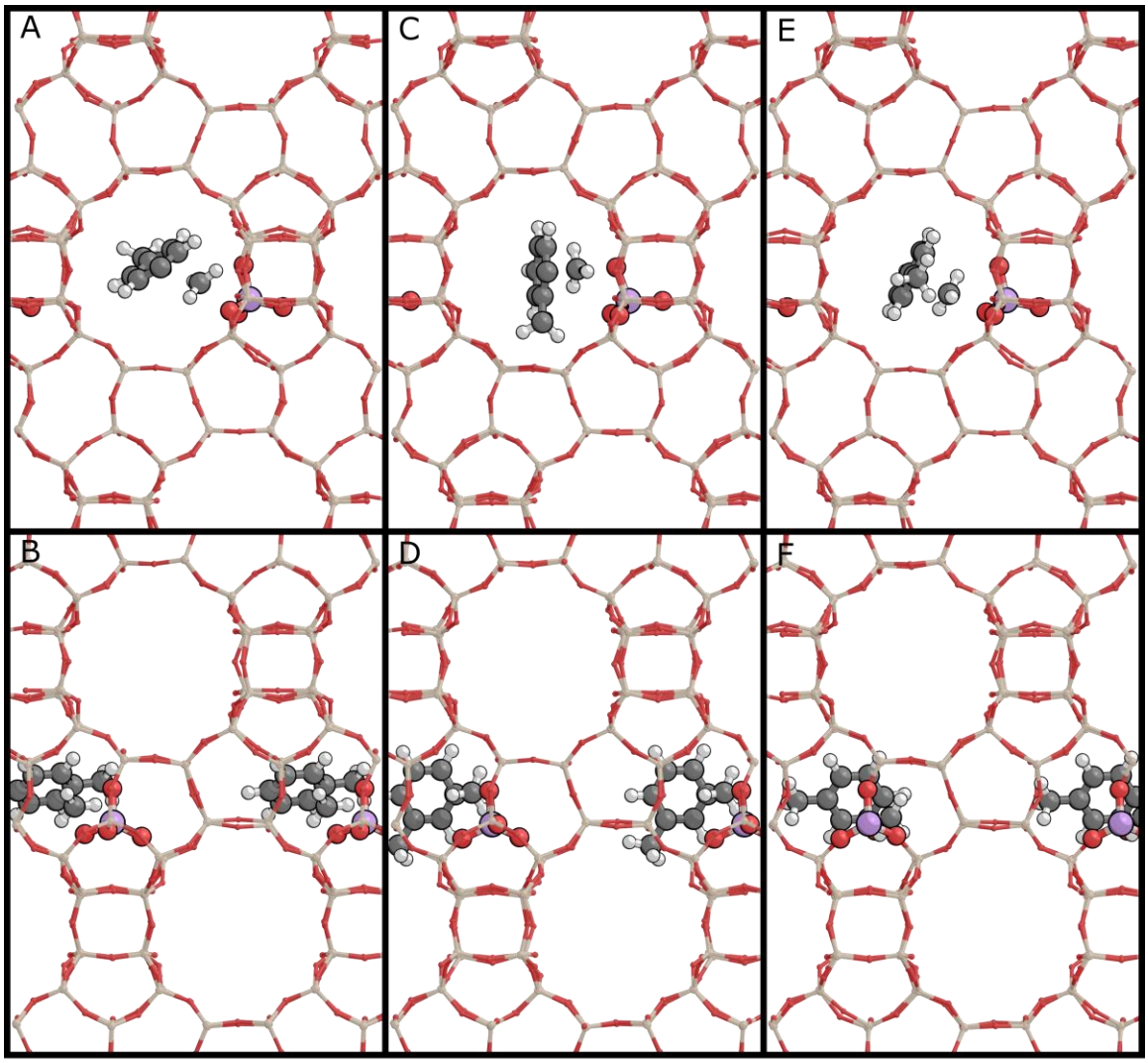

T5	o-xylene	m-xylene	p-xylene
O-atom	O13	O10	O15
$\Delta G_{act,int}$	*97*	*104*	*97*
$\Delta G_{act,eff}$	**80**	**86**	**79**

Fig. S71. Transition state structures for toluene methylation at BEA-T5 viewed along the 010 (top) and 100 (bottom) axes. Activation free energies (ΔG_{act},kJ mol^{-1}) are reported at 403 K.

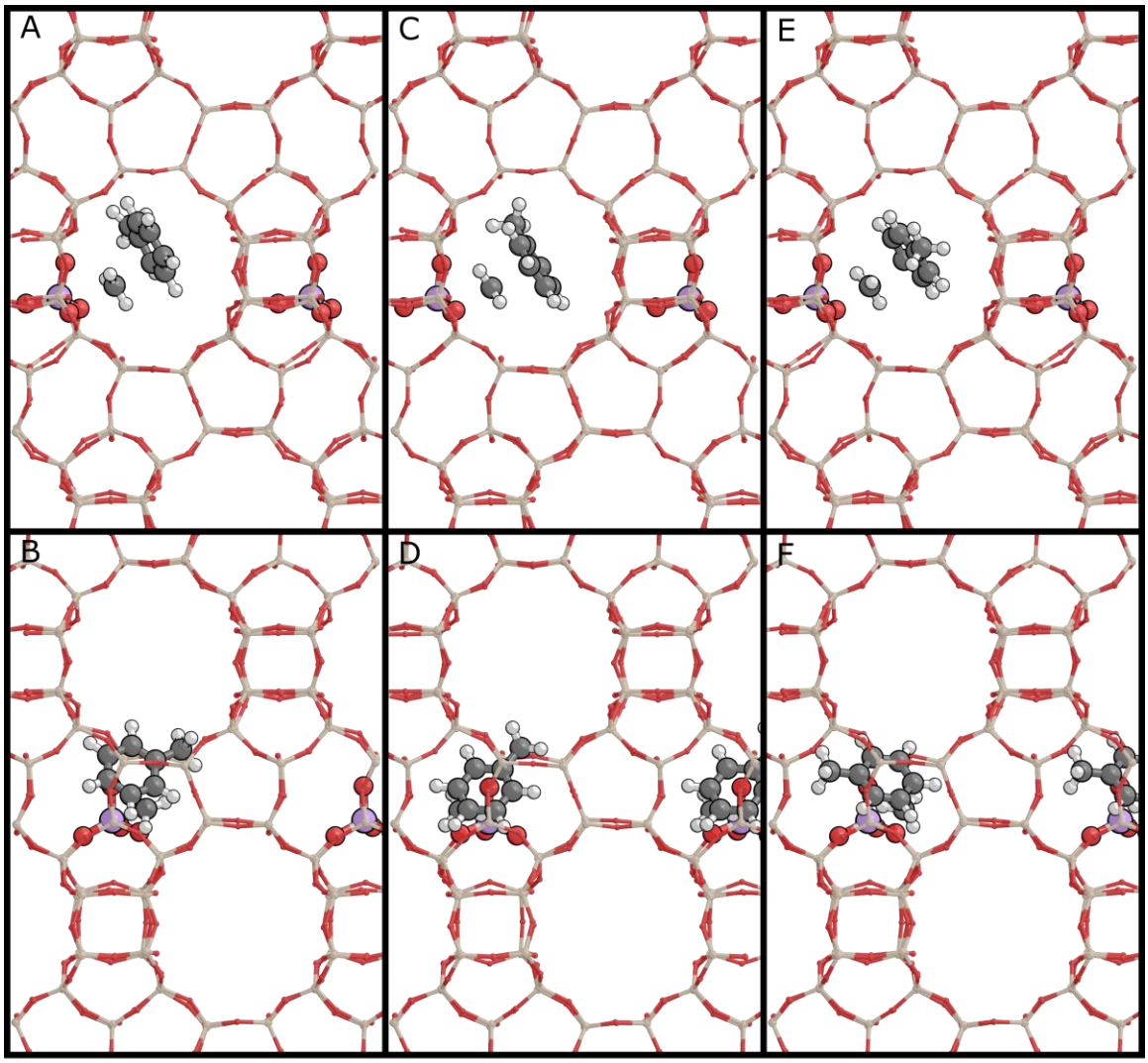

T6	o-xylene	m-xylene	p-xylene
O-atom	O17	O16	O17
$\Delta G_{act,int}$	*99*	*104*	*96*
$\Delta G_{act,eff}$	**84**	**89**	**81**

Fig. S72. Transition state structures for toluene methylation at BEA-T6 viewed along the 010 (top) and 100 (bottom) axes. Activation free energies (ΔG_{act},kJ mol^{-1}) are reported at 403 K.

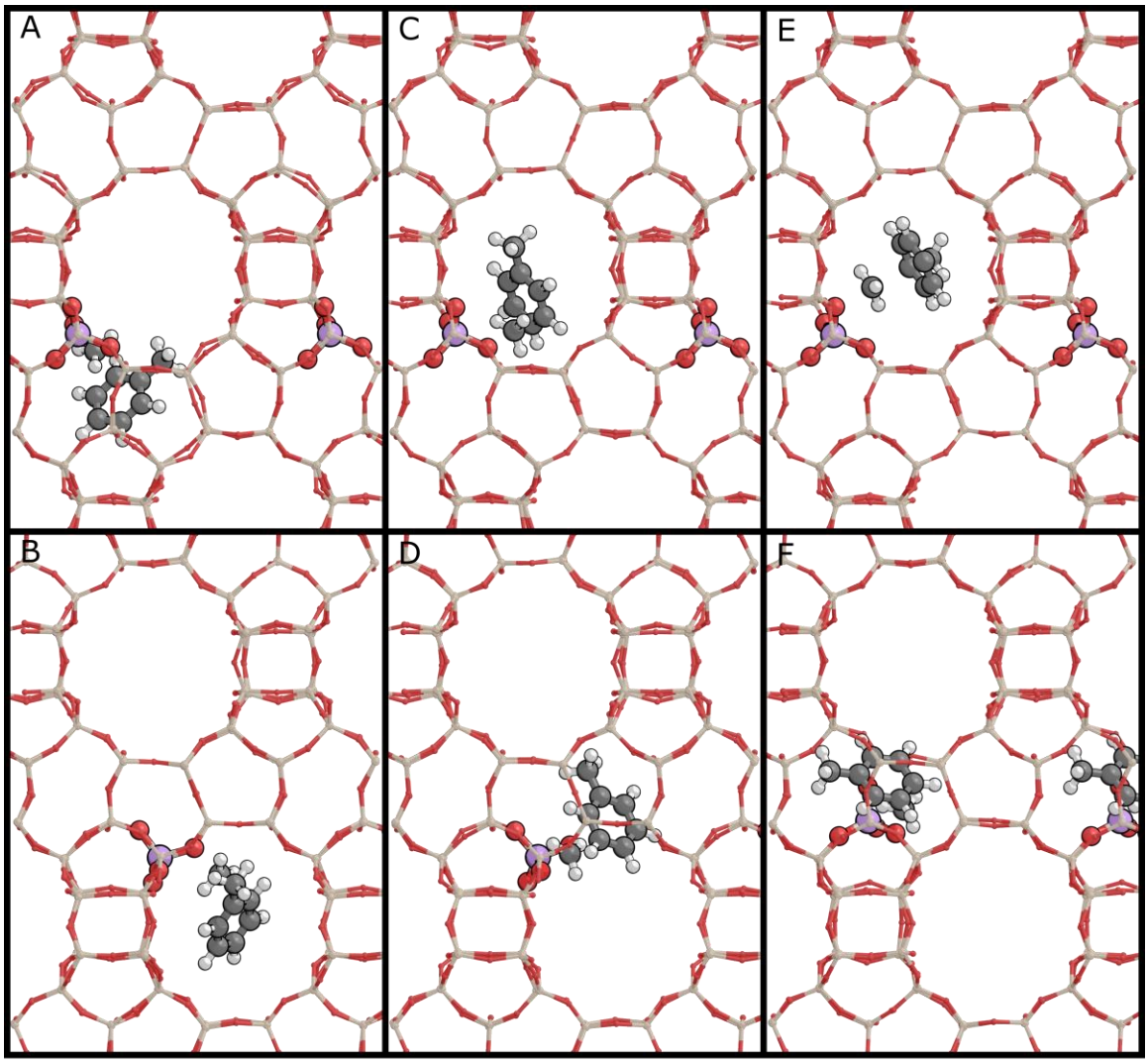

T7	o-xylene	m-xylene	p-xylene
O-atom	O7	O8	O17
$\Delta G_{act,int}$	*82*	*96*	*92*
$\Delta G_{act,eff}$	**71**	**86**	**81**

Fig. S73. Transition state structures for toluene methylation at BEA-T7 viewed along the 010 (top) and 100 (bottom) axes. Activation free energies (ΔG_{act},kJ mol^{-1}) are reported at 403 K.

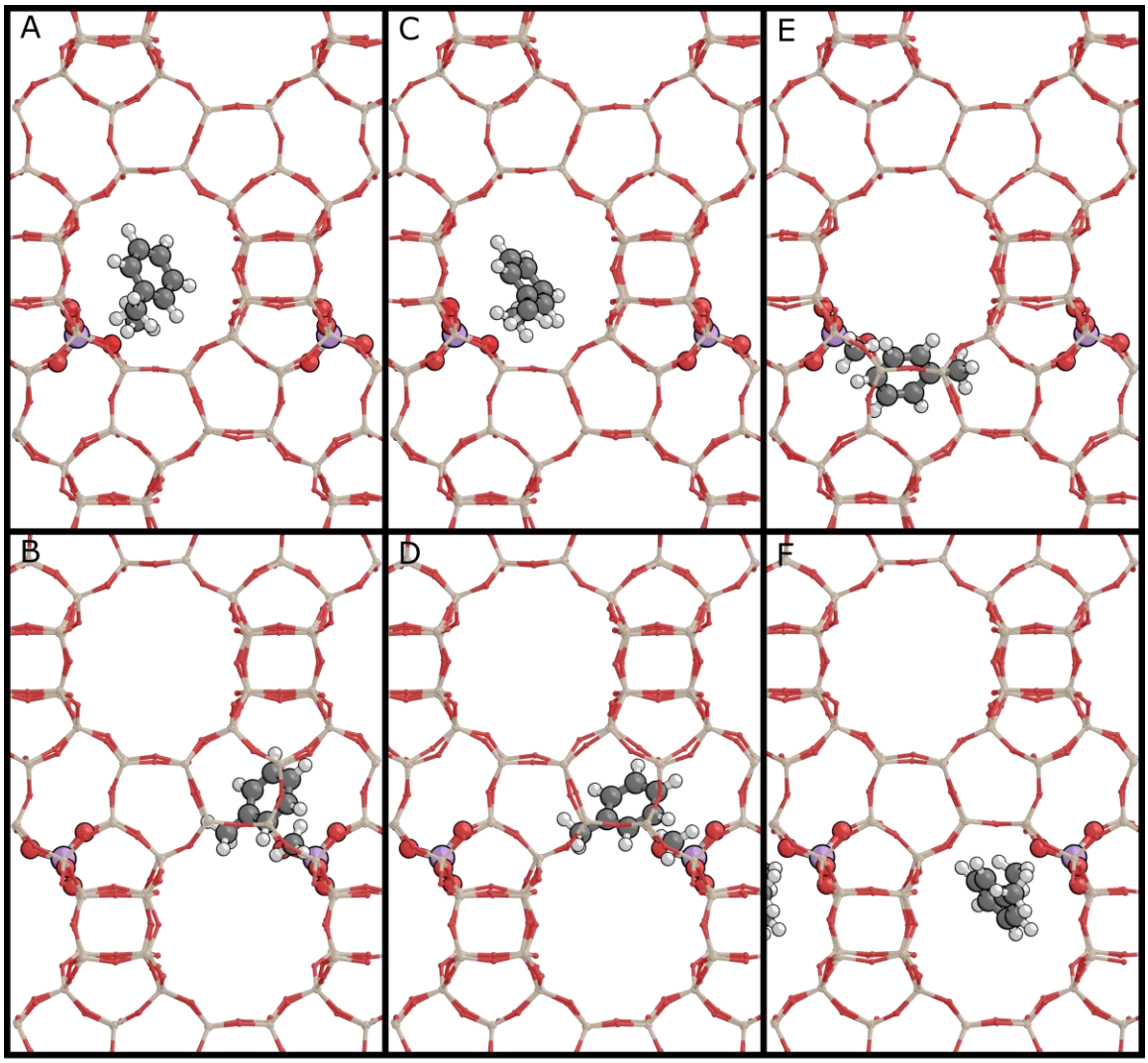

T8	o-xylene	m-xylene	p-xylene
O-atom	O11	O11	O11
$\Delta G_{act,int}$	*96*	*106*	*104*
$\Delta G_{act,eff}$	**73**	**83**	**81**

Fig. S74. Transition state structures for toluene methylation at BEA-T8 viewed along the 010 (top) and 100 (bottom) axes. Activation free energies (ΔG_{act},kJ mol^{-1}) are reported at 403 K.

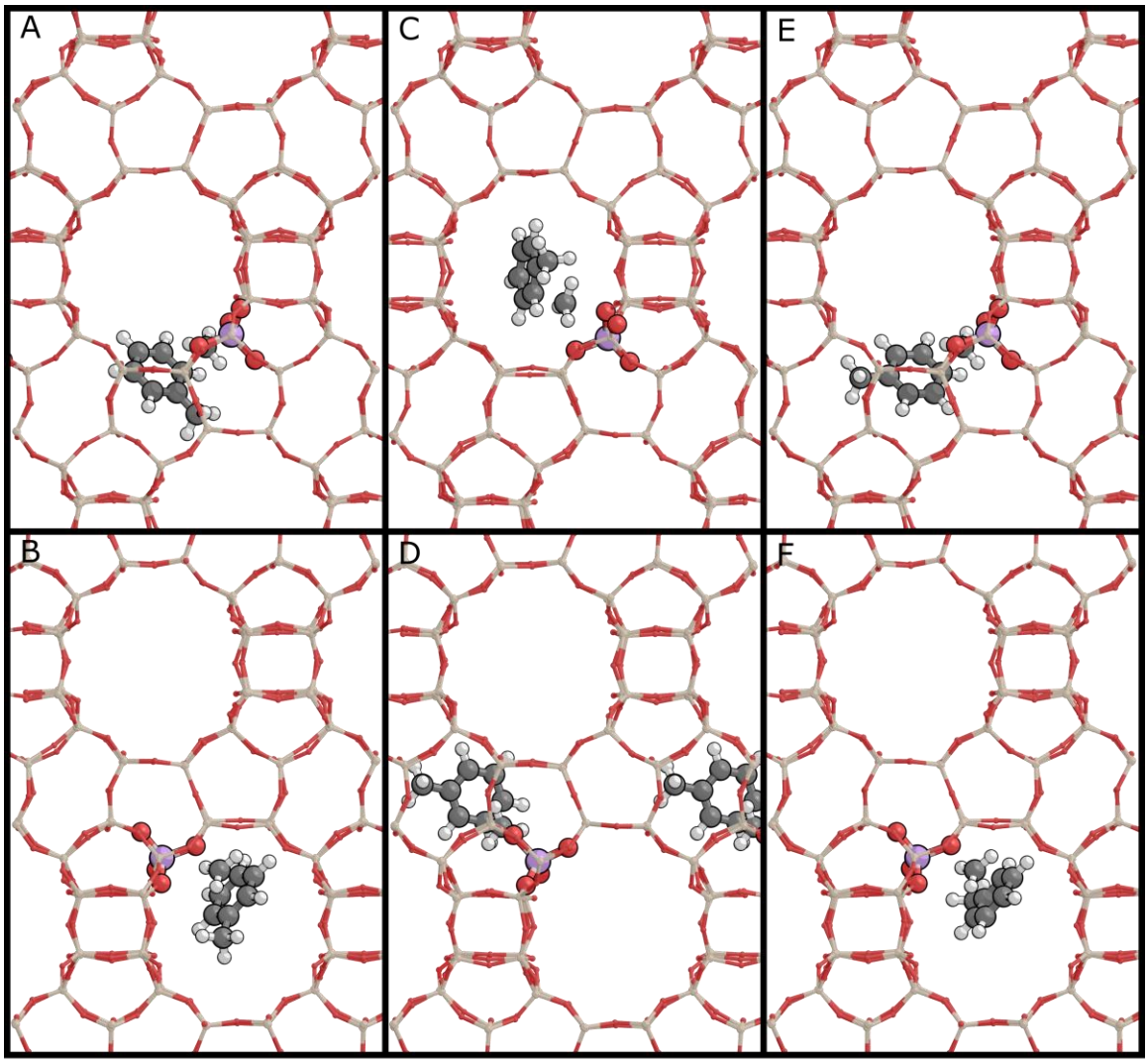

T9	o-xylene	m-xylene	p-xylene
O-atom	O3	O15	O3
$\Delta G_{act,int}$	*98*	*106*	*104*
$\Delta G_{act,eff}$	**78**	**85**	**83**

Fig. S75. Transition state structures for toluene methylation at BEA-T9 viewed along the 010 (top) and 100 (bottom) axes. Activation free energies (ΔG_{act},kJ mol^{-1}) are reported at 403 K.

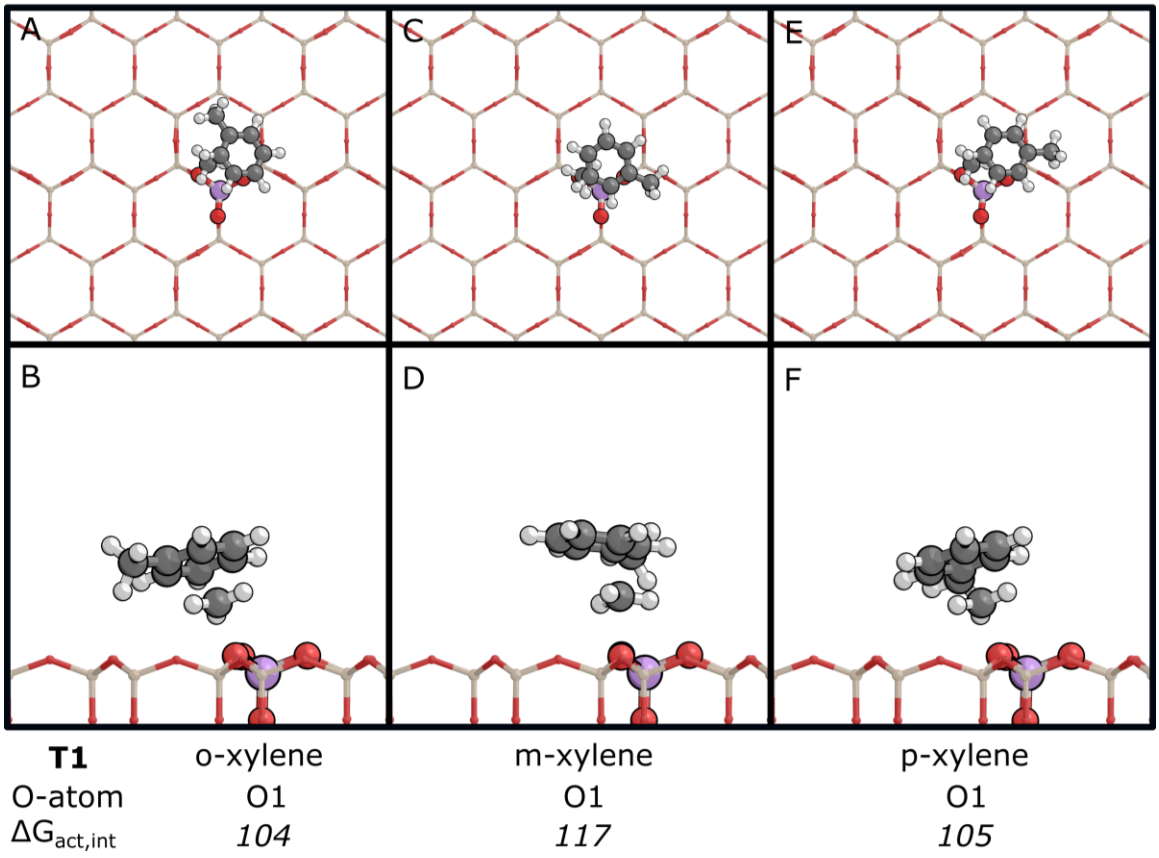

Fig. S76. Transition state structures for toluene methylation at unconfined 2D zeolite viewed along the 010 (top) and 100 (bottom) axes. Activation free energies (ΔG_{act},kJ mol^{-1}) are reported at 403 K.

S5.21. DFT structures of organic structure directing agents in MFI

Electrostatic interactions between organic structure directing agents (OSDA) and Al from zeolite framework influence the Al siting at lattice positions close to the charged nitrogen (N^+) centers of the occluded OSDA. Figures S77 to S78 and Figures S79 to S80 show structures for MFI with DABCO structure directing agent with methylamine (MA) and water (H_2O) respectively, across all T-sites in MFI. Specifically, structures consist of a protonated DABCO-H-MA^+ or DABCO-H-H_2O^+ complexes interacting with Al from framework with three neutral DABCO-MA(H_2O) complexes in the remaining MFI intersections to simulate occlusion. As such, the reported relative energies are a thermodynamic proxy to assess the favorability to substitute Al at framework positions around protonated complexes between DABCO and MA or H_2O. Relative energies reported for DABCO-MA complexes are relative to T5, while those reported for DABCO-H_2O complexes are relative to T12 as these were the relatively lowest energies computed for these complexes, respectively.

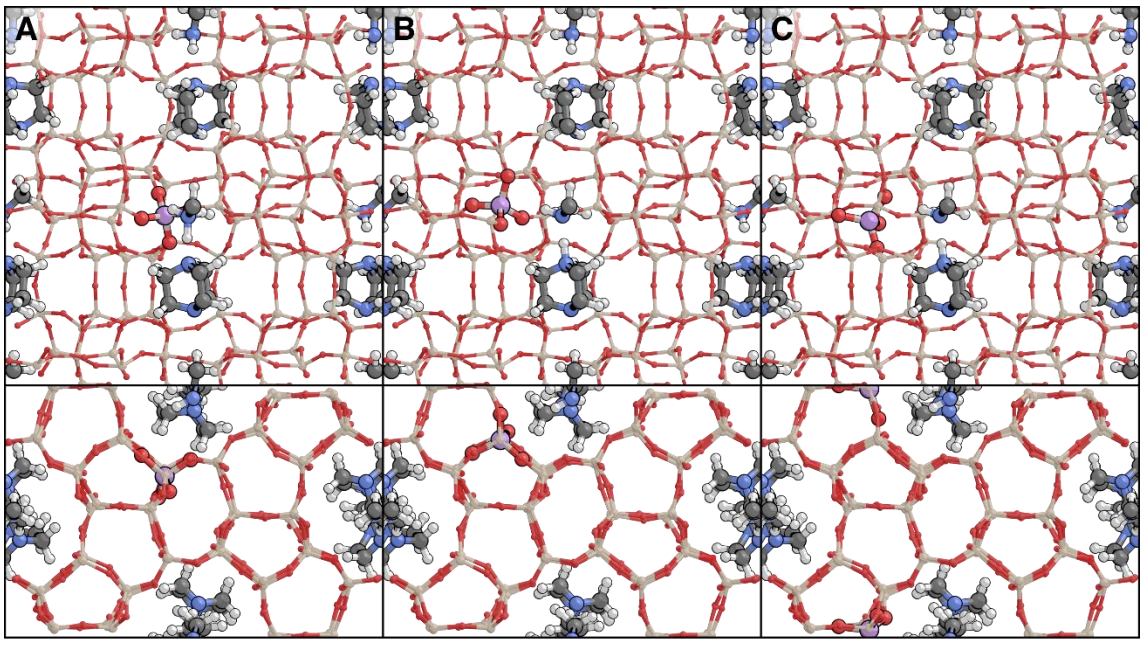

	T1	T2	T3
Δ*E* (vac)	9	5	3
Δ*E* (sol)	9	6	4

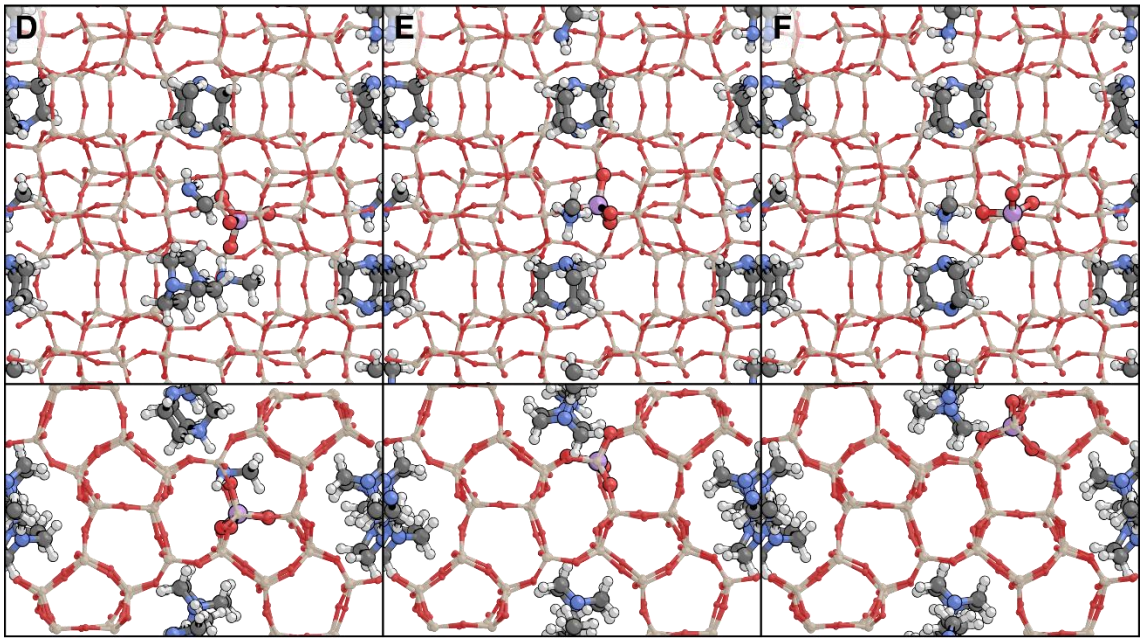

	T4	T5	T6
Δ*E* (vac)	7	0	9
Δ*E* (sol)	1	0	9

Fig. S77. Structures for MFI with 4 DABCO and 4 MA molecules with one protonated complex and Al substituted in (A) T1, (B) T2, (C) T3, (D) T4, (E) T5, and (F) T6 shown down the *c*-vector (top) and the *b*-vector (bottom). Each structure is labeled with its relative electronic energy (Δ*E*) in kJ mol^{-1} in vacuum and with implicit solvent (ϵ = 80).

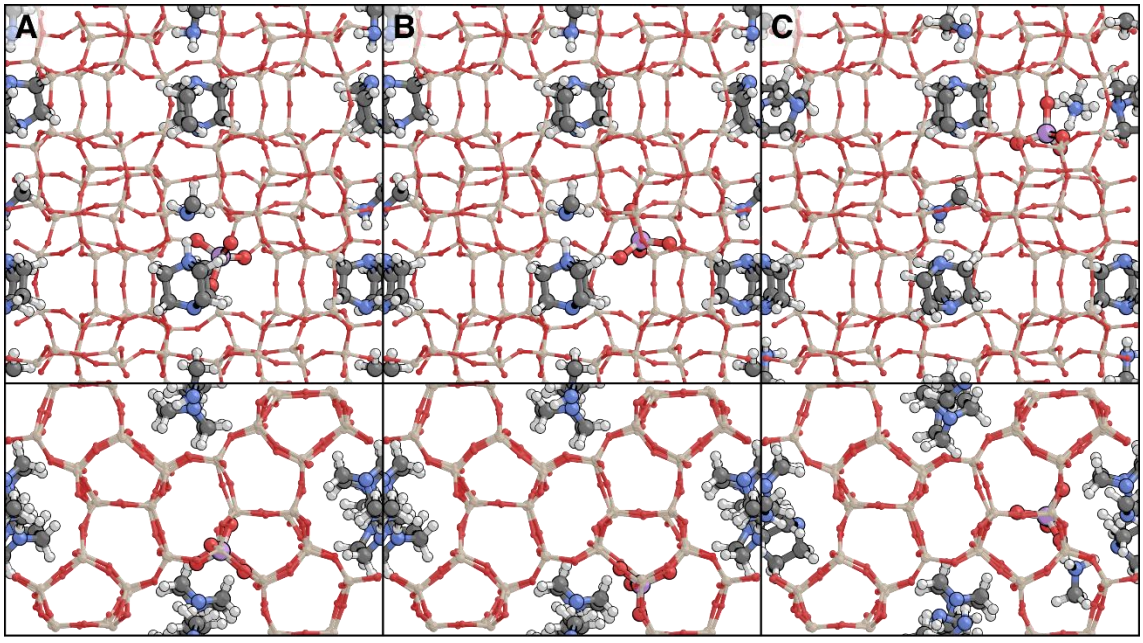

	T7	T8	T9
Δ*E* (vac)	17	9	10
Δ*E* (sol)	15	9	9

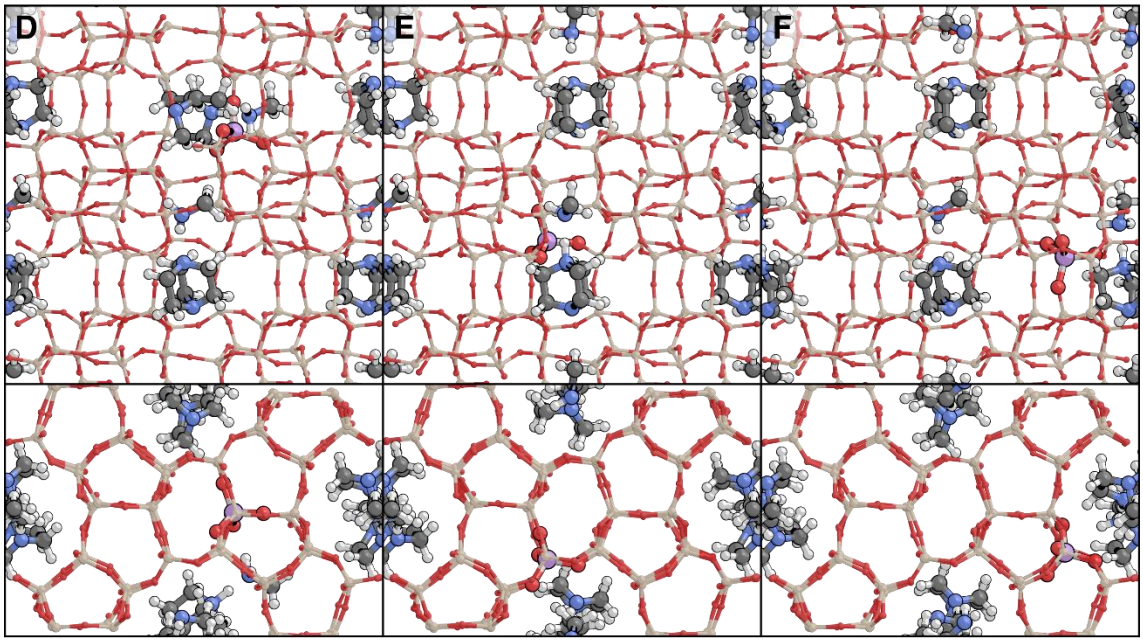

	T10	T11	T12
Δ*E* (vac)	12	6	2
Δ*E* (sol)	17	7	8

Fig. S78. Structures for MFI with 4 DABCO and 4 MA molecules with one protonated complex and Al substituted in (A) T7, (B) T8, (C) T9, (D) T10, (E) T11, and (F) T12 shown down the *c*-vector (top) and the *b*-vector (bottom). Each structure is labeled with its relative electronic energy (ΔE) in kJ mol^{-1} in vacuum and with implicit solvent ($\epsilon = 80$).

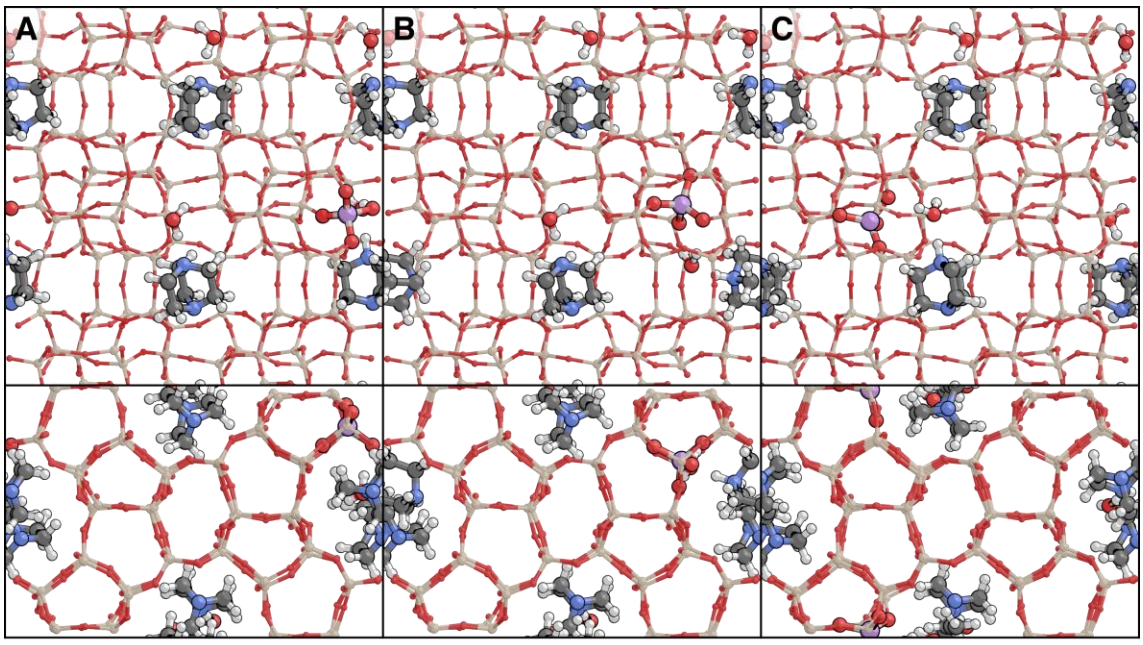

	T1	T2	T3
Δ*E* (vac)	12	10	7
Δ*E* (sol)	16	11	4

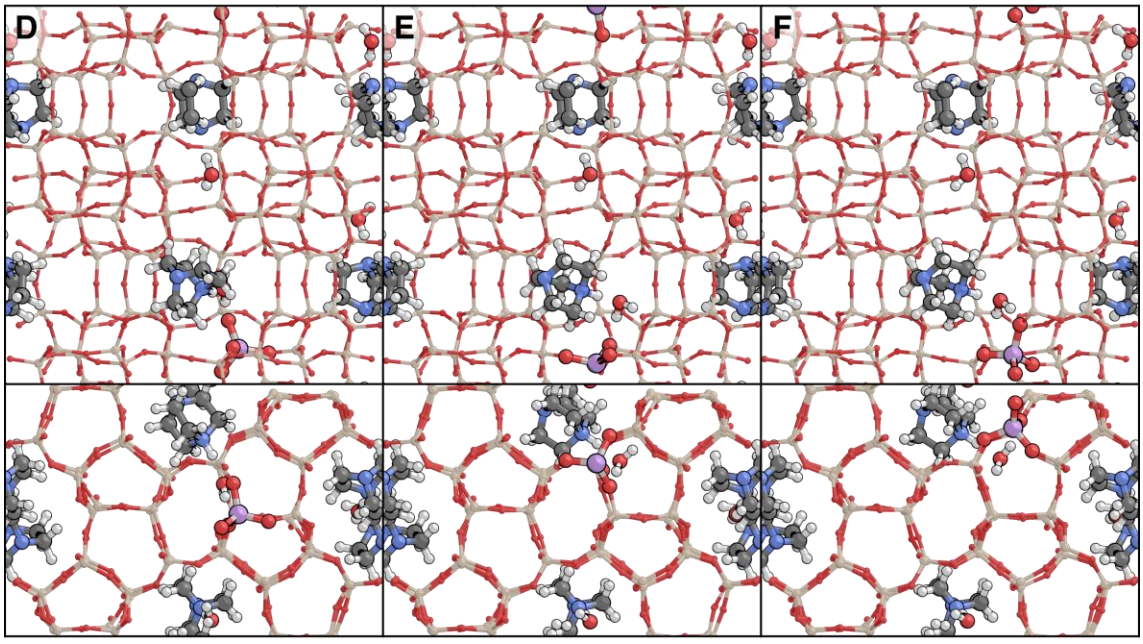

	T4	T5	T6
Δ*E* (vac)	17	5	18
Δ*E* (sol)	12	4	15

Fig. S79. Structures for MFI with 4 DABCO and 4 H_2O molecules with one protonated complex and Al substituted in (A) T1, (B) T2, (C) T3, (D) T4, (E) T5, and (F) T6 shown down the *c*-vector (top) and the *b*-vector (bottom). Each structure is labeled with its relative electronic energy (ΔE) in kJ mol^{-1} in vacuum and with implicit solvent ($\epsilon = 80$).

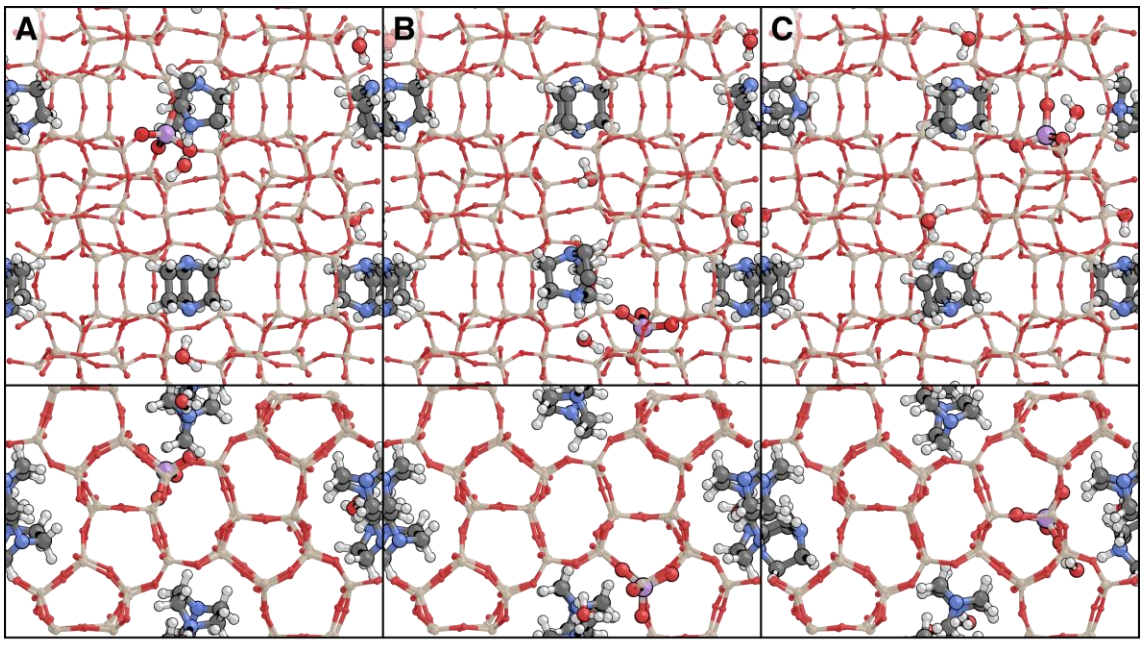

	T7	T8	T9
Δ*E* (vac)	17	15	14
Δ*E* (sol)	14	14	24

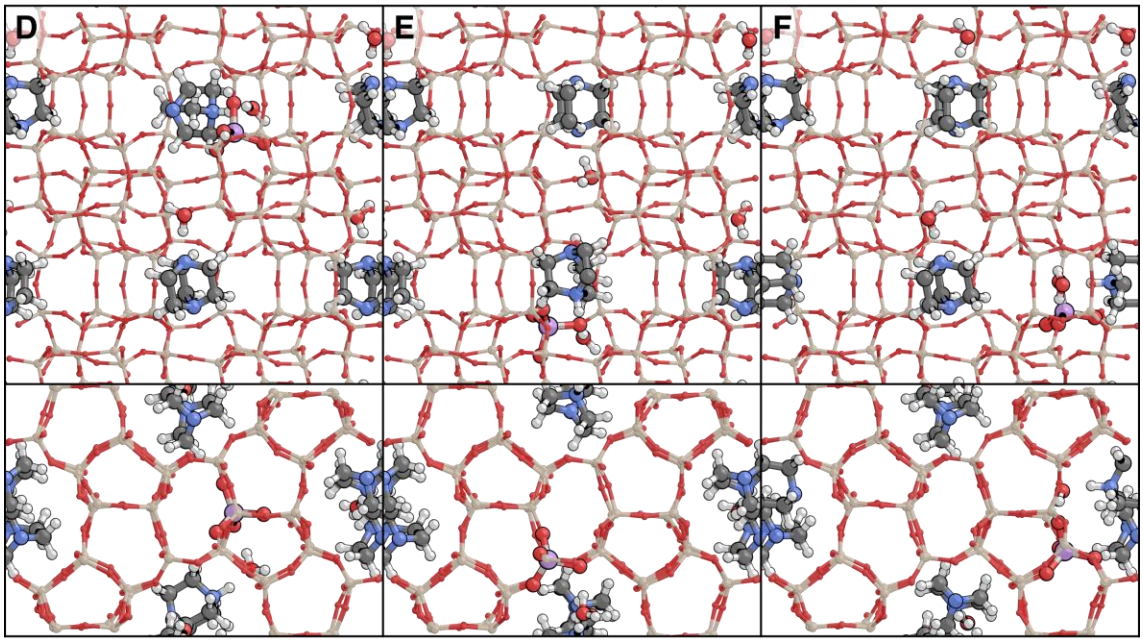

	T10	T11	T12
Δ*E* (vac)	18	15	0
Δ*E* (sol)	12	8	0

Fig. S80. Structures for MFI with 4 DABCO and 4 H_2O molecules with one protonated complex and Al substituted in (A) T7, (B) T8, (C) T9, (D) T10, (E) T11, and (F) T12 shown down the *c*-vector (top) and the *b*-vector (bottom). Each structure is labeled with its relative electronic energy (ΔE) in kJ mol^{-1} in vacuum and with implicit solvent ($\epsilon = 80$).

S5.22. Analysis of organic SDA in as-synthesized MFI-DABCO using ^{13}C MAS NMR

We performed a preliminary $^{1}H \rightarrow ^{13}C$ cross-polarized magic angle spinning nuclear magnetic resonance (CP MAS NMR) measurement which shows that DABCO and MA are co-occluded and intact in an as-synthesized MFI-DABCO sample (Fig. S81). Spectra were recorded under ambient conditions using a Chemagnetics CMX-Innity 400 spectrometer in a wide-bore 9.4 T magnet (Purdue Interdepartmental NMR Facility). We thank Dr. John Harwood for assistance with the ^{13}C CP SS MAS NMR.

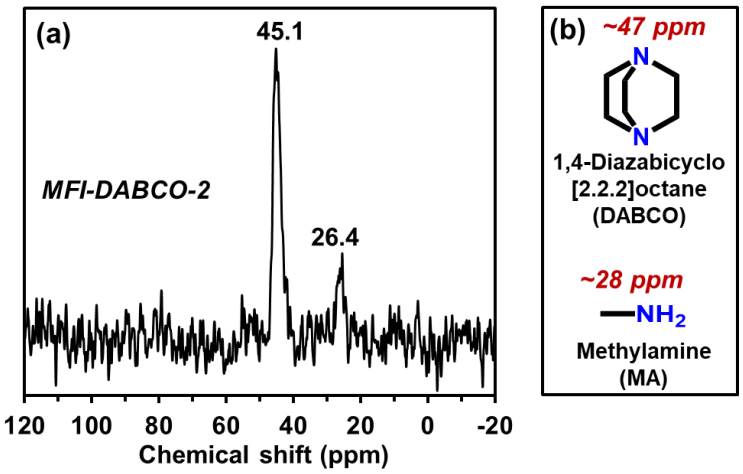

Fig. S81. (a) ^{13}C CP SS MAS NMR of as-synthesized MFI-DABCO-2 (b) ^{13}C NMR chemical shifts (from PubChem[87,88]) of unprotonated DABCO and MA (in D_2O) are shown for reference.

REFERENCES

(1) Hur, Y. G.; Kester, P. M.; Nimlos, C. T.; Cho, Y.; Miller, J. T.; Gounder, R. Influence of Tetrapropylammonium and Ethylenediamine Structure-Directing Agents on the Framework Al Distribution in B–Al–MFI Zeolites. *Ind. Eng. Chem. Res.* **2019**, *58* (27), 11849–11860. https://doi.org/10.1021/acs.iecr.9b01726.

(2) Nimlos, C. T.; Hoffman, A. J.; Hur, Y. G.; Lee, B. J.; Di Iorio, J. R.; Hibbitts, D. D.; Gounder, R. Experimental and Theoretical Assessments of Aluminum Proximity in MFI Zeolites and Its Alteration by Organic and Inorganic Structure-Directing Agents. *Chem. Mater.* **2020**, *32* (21), 9277–9298. https://doi.org/10.1021/acs.chemmater.0c03154.

(3) Bickel, E. E.; Lee, S.; Gounder, R. Influence of Brønsted Acid-Site Density on Reaction-Diffusion Phenomena That Govern Propene Oligomerization Rate and Selectivity in MFI Zeolites. *ACS Catal.* **2023**, *13* (2), 1257–1269. https://doi.org/10.1021/acscatal.2c05184.

(4) Kester, P. M.; Miller, J. T.; Gounder, R. Ammonia Titration Methods To Quantify Brønsted Acid Sites in Zeolites Substituted with Aluminum and Boron Heteroatoms. *Ind. Eng. Chem. Res.* **2018**, *57* (19), 6673–6683. https://doi.org/10.1021/acs.iecr.8b00933.

(5) Kim, K.; Ryoo, R.; Jang, H.-D.; Choi, M. Spatial Distribution, Strength, and Dealumination Behavior of Acid Sites in Nanocrystalline MFI Zeolites and Their Catalytic Consequences. *J. Catal.* **2012**, *288*, 115–123. https://doi.org/10.1016/j.jcat.2012.01.009.

(6) Baerlocher, C.; McCusker, L. B. *Database of Zeolite Structures*. http://www.iza-structure.org/databases/ (accessed 2019-08-11).

(7) Borghard, W. S.; Sheppard, E. W.; Schoennagel, H. J. An Automated, High Precision Unit for Low-pressure Physisorption. *Rev. Sci. Instrum.* **1991**, *62* (11), 2801–2809. https://doi.org/10.1063/1.1142216.

(8) Massiot, D.; Fayon, F.; Alonso, B.; Trebosc, J.; Amoureux, J.-P. Chemical Bonding Differences Evidenced from J-Coupling in Solid State NMR Experiments Involving Quadrupolar Nuclei. *J. Magn. Reson.* **2003**, *164* (1), 160–164. https://doi.org/10.1016/S1090-7807(03)00134-4.

(9) Scanlon, J. T.; Willis, D. E. Calculation of Flame Ionization Detector Relative Response Factors Using the Effective Carbon Number Concept. *J. Chromatogr. Sci.* **1985**, *23* (8), 333–340. https://doi.org/10.1093/chromsci/23.8.333.

(10) Kresse, G.; Hafner, J. Ab Initio Molecular Dynamics for Liquid Metals. *Phys. Rev. B* **1993**, *47* (1), 558–561. https://doi.org/10.1103/PhysRevB.47.558.

(11) Kresse, G.; Hafner, J. Ab Initio Molecular-Dynamics Simulation of the Liquid-Metal-Amorphous-Semiconductor Transition in Germanium. *Phys. Rev. B* **1994**, *49* (20), 14251–14269.

(12) Kresse, G.; Furthmüller, J. Efficient Iterative Schemes for Ab Initio Total-Energy Calculations Using a Plane-Wave Basis Set. *Phys. Rev. B* **1996**, *54* (16), 11169–11186. https://doi.org/10.1103/PhysRevB.54.11169.

(13) Kresse, G.; Furthmüller, J. Efficiency of Ab-Initio Total Energy Calculations for Metals and Semiconductors Using a Plane-Wave Basis Set. *Comput. Mater. Sci.* **1996**, *6* (1), 15–50. https://doi.org/10.1016/0927-0256(96)00008-0.

(14) Kravchenko, P.; Plaisance, C.; Hibbitts, D. A New Computational Interface for Catalysis. **2019**. https://doi.org/10.26434/chemrxiv.8040737.v4.

(15) Blöchl, P. E. Projector Augmented-Wave Method. *Phys. Rev. B* **1994**, *50* (24), 17953–17979. https://doi.org/10.1103/PhysRevB.50.17953.

(16) Kresse, G.; Joubert, D. From Ultrasoft Pseudopotentials to the Projector Augmented-Wave Method. *Phys. Rev. B* **1999**, *59* (3), 1758–1775. https://doi.org/10.1103/PhysRevB.59.1758.

(17) Perdew, J.; Burke, K.; Ernzerhof, M. Generalized Gradient Approximation Made Simple. *Phys. Rev. Lett.* **1996**, *77* (18), 3865–3868. https://doi.org/10.1103/PhysRevLett.77.3865.

(18) Zhang, Y.; Yang, W. Comment on "Generalized Gradient Approximation Made Simple." *Phys. Rev. Lett.* **1998**, *80* (4), 890–890. https://doi.org/10.1103/PhysRevLett.80.890.

(19) Hammer, B.; Hansen, L. B.; Nørskov, J. K. Improved Adsorption Energetics within Density-Functional Theory Using Revised Perdew-Burke-Ernzerhof Functionals. *Phys. Rev. B* **1999**, *59* (11), 7413–7421. https://doi.org/10.1103/PhysRevB.59.7413.

(20) Grimme, S.; Ehrlich, S.; Goerigk, L. Effect of the Damping Function in Dispersion Corrected Density Functional Theory. *J. Comput. Chem.* **2011**, *32* (7), 1456–1465. https://doi.org/10.1002/jcc.21759.

(21) Schröder, H.; Creon, A.; Schwabe, T. Reformulation of the D3(Becke-Johnson) Dispersion Correction without Resorting to Higher than C_6 Dispersion Coefficients. *J. Chem. Theory Comput.* **2015**, *11* (7), 3163–3170. https://doi.org/10.1021/acs.jctc.5b00400.

(22) Grimme, S.; Antony, J.; Ehrlich, S.; Krieg, H. A Consistent and Accurate Ab Initio Parametrization of Density Functional Dispersion Correction (DFT-D) for the 94 Elements H-Pu. *J. Chem. Phys.* **2010**, *132* (15), 154104. https://doi.org/10.1063/1.3382344.

(23) van Koningsveld, H. High-Temperature (350 K) Orthorhombic Framework Structure of Zeolite H-ZSM-5. *Acta Crystallogr. B* **1990**, *46* (6), 731–735. https://doi.org/10.1107/S0108768190007522.

(24) Hoffman, A.; DeLuca, M.; Hibbitts, D. Restructuring of MFI Framework Zeolite Models and Their Associated Artifacts in Density Functional Theory Calculations. *J. Phys. Chem. C* **2019**, *123* (11), 6572–6585. https://doi.org/10.1021/acs.jpcc.8b12230.

(25) Monkhorst, H. J.; Pack, J. D. Special Points for Brillouin-Zone Integrations. *Phys. Rev. B* **1976**, *13* (12), 5188–5192. https://doi.org/10.1103/PhysRevB.13.5188.

(26) Mathew, K.; Sundararaman, R.; Letchworth-Weaver, K.; Arias, T. A.; Hennig, R. G. Implicit Solvation Model for Density-Functional Study of Nanocrystal Surfaces and Reaction Pathways. *J. Chem. Phys.* **2014**, *140* (8), 084106. https://doi.org/10.1063/1.4865107.

(27) Archer, D. G.; Wang, P. The Dielectric Constant of Water and Debye-Hückel Limiting Law Slopes. *J. Phys. Chem. Ref. Data* **1990**, *19* (2), 371–411. https://doi.org/10.1063/1.555853.

(28) DeLuca, M.; Kravchenko, P.; Hoffman, A.; Hibbitts, D. Mechanism and Kinetics of Methylating C6–C12 Methylbenzenes with Methanol and Dimethyl Ether in H-MFI Zeolites. *ACS Catal.* **2019**, *9* (7), 6444–6460. https://doi.org/10.1021/acscatal.9b00650.

(29) Henkelman, G.; Jónsson, H. A Dimer Method for Finding Saddle Points on High Dimensional Potential Surfaces Using Only First Derivatives. *J. Chem. Phys.* **1999**, *111* (15), 7010–7022. https://doi.org/10.1063/1.480097.

(30) Ghorbanpour, A.; Rimer, J. D.; Grabow, L. C. Computational Assessment of the Dominant Factors Governing the Mechanism of Methanol Dehydration over H-ZSM-5 with Heterogeneous Aluminum Distribution. *ACS Catal.* **2016**, *6* (4), 2287–2298. https://doi.org/10.1021/acscatal.5b02367.

(31) Martinez-Espin, J. S.; Mortén, M.; Janssens, T. V. W.; Svelle, S.; Beato, P.; Olsbye, U. New Insights into Catalyst Deactivation and Product Distribution of Zeolites in the Methanol-to-Hydrocarbons (MTH) Reaction with Methanol and Dimethyl Ether Feeds. *Catal. Sci. Technol.* **2017**, *7* (13), 2700–2716. https://doi.org/10.1039/C7CY00129K.

(32) Montalvo-Castro, H.; DeLuca, M.; Kilburn, L.; Hibbitts, D. Mechanisms and Kinetics of the Dehydrogenation of C6–C8 Cycloalkanes, Cycloalkenes, and Cyclodienes to Aromatics in H-MFI Zeolite Framework. *ACS Catal.* **2022**, 99–112. https://doi.org/10.1021/acscatal.2c03360.

(33) Ahn, J. H.; Kolvenbach, R.; Gutiérrez, O. Y.; Al-Khattaf, S. S.; Jentys, A.; Lercher, J. A. Tailoring P-Xylene Selectivity in Toluene Methylation on Medium Pore-Size Zeolites. *Microporous Mesoporous Mater.* **2015**, *210*, 52–59. https://doi.org/10.1016/j.micromeso.2015.02.018.

(34) Kaeding, W. W.; Chu, C.; Young, L. B.; Weinstein, B.; Butter, S. A. Selective Alkylation of Toluene with Methanol to Produce Para-Xylene. *J. Catal.* **1981**, *67* (1), 159–174. https://doi.org/10.1016/0021-9517(81)90269-4.

(35) Hwang, A.; Bhan, A. Deactivation of Zeolites and Zeotypes in Methanol-to-Hydrocarbons Catalysis: Mechanisms and Circumvention. *Acc. Chem. Res.* **2019**, *52* (9), 2647–2656. https://doi.org/10.1021/acs.accounts.9b00204.

(36) Chakinala, N.; Chakinala, A. G. Process Design Strategies To Produce P-Xylene via Toluene Methylation: A Review. *Ind. Eng. Chem. Res.* **2021**, *60* (15), 5331–5351. https://doi.org/10.1021/acs.iecr.1c00625.

(37) Wulfers, M. J.; Lobo, R. F. Assessment of Mass Transfer Limitations in Oligomerization of Butene at High Pressure on H-Beta. *Appl. Catal. Gen.* **2015**, *505*, 394–401. https://doi.org/10.1016/j.apcata.2015.08.016.

(38) Cheung, P.; Bhan, A.; Sunley, G. J.; Law, D. J.; Iglesia, E. Site Requirements and Elementary Steps in Dimethyl Ether Carbonylation Catalyzed by Acidic Zeolites. *J. Catal.* **2007**, *245* (1), 110–123. https://doi.org/10.1016/j.jcat.2006.09.020.

(39) DeLuca, M.; Hibbitts, D. Predicting Diffusion Barriers and Diffusivities of C6–C12 Methylbenzenes in MFI Zeolites. *Microporous Mesoporous Mater.* **2022**, *333*, 111705. https://doi.org/10.1016/j.micromeso.2022.111705.

(40) Kapteijn, F.; Moulijn, J. A. Laboratory Catalytic Reactors: Aspects of Catalyst Testing. In *Handbook of Heterogeneous Catalysis*; American Cancer Society, 2008; pp 2019–2045. https://doi.org/10.1002/9783527610044.hetcat0108.

(41) Thiele, E. W. Relation between Catalytic Activity and Size of Particle. *Ind. Eng. Chem.* **1939**, *31* (7), 916–920. https://doi.org/10.1021/ie50355a027.

(42) Fogler, H. S. *Elements of Chemical Reaction Engineering*, 5th edition.; Pearson: Boston, 2016.

(43) Wang, C.; Zhang, L.; Huang, X.; Zhu, Y.; Li, G. (Kevin); Gu, Q.; Chen, J.; Ma, L.; Li, X.; He, Q.; Xu, J.; Sun, Q.; Song, C.; Peng, M.; Sun, J.; Ma, D. Maximizing Sinusoidal Channels of HZSM-5 for High Shape-Selectivity to p -Xylene. *Nat. Commun.* **2019**, *10* (1), 1–8. https://doi.org/10.1038/s41467-019-12285-4.

(44) Karwacki, L.; Kox, M. H. F.; Matthijs de Winter, D. A.; Drury, M. R.; Meeldijk, J. D.; Stavitski, E.; Schmidt, W.; Mertens, M.; Cubillas, P.; John, N.; Chan, A.; Kahn, N.; Bare, S. R.; Anderson, M.; Kornatowski, J.; Weckhuysen, B. M. Morphology-Dependent Zeolite Intergrowth Structures Leading to Distinct Internal and Outer-Surface Molecular Diffusion Barriers. *Nat. Mater.* **2009**, *8* (12), 959–965. https://doi.org/10.1038/nmat2530.

(45) Noh, G.; Sarazen, M. L. Transport in Heterogeneous Catalysis -- beyond Reactant Diffusion Limitations. *J. Catal.* **2021**, *404*, 679–686. https://doi.org/10.1016/j.jcat.2021.09.028.

(46) Noh, G.; Zones, S. I.; Iglesia, E. Consequences of Acid Strength and Diffusional Constraints for Alkane Isomerization and β-Scission Turnover Rates and Selectivities on Bifunctional Metal-Acid Catalysts. *J. Phys. Chem. C* **2018**, *122* (44), 25475–25497. https://doi.org/10.1021/acs.jpcc.8b08460.

(47) Baertsch, C. D.; Funke, H. H.; Falconer, J. L.; Noble, R. D. Permeation of Aromatic Hydrocarbon Vapors through Silicalite−Zeolite Membranes. *J. Phys. Chem.* **1996**, *100* (18), 7676–7679. https://doi.org/10.1021/jp960226h.

(48) Reitmeier, S. J.; Gobin, O. C.; Jentys, A.; Lercher, J. A. Influence of Postsynthetic Surface Modification on Shape Selective Transport of Aromatic Molecules in HZSM-5. *J. Phys. Chem. C* **2009**, *113* (34), 15355–15363. https://doi.org/10.1021/jp905307b.

(49) Webster, C. E.; Drago, R. S.; Zerner, M. C. Molecular Dimensions for Adsorptives. *J. Am. Chem. Soc.* **1998**, *120* (22), 5509–5516. https://doi.org/10.1021/ja973906m.

(50) Choudhary, V. R.; Nayak, V. S.; Choudhary, T. V. Single-Component Sorption/Diffusion of Cyclic Compounds from Their Bulk Liquid Phase in H-ZSM-5 Zeolite. *Ind. Eng. Chem. Res.* **1997**, *36* (5), 1812–1818. https://doi.org/10.1021/ie960411h.

(51) Mirth, G.; Cejka, J.; Lercher, J. A. Transport and Isomerization of Xylenes over HZSM-5 Zeolites. *J. Catal.* **1993**, *139* (1), 24–33. https://doi.org/10.1006/jcat.1993.1003.

(52) Wei, J. A Mathematical Theory of Enhanced Para-Xylene Selectivity in Molecular Sieve Catalysts. *J. Catal.* **1982**, *76* (2), 433–439. https://doi.org/10.1016/0021-9517(82)90272-X.

(53) Young, L. B.; Butter, S. A.; Kaeding, W. W. Shape Selective Reactions with Zeolite Catalysts: III. Selectivity in Xylene Isomerization, Toluene-Methanol Alkylation, and Toluene Disproportionation over ZSM-5 Zeolite Catalysts. *J. Catal.* **1982**, *76* (2), 418–432. https://doi.org/10.1016/0021-9517(82)90271-8.

(54) Yashima, T.; Ahmad, H.; Yamazaki, K.; Katsuta, M.; Hara, N. Alkylation on Synthetic Zeolites: I. Alkylation of Toluene with Methanol. *J. Catal.* **1970**, *16* (3), 273–280. https://doi.org/10.1016/0021-9517(70)90223-X.

(55) Allen, R. H.; Yats, L. D. Kinetics of Three-Compound Equilibrations. V. Concurrent Alkylation and Isomerization. *J. Am. Chem. Soc.* **1961**, *83* (13), 2799–2805. https://doi.org/10.1021/ja01474a003.

(56) Brown, H. C.; Jungk, H. The Reaction of Benzene and Toluene with Methyl Bromide and Iodide in the Presence of Aluminum Bromide; Evidence for a Displacement Mechanism in the Methylation of Aromatic Compounds. *J. Am. Chem. Soc.* **1955**, *77* (21), 5584–5589. https://doi.org/10.1021/ja01626a039.

(57) Solomons, T. W. G.; Fryhle, C. B.; Snyder, S. A. *Organic Chemistry, 12th Edition*; Wiley Global Education, 2016.

(58) Chirico, R. D.; Steele, W. V. Thermodynamic Equilibria in Xylene Isomerization. 5. Xylene Isomerization Equilibria from Thermodynamic Studies and Reconciliation of Calculated and Experimental Product Distributions. *J. Chem. Eng. Data* **1997**, *42* (4), 784–790. https://doi.org/10.1021/je970030q.

(59) Hill, I.; Malek, A.; Bhan, A. Kinetics and Mechanism of Benzene, Toluene, and Xylene Methylation over H-MFI. *ACS Catal.* **2013**, *3* (9), 1992–2001. https://doi.org/10.1021/cs400377b.

(60) Cheung, P.; Bhan, A.; Sunley, G. J.; Iglesia, E. Selective Carbonylation of Dimethyl Ether to Methyl Acetate Catalyzed by Acidic Zeolites. *Angew. Chem. Int. Ed.* **2006**, *45* (10), 1617–1620. https://doi.org/10.1002/anie.200503898.

(61) Eyring, H. The Activated Complex in Chemical Reactions. *J. Chem. Phys.* **1935**, *3* (2), 107–115. https://doi.org/10.1063/1.1749604.

(62) Evans, M. G.; Polanyi, M. Some Applications of the Transition State Method to the Calculation of Reaction Velocities, Especially in Solution. *Trans. Faraday Soc.* **1935**, *31* (0), 875–894. https://doi.org/10.1039/TF9353100875.

(63) Corma, A.; Fornés, V.; Forni, L.; Márquez, F.; Martínez-Triguero, J.; Moscotti, D. 2,6-Di-Tert-Butyl-Pyridine as a Probe Molecule to Measure External Acidity of Zeolites. *J. Catal.* **1998**, *179* (2), 451–458. https://doi.org/10.1006/jcat.1998.2233.

(64) Jones, A. J.; Carr, R. T.; Zones, S. I.; Iglesia, E. Acid Strength and Solvation in Catalysis by MFI Zeolites and Effects of the Identity, Concentration and Location of Framework Heteroatoms. *J. Catal.* **2014**, *312*, 58–68. https://doi.org/10.1016/j.jcat.2014.01.007.

(65) Zhu, Q.; Kondo, J. N.; Yokoi, T.; Setoyama, T.; Yamaguchi, M.; Takewaki, T.; Domen, K.; Tatsumi, T. The Influence of Acidities of Boron- and Aluminium-Containing MFI Zeolites on Co-Reaction of Methanol and Ethene. *Phys. Chem. Chem. Phys.* **2011**, *13* (32), 14598–14605. https://doi.org/10.1039/C1CP20338J.

(66) Chu, C. T.-W.; Kuehl, G. H.; Lago, R. M.; Chang, C. D. Isomorphous Substitution in Zeolite Frameworks: II. Catalytic Properties of [B]ZSM-5. *J. Catal.* **1985**, *93* (2), 451–458. https://doi.org/10.1016/0021-9517(85)90192-7.

(67) Bickel, E. E.; Nimlos, C. T.; Gounder, R. Developing Quantitative Synthesis-Structure-Function Relations for Framework Aluminum Arrangement Effects in Zeolite Acid Catalysis. *J. Catal.* **2021**, *399*, 75–85. https://doi.org/10.1016/j.jcat.2021.04.027.

(68) Pinar, A. B.; Verel, R.; Pérez-Pariente, J.; van Bokhoven, J. A. Direct Evidence of the Effect of Synthesis Conditions on Aluminum Siting in Zeolite Ferrierite: A 27Al MQ MAS NMR Study. *Microporous Mesoporous Mater.* **2014**, *193*, 111–114. https://doi.org/10.1016/j.micromeso.2014.03.016.

(69) Wang, Z.; Chu, W.; Zhao, Z.; Liu, Z.; Chen, H.; Xiao, D.; Gong, K.; Li, F.; Li, X.; Hou, G. The Role of Organic and Inorganic Structure-Directing Agents in Selective Al Substitution of Zeolite. *J. Phys. Chem. Lett.* **2021**, *12* (38), 9398–9406. https://doi.org/10.1021/acs.jpclett.1c01448.

(70) Berkson, Z. J.; Hsieh, M.-F.; Smeets, S.; Gajan, D.; Lund, A.; Lesage, A.; Xie, D.; Zones, S. I.; McCusker, L. B.; Baerlocher, C.; Chmelka, B. F. Preferential Siting of Aluminum Heteroatoms in the Zeolite Catalyst Al-SSZ-70. *Angew. Chem. Int. Ed.* **2019**, *58* (19), 6255–6259. https://doi.org/10.1002/anie.201813533.

(71) Liu, M.; Yokoi, T.; Yoshioka, M.; Imai, H.; Kondo, J. N.; Tatsumi, T. Differences in Al Distribution and Acidic Properties between RTH-Type Zeolites Synthesized with OSDAs and without OSDAs. *Phys. Chem. Chem. Phys.* **2014**, *16* (9), 4155–4164. https://doi.org/10.1039/C3CP54297A.

(72) Han, O. H.; Kim, C.-S.; Hong, S. B. Direct Evidence for the Nonrandom Nature of Al Substitution in Zeolite ZSM-5: An Investigation by 27Al MAS and MQ MAS NMR. *Angew. Chem. Int. Ed.* **2002**, *41* (3), 469–472. https://doi.org/10.1002/1521-3773(20020201)41:3<469::AID-ANIE469>3.0.CO;2-K.

(73) Sklenak, S.; Dědeček, J.; Li, C.; Wichterlová, B.; Gábová, V.; Sierka, M.; Sauer, J. Aluminum Siting in Silicon-Rich Zeolite Frameworks: A Combined High-Resolution 27Al NMR Spectroscopy and Quantum Mechanics / Molecular Mechanics Study of ZSM-5. *Angew. Chem. Int. Ed.* **2007**, *46* (38), 7286–7289. https://doi.org/10.1002/anie.200702628.

(74) Holzinger, J.; Beato, P.; Lundegaard, L. F.; Skibsted, J. Distribution of Aluminum over the Tetrahedral Sites in ZSM-5 Zeolites and Their Evolution after Steam Treatment. *J. Phys. Chem. C* **2018**, *122* (27), 15595–15613. https://doi.org/10.1021/acs.jpcc.8b05277.

(75) Dib, E.; Mineva, T.; Veron, E.; Sarou-Kanian, V.; Fayon, F.; Alonso, B. ZSM-5 Zeolite: Complete Al Bond Connectivity and Implications on Structure Formation from Solid-State NMR and Quantum Chemistry Calculations. *J. Phys. Chem. Lett.* **2018**, *9* (1), 19–24. https://doi.org/10.1021/acs.jpclett.7b03050.

(76) Schmithorst, M. B.; Prasad, S.; Moini, A.; Chmelka, B. F. Direct Detection of Paired Aluminum Heteroatoms in Chabazite Zeolite Catalysts and Their Significance for Methanol Dehydration Reactivity. *J. Am. Chem. Soc.* **2023**, *145* (33), 18215–18220. https://doi.org/10.1021/jacs.3c05708.

(77) Sang, S.; Chang, F.; Liu, Z.; He, C.; He, Y.; Xu, L. Difference of ZSM-5 Zeolites Synthesized with Various Templates. *Catal. Today* **2004**, *93–95*, 729–734. https://doi.org/10.1016/j.cattod.2004.06.091.

(78) Rollmann, L. D.; Schlenker, J. L.; Lawton, S. L.; Kennedy, C. L.; Kennedy, G. J.; Doren, D. J. On the Role of Small Amines in Zeolite Synthesis. *J. Phys. Chem. B* **1999**, *103* (34), 7175–7183. https://doi.org/10.1021/jp991913m.

(79) Rollmann, L. D.; Schlenker, J. L.; Kennedy, C. L.; Kennedy, G. J.; Doren, D. J. On the Role of Small Amines in Zeolite Synthesis. 2. *J. Phys. Chem. B* **2000**, *104* (4), 721–726. https://doi.org/10.1021/jp993561p.

(80) Schwarz, S.; Kojima, M.; O'Connor, C. T. Effect of Tetraalkylammonium, Alcohol and Amine Templates on the Synthesis and High Pressure Propene Oligomerisation Activity of ZSM-Type Zeolites. *Appl. Catal.* **1991**, *73* (2), 313–330. https://doi.org/10.1016/0166-9834(91)85144-K.

(81) Valyocsik, E. W.; Rollmann, L. D. Diamines as Templates in Zeolite Crystallization. *Zeolites* **1985**, *5* (2), 123–125. https://doi.org/10.1016/0144-2449(85)90084-3.

(82) Guo, Y.; Wang, S.; Geng, R.; Wang, P.; Li, S.; Dong, M.; Qin, Z.; Wang, J.; Fan, W. Enhancement of the Dimethyl Ether Carbonylation Activation via Regulating Acid Sites Distribution in FER Zeolite Framework. *iScience* **2023**, *26* (10), 107748. https://doi.org/10.1016/j.isci.2023.107748.

(83) Zones, S. I.; Hwang, S.-J.; Davis, M. E. Studies of the Synthesis of SSZ-25 Zeolite in a "Mixed-Template" System. *Chem. – Eur. J.* **2001**, *7* (9), 1990–2001. https://doi.org/10.1002/1521-3765(20010504)7:9<1990::AID-CHEM1990>3.0.CO;2-G.

(84) Caullet, P.; Hazm, J.; Guth, J. L.; Joly, J. F.; Lynch, J.; Raatz, F. Synthesis of Zeolite Beta from Nonalkaline Fluoride Aqueous Aluminosilicate Gels. *Zeolites* **1992**, *12* (3), 240–250. https://doi.org/10.1016/S0144-2449(05)80290-8.

(85) Bates, J. S.; Bukowski, B. C.; Greeley, J.; Gounder, R. Structure and Solvation of Confined Water and Water–Ethanol Clusters within Microporous Brønsted Acids and Their Effects on Ethanol Dehydration Catalysis. *Chem. Sci.* **2020**, *11* (27), 7102–7122. https://doi.org/10.1039/D0SC02589E.

(86) First, E. L.; Gounaris, C. E.; Wei, J.; Floudas, C. A. Computational Characterization of Zeolite Porous Networks: An Automated Approach. *Phys. Chem. Chem. Phys.* **2011**, *13* (38), 17339–17358. https://doi.org/10.1039/C1CP21731C.

(87) PubChem. *1,4-Diazabicyclo[2.2.2]octane*. https://pubchem.ncbi.nlm.nih.gov/compound/9237 (accessed 2024-03-02).

(88) PubChem. *Ethylenediamine*. https://pubchem.ncbi.nlm.nih.gov/compound/3301 (accessed 2024-03-02).